

UNIVERSITY OF MISKOLC

FACULTY OF MECHANICAL ENGINEERING AND INFORMATICS



# HARVESTING ENERGY FOR ERS AUTOMOBILITY

PHD THESIS

Prepared by

**Mohammed Alaa Alwafaie**

Engineering of Mechanical (BSc, MSc)

ISTVÁN SÁLYI DOCTORAL SCHOOL OF MECHANICAL ENGINEERING SCIENCES

TOPIC FIELD OF BASIC ENGINEERING SCIENCES

TOPIC GROUP OF MECHANICS OF SOLIDS

Head of Doctoral School

**Dr. Gabriella Vadászné Bognár**

DSc, Full Professor

Head of Topic Group

**Dr. György Szeidl**

Full Professor

Scientific Supervisor

**Dr. Béla Kovács**

**Miskolc**

**2025**

## **SUPERVISOR'S RECOMMENDATIONS**

Mr. Mohammed Alwafaie, a dedicated PhD candidate, has been under my supervision for nearly four years. Since September 2020. His research is supported by the prestigious "Stipendium Hungaricum" scholarship program.

Mohammed's PhD research centers on energy harvesting solutions for mobility applications, a timely and forward-looking area of study given the growing emphasis on energy sustainability and the increasing energy demands of modern transport systems. His work explores innovative methods to capture and convert otherwise wasted energy such as electromagnetic effect from the wheel ,piezoelectric and electromechanical by MMR into useful electrical energy within vehicular environments. Throughout his research, Mohammed has focused on designing integrated energy harvesting systems that combine multiple mechanisms to improve energy recovery rates. His investigations involve both theoretical modeling and advanced numerical simulations, leveraging thermodynamic and mechanical analysis tools. He systematically assessed system performance under variable operating conditions and compared his simulation outcomes with data reported in the literature to ensure accuracy and relevance. Among his key accomplishments is finding pedal harvesting energy (PHE) that effectively increases conversion efficiency through multi-source energy capture. This contribution marks a significant advancement in the field and reflects Mohammed's ability to merge innovation with rigorous engineering practice.

His findings have been disseminated through well-regarded scientific journals, international conferences, and doctoral symposia. Journals that have featured his work include International Journal of Membrane Science and Technology-Scopus index , AIP Conference and Acta Technologica. Mohammed successfully passed his complex doctoral examination in 04.06.2022. He was awarded his pre-degree certificate with distinction on July 05, 2024.

As a doctoral researcher, Mohammed has demonstrated independence, creativity, and a strong sense of initiative. He has consistently met high academic standards and shown excellent progress in mastering advanced research methods and communication skills. I am confident that his knowledge, capabilities, and dedication will continue to make significant contributions in both academic and industrial research environments.

05 June 2025

Béla Kovács

## Table of contents

<b>1. Introduction and Literature Review .....</b>	<b>10</b>
1.1 Energy Recovery System .....	10
1.2 Types of an energy recovery system .....	10
<b>2. Key components of an Energy Capture .....</b>	<b>11</b>
2.1 Regenerative Braking or Motor Generating Unit Kinetic (MGU-K).....	11
2.1.1 Types of Kinetic Energy Recovery System (KERS) .....	11
2.1.2 Principle working of MGUK.....	13
2.2 Exhaust Gas Energy Recovery or Motor Generating Unit Heat (MGU-H).....	14
2.2.1 Force on moving charge (Lorentz-force).....	14
2.2.2 Force on a current-carrying wire (Laplace force).....	15
2.2.3 Torque of MGUH .....	15
2.3 Directly Injected or Turbocharger .....	16
<b>3. Key components of an energy conversion and storage in automotive .....</b>	<b>17</b>
3.1 Energy Storage .....	17
3.2 Control electronic (CE) .....	17
<b>4. Electromagnetic effects for other harvesting energy .....</b>	<b>20</b>
4.1 Introduce.....	20
4.2 Characterization of electromagnetic harvesting energy .....	21
4.3 Simulation of electromagnetic harvesting energy .....	22
4.3.1 Radial Design (RD): .....	22
4.3.2 Axial Design (AD):.....	26
4.4 Experiment of axial design electromagnetic harvesting energy .....	31
4.4.1 Free falling test .....	31
4.4.2 Rotation motion test.....	33
4.5 Results of electromagnetic harvesting energy .....	34
4.6 Conclusion.....	36
<b>5. Piezoelectric effects for other harvesting energy .....</b>	<b>37</b>
5.1 Introduction .....	37

5.2 Procedures types of design piezoelectric .....	38
5.2.1 Piezoelectric within the tire (first case) .....	39
5.2.2 Piezoelectric with magneto strictive materials (second case) .....	39
5.3 The calculation and experimental of piezoelectric harvesting energy .....	40
5.3.1 First case .....	40
5.3.2 Second case.....	47
5.4 The results of piezoelectric harvesting energy .....	51
5.5 Conclusion.....	52
<b>6. Roads (infrastructure) effects for other harvesting energy.....</b>	<b>53</b>
6.1 Introduction:.....	53
6.2 Algorithm of harvesting charging station:.....	54
6.3 Design and construction of roads harvesting energy .....	55
6.3.1 First design (LAD1).....	56
6.3.2 Second design (LAD2) .....	57
6.3.3 Third design (LAD3) .....	58
6.3.4 Fourth design (LAD4).....	58
6.3.5 Fifth design (LAD5) .....	59
6.3.6 Sixth design (LAD6).....	60
6.4 Test piezoelectric designs of roads harvesting energy .....	60
6.4.1 first design (LAD1) test .....	60
6.4.2 Fourth design (LAD4) test .....	64
6.5 Conclusion.....	68
<b>7. Electromechanical effects by MMR for other harvesting energy.....</b>	<b>69</b>
7.1 Introduction .....	69
7.2 Characteristics and features of electromechanically energy .....	70
7.2.1 Pedal (throttle + break) module .....	70
7.2.2 Pedal harvesting energy module .....	71
7.2.3 Energy storage module .....	73

7.3 Statistical analysis of electromechanically energy by MMR .....	74
7.3.1 Pedal harvesting energy dynamics .....	74
7.3.2 Dynamics equations for rack in MMR.....	76
7.3.3 Dynamics equations for pinion and outer ring of one-way clutch in MMR.....	76
7.3.4 Dynamics equations for coupling, gearbox and generator in MMR.....	77
7.3.5 State of disengagement equation in MMR.....	79
7.4 Modeling and Experiment of MMR:.....	80
7.5 Conclusion:.....	83
<b>New Scientific results of the theses.....</b>	<b>85</b>
<b>Acknowledgements .....</b>	<b>87</b>
<b>References .....</b>	<b>88</b>
<b>List of figures.....</b>	<b>93</b>
<b>List of tables.....</b>	<b>95</b>
<b>List of publications.....</b>	<b>96</b>

## List of symbols and abbreviations

$a$	distance between the center of wheel and the center of coil (m)
$a_1$	initial radial position of the coil (m)
$a_2$	final radial position of the coil (m)
$A$	area (m <sup>2</sup> )
$a^\theta$	angular acceleration (rad/sec <sup>2</sup> )
$a^r, r''$	radial acceleration (m/ sec <sup>2</sup> )
$B$	magnetic field (T)
$C_b$	damping of PHE coefficient (N.s/m)
$C_d$	electric charge density per surface (C/m <sup>2</sup> )
$C'_d$	electric charge density (C)
$c$	stiffness matrix
$d$	distance from the neutral axis to the outermost fiber (m)
$E$	electrical energy (W)
$E$	electric field (V/m)
$e$	modulus of elasticity (Pa)
$e'$	Young's moduli (Pa)
$G$	shear moduli (Pa)
$F$	Lorentz force (N)
$F'$	Laplace force (N)
$F_m$	electromagnetic force (N)
$F_f$	friction force (N)
$F_{Th}$	pressed force from the throttle pedal (N)
$F_b$	pressed force from the brake pedal (N)
$F_t$	total forces that come from pressing of the throttle and brake pedals separately (N)

$F_p$	force of pinion gear (N)
$g$	gravity acceleration (m/sec <sup>2</sup> )
$H$	magnetic field (T)
$I$	electric current flowing through the machine (A)
$I$	moment of inertia in general (kg.m <sup>2</sup> )
$I_{p, n}$	moment of inertia for $n$ pinion (kg.m <sup>2</sup> )
$I_c$	moment of inertia for coupling (kg.m <sup>2</sup> )
$I_b$	moment of inertia for gearbox (kg.m <sup>2</sup> )
$I_{ge}$	moment of inertia for generator (kg.m <sup>2</sup> )
$I_\sigma$	moment of inertia of the cross-section for wheel (m <sup>4</sup> )
$K_t$	generator stiffness (N/m)
$K_g$	electromotive voltage constant (V.sec/rad)
$K_m$	electromagnetic constant (kg.m / rad. s <sup>2</sup> . A <sup>2</sup> )
$K_v$	damping constant (N.s/m)
$K_b$	spring stiffness of pedal harvesting energy (N/m)
$L$	inductance of coil (H)
$l$	length of wire (m)
$m$	mass of magnetic (kg)
$M_{eq}$	equivalent mass (kg)
$M_b$	mass of pressing (kg)
$M_r$	mass of rack (kg)
$M$	magnetic dipole moment (A.m <sup>2</sup> )
$M_\sigma$	bending moment (N.m)
$n$	number of loops / turns
$n'$	ratio of gearbox

$N$	normal force (N)
$n$	number of pinions
$P$	power (W)
$p$	pressure (N/m <sup>2</sup> )
$p'$	pitch
$q$	electric charge (C)
$r$	radius of wheel (m)
$S$	compliance matrix
$R$	resistance ( $\Omega$ )
$R$	radius of coil / pinion (m)
$R_1$	inner radius of the loop (m)
$R_2$	outer radius of the loop (m)
$R_t$	resistance in pedal harvesting energy ( $\Omega$ )
$r_1$	distance of the magnetic from the center of wheel when entry the coil (m)
$r_2$	distance of the magnetic from the center of wheel when exit the coil (m)
$r'$	radial velocity (m/sec)
$T_p$	torque of pinion gear (N.m)
$T_c$	torque due to the presence of external loads (N.m)
$T_g$	electromagnetic induced torque (N.m)
$t$	time (sec)
$\hat{t}$	Stress vector (N/m <sup>2</sup> )
$U, V$	voltage (V)
$v$	volume (m <sup>3</sup> )
$V_m$	volume of magnetic (m <sup>3</sup> )
$v$	speed of magnetic (m/sec)
$v'$	speed of charge (m/sec)



$x$	position of magnetic to center of loop (m)
$Z_c$	capacitance impedance ( $\Omega$ )
$Z_m$	mechanical impedance (N.sec/m)
$\varepsilon$	induced voltage in coil (V)
$\sigma$	normal stress (N/m <sup>2</sup> )
$\varphi_e$	electromechanical coupling factor
$\varphi_m$	magnetostrictive coupling factor
$\eta$	efficiency of pinion
$\omega$	angular velocity (rotational speed) of gearbox (rad/sec)
$\tau$	torque (N.m)
$\theta, \alpha$	angle (rad)
$\dot{\theta}$	angular velocity of wheel (rad/sec)
$\ddot{\theta}$	angular acceleration of wheel (rad/sec <sup>2</sup> )
$\mu_0$	magnetic permeability (H/m)
$\mu$	kinetic coefficient friction
$\gamma_r$	coupling factor (N/A)
$\tau^n$	shear stress (N/m <sup>2</sup> )
$\epsilon$	strain
$\nu$	Poisson's ratio

## 1. Introduction and Literature Review

### 1.1 Energy Recovery System

ERS plays a crucial role in power performance, decreasing environmental effect and selling sustainable improvement in industries. Continued enhancements in recovery technology and their integration into systems and methods have the potential to similarly enhance energy efficiency and make contributions to a more sustainable future. It is a technology that pursuits to seize and recycle electricity that might otherwise be wasted in various applications. The number one dreams of ERS are to growth power efficiency, reduce electricity consumption, and decrease environmental impact. ERS may be used in lots of industries, inclusive of automotive and commercial creation structures.

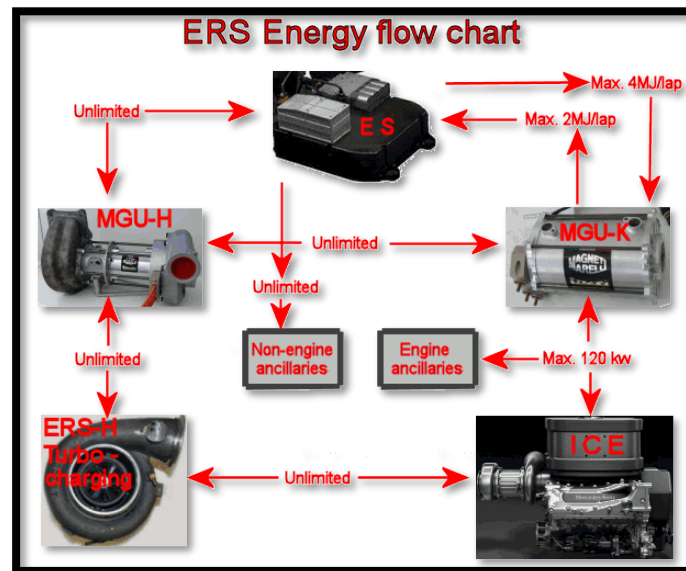


Figure 1. 1 The flow chart of energy recovery system by (formula 1Dictionary, 2014)

### 1.2 Types of an energy recovery system

1. Energy Capture: ERSs are designed to capture and recover electricity from resources that might generally be lost or dissipated as waste. This can encompass kinetic energy [1], thermal power [2], or different kinds of power generated for the duration of the operation of a system or technique [3].

2. Energy Conversion [4]: Once the strength is captured, an ERS converts it into a usable form. This conversion technique can involve various technologies, which include electrical mills,

heat exchangers, or energy garage systems. The aim is to convert the captured strength into an appropriate shape for reuse or storage.

3. Energy Storage [5]: In many instances, ERSs comprise electricity storage structures to keep the captured power for later use. Energy storage technologies can encompass batteries [6], supercapacitors [7], flywheels [8], or compressed air structures [9]. These storage structures permit for the green utilization of the captured power while it is maximum wanted or at some stage in intervals of better demand.

4. Energy Reuse: The recovered energy from an ERS may be reused in the same machine or transferred to different systems for extraordinary purposes. For example, in an automotive application, the recovered electricity may be used to electricity auxiliary components, recharge batteries [10], or provide additional energy for the duration of acceleration.

## **2. Key components of an Energy Capture**

It is consisting of main components which can refer it as follows:

### **2.1 Regenerative Braking or Motor Generating Unit Kinetic (MGU-K)**

Regenerative braking is a key technology in ERS. More of research studies about this technology and last of them Jafari et al. [11] that refer about the Hybrid energy storage system using electric vehicle batteries for regenerative braking energy recovery at railway stations. When a vehicle decelerates or brakes, the kinetic energy that would commonly be dissipated as warmth is as an alternative captured and transformed into electrical power. This energy is then stored in batteries or different power garage systems in the car. During acceleration or when additional power is required, the saved strength can be discharged to power electric powered automobiles, reducing the burden at the engine and improving ordinary gas efficiency.

So that, it is the development of kinetic energy recovery system (KERS) and it is a generator that works in two ways which can capture energy from the Automotive Car under braking.

#### **2.1.1 Types of Kinetic Energy Recovery System (KERS)**

1- Mechanical flywheel system: When the car is using the flywheel, it isn't linked to the axle. Since the car slows down whilst the motive force starts braking, the flywheel is connected with the axle and this manner allows the traditional brakes sluggish down the automobile then flywheel starts off evolved rotating at a totally excessive pace. After spinning, the flywheel disconnects from the axle. When the auto needs to accelerate once more at some point the

flywheel can be reconnected to the axle to provide the automobile more enhance. We found more researches study it like Hedlund et al. [12], POPA et al. [13]

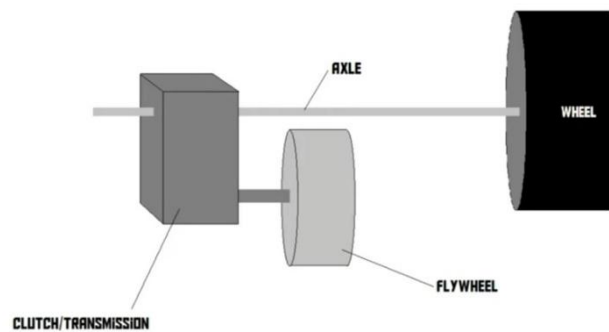


Figure 2. 1 The mechanical flywheel system of KERS by Hedlund et al. [12]

2- Generator & Motor system: The Generator & Motor are included as part of the energy recovery system in the vehicle. Near one axle is a generator that connects to the front axle when the driver starts to apply the brakes. As the brakes are applied, the generator begins to rotate, using kinetic energy and converting it into electricity. The generated electricity is then transferred to an electromagnet. The electric motor uses this electricity to turn a new flywheel, acting as a form of energy storage. When the vehicle stops and no braking is required, the generator is disconnected from the axle, and the spinning flywheel is disconnected from the electric motor so that the spinning flywheel can be returned to the motor in place the speed of the vehicle or the other speed is important. Because electric motors can act as generators, they generate electricity for the motors through the motion of the wheels. This generated electricity is then fed back into the generator, which now operates as a mechanism. A generator attached to the axle now propels the wheels forward, further increasing power. This seamless transition between generator and motor operations occurs in less than a second, allowing for fast and efficient energy transfer.

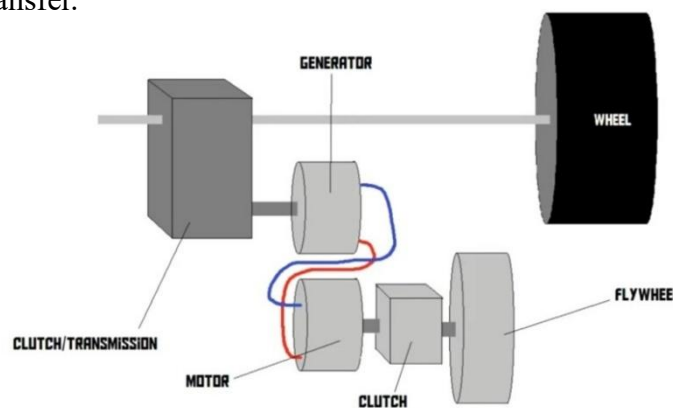


Figure 2. 2 The mechanical flywheel with gear and generator system of KERS

3- Generator & Battery: This type replaces the electric motor and flywheel with a battery or super capacitor to store energy. This system is more efficient because it uses a battery.

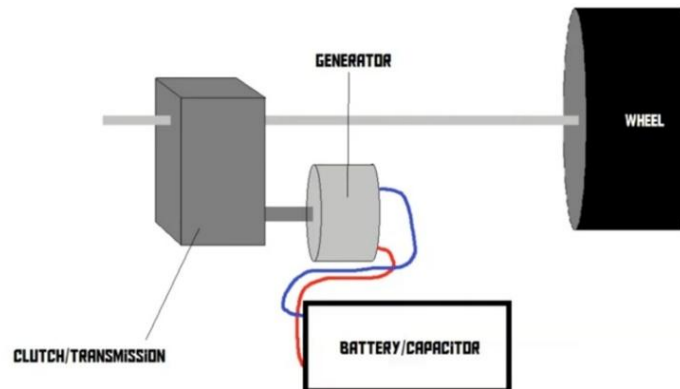


Figure 2. 3 The generator with battery system of KERS

### 2.1.2 Principle working of MGUK

The motor generating unit kinetic works as generator mode and motor mode.

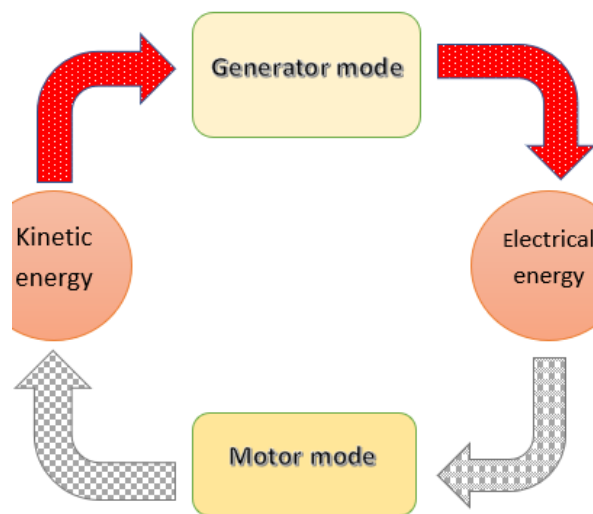


Figure 2. 4 The Illustration work of MGUK

The principal function of MGU-K (Motor Generator Unit-Kinetic) is the interaction between electric and magnetic fields as explained in (Chain Bear,2018) [14]. The rotor of the MGU-K is rotated by the vehicle's magnetic field, and this relationship between current and magnetic field is bidirectional. According to Lorentz law, when an electric current passes through a wire in a magnetic field, it produces a kinetic force. Similarly, a wire circuit induces a current in the wire when it enters a magnetic field. Using this principle, as the wire loop of the MGU-K rotates clockwise, the magnetic fields move from left to right, the left side of the loop up, and

carry current flow to the left top on the right -hand comes to the side. As the loop passes halfway, the current direction alters, slowly generating current.

In motor mode, the induced current supplied in the wire loop causes a rotational motion against the direction of rotation in the wire. Following the left-hand rule, the electric current produces a counterclockwise force, which, by rotating the rotor in the direction of the wheel drive, causes the wheel to exert a fighting force greatly counter-clockwise. The magnetic field and current exert a force against the motion of the rotor, generating power from the rear wheel. In motor mode, when the loop rotates more than ninety degrees, the direction of current changes to opposite sides of the loop. The right side of the rope goes up and the left side goes down.

To deal with this issue, Formula 1 (F1) uses an alternating current, which means the current in the wire switches direction intermittently. As the loop flips over, the current direction switches, but the forces acting on the loop continue to act in the same direction. This constant rotation of the current gives the wheel its rotating motion.

## 2.2 Exhaust Gas Energy Recovery or Motor Generating Unit Heat (MGU H)

The MGU-H works by converting the kinetic energy in the emissions into electricity [15]. This process requires wires to interact with the magnetic fields inside the motor. When wires are exposed to a rotating magnetic field, they generate electricity, even when they are not connected to an electrical source. The rotation of the motor driven by external forces produces the necessary rotating magnetic field and torque [16].

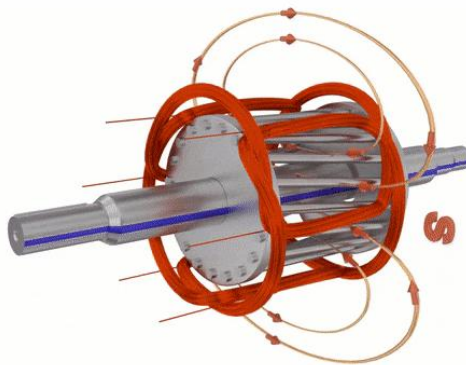


Figure 2. 5 The Illustration work of MGU-H

### 2.2.1 Force on moving charge (Lorentz-force)

The comprehensive understanding of electromagnetic phenomena requires the integration of various physical laws, and the Lorentz force law plays a crucial role in completing this intricate picture. By elucidating the force acting on a moving point charge  $q$  in the presence of electromagnetic fields, the Lorentz force law unveils the intricate interplay between electric (E) and magnetic (B) fields. However, it is important to recognize that electromagnetic forces alone do not encompass the entirety of the interaction experienced by charged particles. These particles can also be subject to the influence of other fundamental forces, such as gravity and

nuclear forces. Consequently, Maxwell's equations, which govern electromagnetic phenomena, are not standalone principles but rather intricately linked to other physical laws through the charge and current densities. In this interconnected framework, the response of a point charge to the Lorentz force law represents just one facet of the broader tapestry of electromagnetic interactions. To gain a comprehensive perspective on the behavior of charged particles, one must consider the combined effects of electromagnetic, gravitational, and nuclear forces, thereby revealing the intricate nature of the physical world.

This force can write as:

$$F = q(E + \mathbf{v}' \times \mathbf{B}) \quad (2.1)$$

### 2.2.2 Force on a current-carrying wire (Laplace force)

The Laplace force is acting on a wire that carries an electric current in the presence of a magnetic field, gives rise to various practical phenomena. When a current flows through a loop exposed to a magnetic field, the field exerts a torque on the loop. This principle finds wide application in motors, where the loop is connected to a shaft that rotates under the influence of the torque. As a result, the electrical energy from the current is converted into mechanical energy, driving the rotation of the loop and shaft. This mechanical energy can then be utilized to power other devices and perform calculations. So, it gives as:

$$F' = Il \times B \quad (2.2)$$

### 2.2.3 Torque of MGUH

As MGU-H gives the energy depending on when current flows through a wire placed in a magnetic field, the magnetic field exerts a torque on the loop. In which the loop is connected to a shaft that rotates due to torque. Thus, the electric energy from the current is converted into mechanical energy by the rotation of the loop and shaft, and this mechanical energy is then used to power another device. It can express as

$$\tau = nIAB \sin \theta \quad (2.3)$$

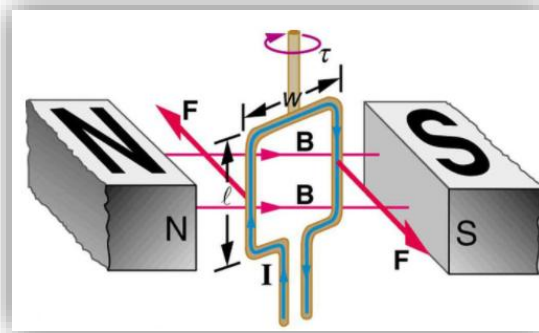


Figure 2. 6 The torque of MGU-H in one loop

## 2.3 Directly Injected or Turbocharger

The turbocharger consists of two turbines. The first turbine is driven by hot air from the internal combustion engine (ICE). According to (Donut,2018) [17], the turbine spins as fast as a pin wheel and is attached to the compressor wheel on the other side of the turbo. The compressor wheel also begins to rotate slowly. As the turbocharger runs, it sucks in more air from an inlet and forces it through an inlet into the intake barrel the compressed air is cooler, with more oxygen . . . This increase in oxygen causes more fuel to burn, increasing power output. A blow-off valve is used to prevent compressed air from returning to the turbocharger when the throttle is released. This valve reduces the pressure by returning the air to the atmosphere or, in some modified systems, to the turbocharger cycle. Because of the high heat generated by the turbocharger, pay particular attention to the hot portion of the turbo. This region often exhibits a rusty appearance due to the intense heat, which acts as a catalyst to rapidly oxidize metal in addition to driving the compressor section of the turbocharger to produce heat due to compressed air. When air is compressed, the molecules are forced closer together, creating friction. This friction generates heat as the molecules interact strongly with each other and increase in gas velocity due to pressure decreases its density. But as the hot turbocharged exhaust cools, the molecules shrink, stay closer together, and regain their density. To prevent this issue by few ways as most popular and simple it is with an intercooler which is located between the turbo and the engine, the air passes through channels with cooling fins. The cool air from outside passes over the fins absorbs the heat and reduces the temperature.

There is timing between hitting gas and feeling the boost called Lag and this is solved by engineers by using two smaller turbos to push more air than one large one. The best located is Parallel turbo charging using two equal sized turbos working 100% of the time. Sequential Systems use a little turbo that spools up quickly to tide you over until another larger turbo which has time to spool up. This method alleviates turbo lag and provides a much smoother power again like in Mark 4 Supra and FDRX7 which use sequential twin turbo systems.

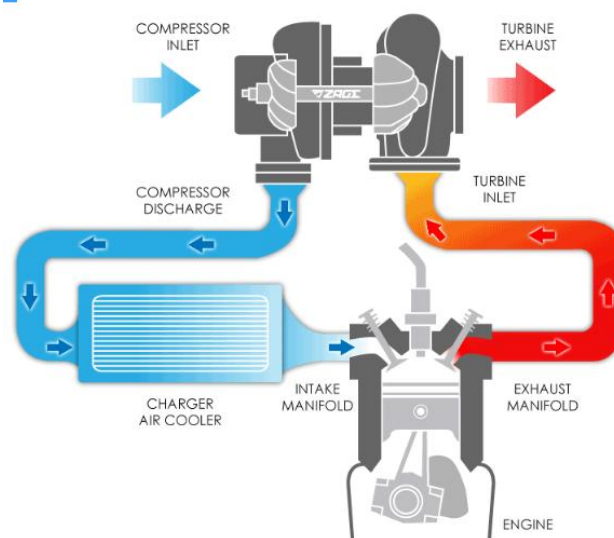


Figure 2. 7 Turbocharger cycle



The turbocharger connected with MGUH which works as we see before by wasting exhaust energy. The MGU-H comes in to solve the Lag which causes when the Automotive starts to accelerate again, the turbine takes a time (second or two) to get up more speed and the compressor doesn't spin so that it starts boost the turbine and give the speed for it.

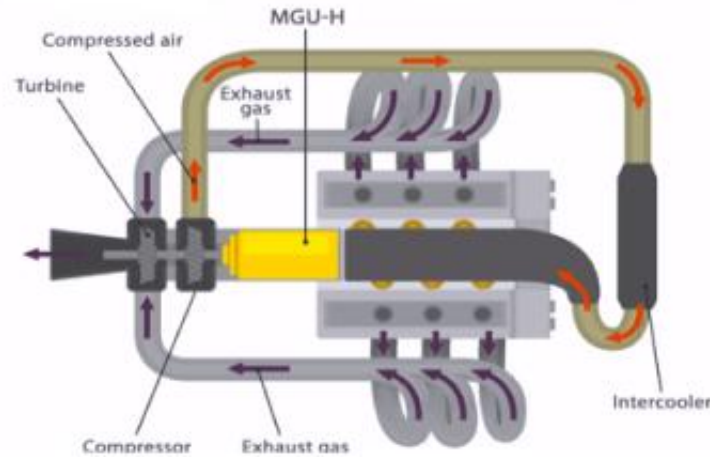


Figure 2. 8 the MGU-H connecting with turbocharger

### 3. Key components of an energy conversion and storage in automotive

This is represented by energy storage (ES) and control electronic (CE)

#### 3.1 Energy Storage

This is where all the energy recovered from the MGUK and MGUH is stored. It functions like a large battery or a set of powerful capacitors that enable the utilization of the recovered energy. With the enhanced energy storage capacity, the system is capable of handling larger amounts of energy, resulting in a power output of up to 200 kW. Moreover, the energy storage system has led to an increase in voltage, now operating at just under 1000 volts with the ERS battery.

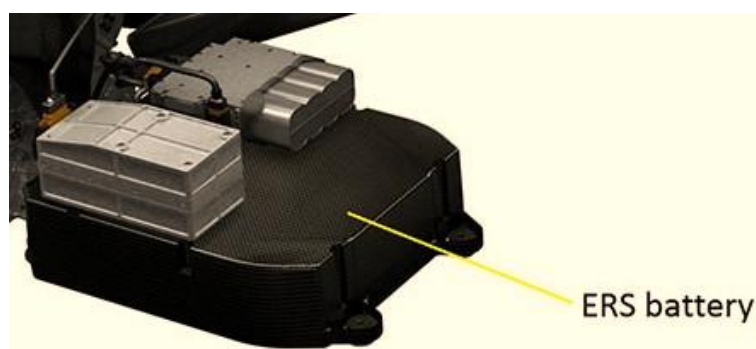


Figure 3. 1 The energy storage (ERS battery)

#### 3.2 Control electronic (CE)

The Control electronics (CE) has the function of managing the AC three-phase power from the Motor Generator Units (MGUs) and the DC power from the battery in Formula One. In the current setup, Formula One cars utilize two MGUs: one for the kinetic system (CUK) and one

for the heat system (CUH). Within the CE, there are two sides to its operation. The low-voltage side consists of logic boards that control the high-voltage side using switches and capacitors to transfer power between the MGU and the battery.

During energy harvesting, the respective MGU sends its AC power through three high-current cables to the CE. Inside the control unit's casing, there are high-current switches known as IGBTs (insulated gate bipolar transistors) that switch the current. The current also passes through capacitors, and the electronics within the CE convert the current into DC format. The CE then transmits the DC power to the battery via two cables. Conversely, the CE can also utilize battery power to spin the MGUs by reversing this process. One advantage of this setup is that the car does not require an alternator or its own battery since the CEs provide the car with a 12-24 V supply for other electrical systems.



*Figure 3. 2 The control electronic by (Bold valuable tec,2019)*

The previous description provides a general understanding of the components, it's important to note that the actual ERS system in Formula One can be more intricate and may involve additional components and subsystems. In this comprehensive study, it will be exploring various other types of energy harvesting that can be incorporated into the system to enhance efficiency and foster the development of technical advancements with potential benefits for passenger car applications. One of the areas of focus will be Mechanical Motion Rectifier (MMR), which involves utilizing the excess energy from the mechanical motion of pedals and generate additional power. This process improves overall efficiency. Furthermore, will delve into enhanced vibratory, pressing energy recovery methods and electromagnetic effects. These techniques involve harnessing the energy generated by vibrations, shocks, and mechanical movements within the vehicle and converting it into usable electrical power. By capturing and utilizing this otherwise wasted energy, significant gains in overall efficiency can be achieved. Moreover, the study explores the concept of better hybridization, which involves integrating multiple energy sources and storage systems to optimize power delivery and usage in passenger cars. By combining traditional internal combustion engines with electric motors, batteries, and other energy storage technologies, hybridization offers improved fuel efficiency and reduced emissions.

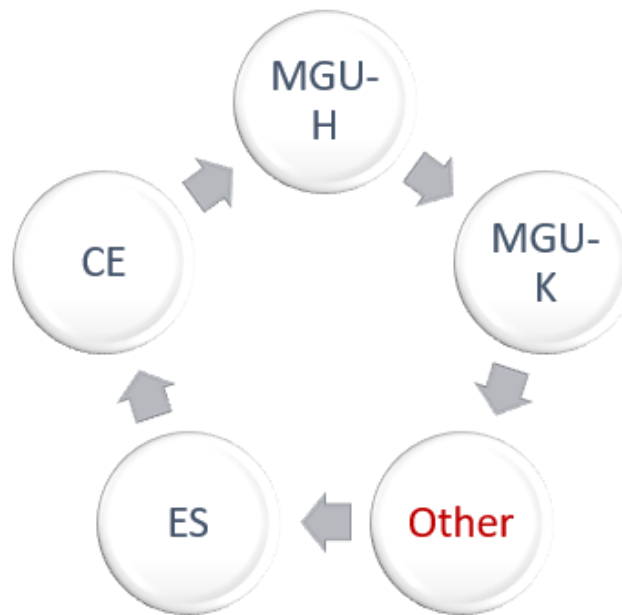


*Figure 3.3 The scheme of other harvesting energy*

# Chapter 4

## 4. Electromagnetic effects for other harvesting energy

### 4.1 Introduce

The development of long-term power solutions will become increasingly important in the future. The demand for alternative methods of electricity generation continues to grow, and energy storage facilities offer promising solutions. In recent years, research focusing on energy accumulation and many popular issues has grown exponentially. Energy storage, in various forms, has been around for a long time. Well-known examples are wind energy using wind turbines, hydropower using wind turbines and solar power from the sun. But with the current emphasis on clean energy to reduce fuel consumption and preserve the environment, alternative energy sources need to be explored and distributed, even if their numbers are limited a prominent example is electricity harvesting, discovered by Faraday in 1831. In this way the Electric current produced Coils are often used as conductors, electricity is transmitted by changing the magnetic field around the coil or a magnetic field a are repositioned and generated. The amount of energy generated depends on factors such as magnetic field strength, speed at which magnetic field change, and number of coils involved. Electromagnetism can be classified which pointed out by Maamer et al. [18] as follows:

- 1- Moving coil/fixed magnet: the coil movement accomplished as: mechanical spring, rotation or displacement, vibrating structure.
- 2- Moving magnet/fixed coil: it is possible to move magnets by mechanical spring, without spring / move as free (unreservedly).
- 3-Magnetostriction: several ferromagnets exhibit magnetostriction which permit to convert magnetic energy into kinetic energy like Galfenol and Terfenol-D. It represents the relationship between the magnetic field and the applied stress.
- 4- Ferrofluid: it is a fluid possessing ferromagnetic characteristics and the most studied ferrofluids are water based ferrofluid (MSG W11) and hydrocarbon oil ferrofluids (EFH1).

Researchers have made significant efforts to explore and classify electromagnetism as an energy harvesting source. For instance, in 2018, MA. Halim et al. [19] designed, optimized, and characterized an electromagnetic energy harvesting device that utilized a sprung eccentric motor. This device was specifically designed to harvest power from pseudo-walking signals.

Similarly, LB. Zhang et al. [20] demonstrated a unique energy harvesting method in 2019. They presented a technique that captured energy from ambient vibrations resulting from mechanical motions and body movements. Their approach involved using a rolling magnet to cut coils, which resulted in a higher magnetic flux rate compared to a sliding magnet. The electric power source generated from this method had a working voltage of 1.1 V and could sustain operation for up to two minutes, harnessing energy harvested from a minute of hand shaking. In 2021, Jin, X. et al. [21] introduced a novel technique for harvesting magnetic energy using a Triboelectric Nanogenerator (TENG). The TENG utilized magnetic balls rotating around a core to capture magnetic energy from transmission lines. When exposed to the alternating magnetic field generated by the transmission line, the magnetic ball rolled within a spherical shell, resulting in an output power of 1.5KV and 6.67 mW per single TENG unit.

Furthermore, Z. Wang et al. [22] proposed an energy-monitoring system in which the electromagnetic energy of the rotor is measured by installing coils on the bogie frames. In this system, the coils and magnetic field move relative to each other, facilitated by a counterweight acting as a friction pendulum. This arrangement simplifies the mounting process of the device onto the wheelset. The output power achieved under train speeds ranging from 420 to 820 rpm was approximately  $1982 \text{ W} \cdot \text{m}^{-3}$ .

These notable studies highlight the ongoing endeavors of scientists and researchers to explore and harness the potential of electromagnetism as an energy harvesting source. By developing innovative devices and techniques, they contribute to the advancement of energy harvesting technologies and pave the way for sustainable and efficient power solutions in the future.

## **4.2 Characterization of electromagnetic harvesting energy**

Electromagnetic energy harvesters heavily rely on the interaction between coils and magnets to capture and convert energy. Specifically, these devices are engineered to extract energy from the rotational motion of a wheel. Building upon the classification of research by Maamer et al. [18] about second point of his research in electromagnetism, it becomes feasible to construct a rotating magnet that derives its power from the wheel's rotation. Simultaneously, the coils remain fixed in position, allowing for the efficient extraction of energy from this setup

This setup can be applied in distinct designs:

1- Radial Design (RD): In this layout, the coils are arranged in a radial sample around the rotating magnet. As the wheel rotates, the magnet spins, causing a changing magnetic field to

skip through the coils. This effects in the technology of an electrical present within the coils, which may be harnessed as harvested power.

2- Axial Design (AD): In the axial layout, the coils are located along of the axis of rotation of the wheel (inside Rim of wheel). The rotating magnet passes through the coils because the wheel turns, inducing a converting magnetic area inside the coils. This, in turn, results an electric present within the coils, which may be captured and applied as electricity.

### 4.3 Simulation of electromagnetic harvesting energy

#### 4.3.1 Radial Design (RD):

In this setup, the coil, which possesses resistance  $R_c$  is fastened to half of the bottom of the wheel using a rod, as depicted in Figure 4.1 on the other hand, the magnet, driven by the rotation of the wheel, is affixed to the wheel's edge.



*Figure 4. 1 The simple drawing about placement of magnetic and coil for RD case*

To commence the modeling and calculation of the magnet's motion, it is essential to depict the schematic diagram of the wheel. Please refer to Figure 4.2, for the illustration of the wheel. When the wheel initiates its rotation, the magnet also begins to rotate while exhibiting a swing angle ( $\theta$ ) with respect to time ( $t$ ). The speed of the magnet inside the wheel can be defined as follows:

$$v = r \cdot \theta' \quad (4.1)$$

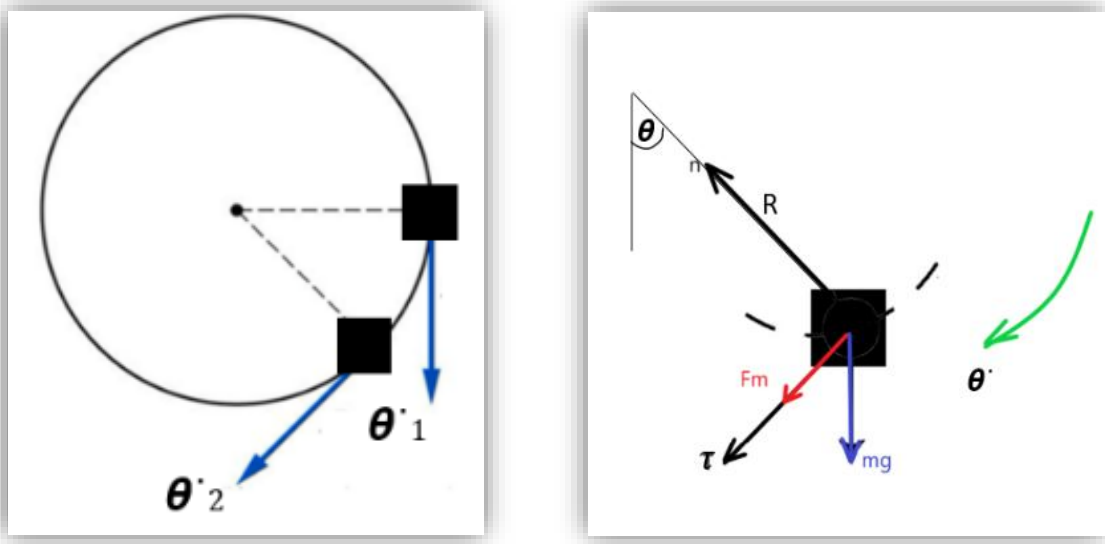


Figure 4. 2 The free body drawing of the magnetic inside coil in  $\hat{n}$  and  $\hat{\tau}$  coordinator system

Based on the second Newton law, the following can be written:

$$m \cdot \hat{a} = \sum_{i=1}^n \hat{F}_i \quad (4.2)$$

$$m \cdot r \cdot \theta'' + K_v \cdot r \cdot \theta' = F_m + m \cdot g \cdot \sin \theta \quad (4.3)$$

The electromagnetic force ( $F_m$ ) produced by an integrated coil length within a magnetic field.

$$F_m = I \cdot l \cdot B_{ex} \quad (4.4)$$

The magnetic field is calculated in the center of wheel and gives as the following equation:

$$B = \frac{\mu_0 I}{4\pi r^2} \int_0^\pi dl \quad (4.5)$$

Also, the magnetic field for half arc of wheel gives as:

$$B = \frac{\mu_0 I}{4\pi r^2} \int_0^\pi r \cdot d\theta = \frac{\mu_0 I}{4\pi r} \cdot \theta \quad (4.6)$$

So that we can write the electromagnetic force according to:

$$F_m = \frac{\mu_0 l \theta I^2}{4 \pi r} = K_m \cdot \theta \cdot I^2 \quad (4.7)$$

$$m \cdot r \cdot \theta'' + K_v \cdot r \cdot \theta' = K_m \cdot \theta \cdot I^2 + m \cdot g \cdot \sin \theta \quad (4.8)$$

$$\theta'' + \frac{K_v}{m} \theta' = \frac{K_m}{m \cdot r} \cdot \theta \cdot I^2 + \frac{g}{r} \cdot \sin \theta \quad (4.9)$$

$$\theta'' + \frac{K_v}{m} \theta' - \frac{K_m}{m \cdot r} \theta \cdot I^2 - \frac{g}{r} \cdot \sin \theta = 0 \quad (4.10)$$

$$\theta'' + K_1 \theta' - K_2 \theta \cdot I^2 - K_3 \sin \theta = 0 \quad (4.11)$$

To effectively simulate this design using Simulink, it is essential to know the values of  $K_1$ ,  $K_2$ , and  $K_3$ , as specified in table 2.1. These values correspond to the measured parameters necessary for our simulation.

Table 1. 1 Measured parameters for simulation radial design

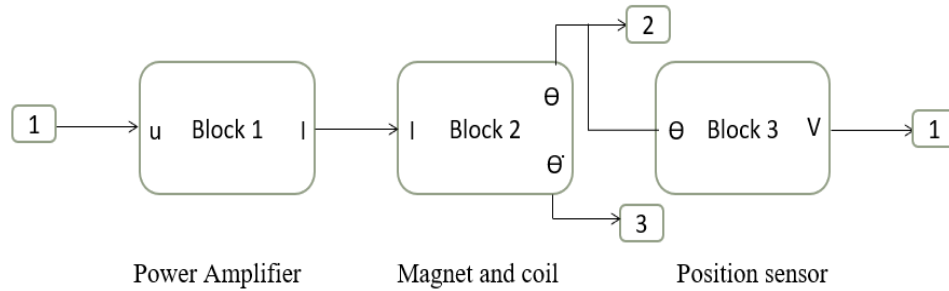
Name	Notation	Value and unit
Mass of magnetic	m	0.01 Kg
Length of coil	l	10 m
Radius of wheel	r	0.1925m
Magnetic permeability	$\mu_0$	$4\pi \cdot 10^{-7}$ H/m
Coil inductance	L	10 H
Copper coil Resistance	$R_c$	0.17 $\Omega$

In the study conducted by JA Calvo et al. [23], his research presented a value, denoted as  $K_v$ , for a comfortable car within the range of 0.20 to 0.25

Table 1. 2 The last values for equation 4.11

$K_1$	22.5 (N.s.m <sup>-3</sup> )
$K_2$	2,755. $10^{-7}$ (rad <sup>-2</sup> sec <sup>-2</sup> A <sup>-2</sup> )
$K_3$	51.49 (sec <sup>-2</sup> )

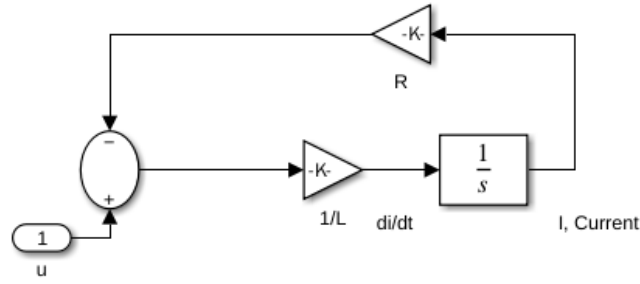
The components of this system can be described as following:



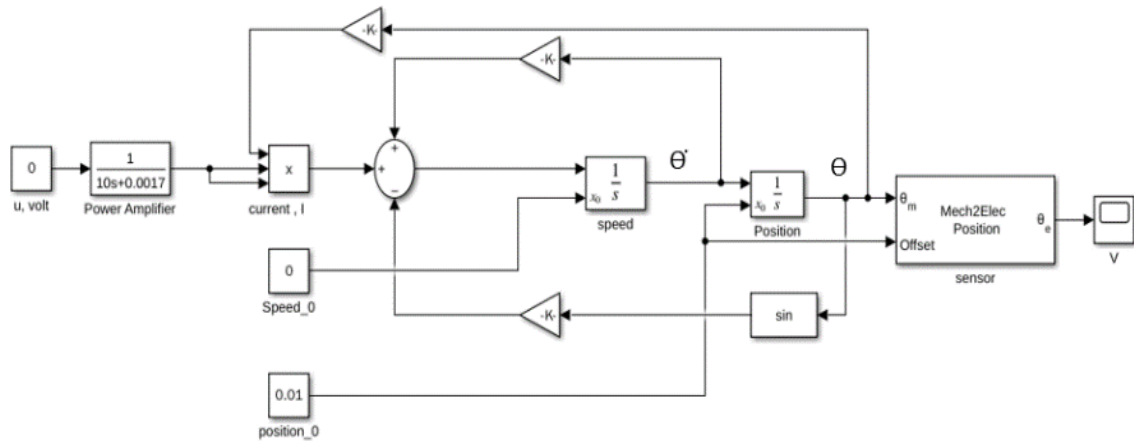
The block (1) elucidates the relationship between current (I) and voltage (U) in an amplifier that incorporates both resistance and inductance. This relationship is expressed by the following equation:

$$\frac{I}{U} = \frac{L}{s + \frac{R}{L}} \quad (4.12)$$





The Simulink for blocks (2 &3) can be shown as follows:



We observed an increase in peaks at the onset of moving the magnet inside the coil. The response time chart shows that the extracted output voltage is approximately 1.05 volts, which is slightly lower than expected based on this study. This voltage level is sufficient for small applications in automotive systems; however, further investigation is necessary. Therefore, we should explore alternative designs as study in axial design to optimize performance and assess their potential.

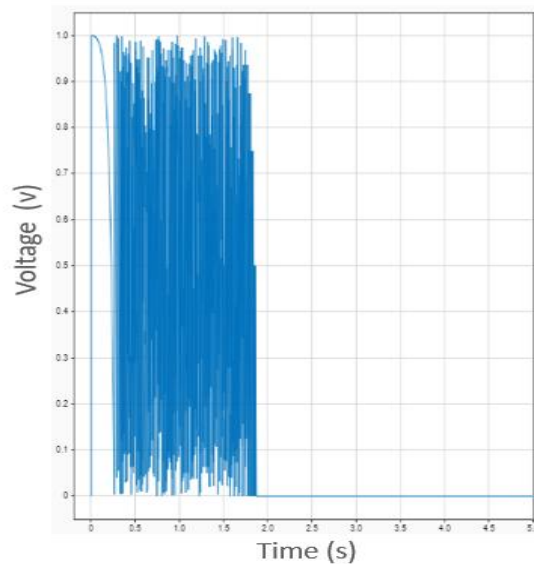


Figure 4. 3 The response of system according to time

### 4.3.2 Axial Design (AD):

In this setup, the coil is typically placed on the spokes of the wheel's hubcap, while the magnet is positioned inside the coil, as depicted in a provided Figure 4.4, when the wheel rotates, the magnet moves in a linear motion within the coil. This movement creates a changing magnetic field, which, according to the principles of electromagnetic induction, induces an electric current in the coil.



Figure 4. 4 The simple drawing about placement of magnetic and coil for AD case

The magnetic movement inside the spokes of hubcaps without a coil is shown in Figure 4.5

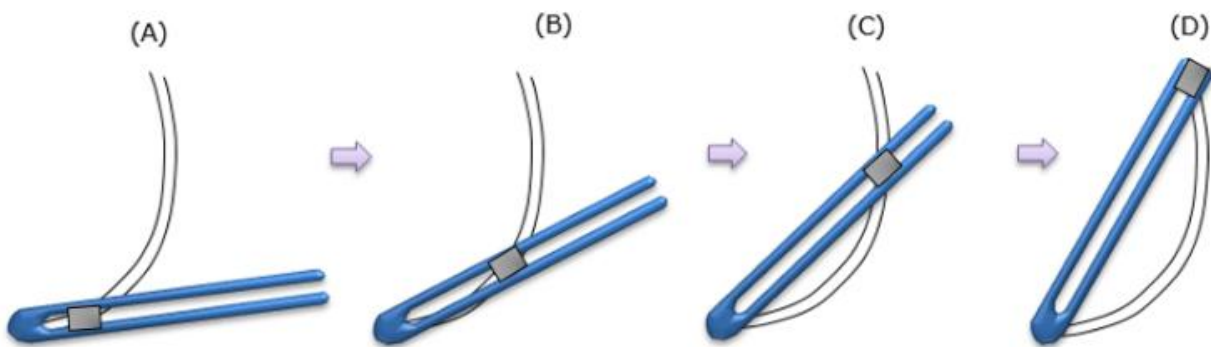


Figure 4. 5 The motion of the magnetic inside the spoke without a coil

Let's focus on the motion being studied, which is similar to the research Donoso, et al. [24], In their study, they investigated the motion of a magnet falling inside a conductive pipe. In our article, we refer to this motion as "Curvilinear motion in polar coordinates  $(r, \theta)$ " When a particle moves along a curvilinear path, it is often convenient to use polar coordinates  $(r, \theta)$  to analyze its instantaneous velocity and acceleration. Polar coordinates are particularly useful because they account for the changing distance of the particle from a reference point as a function of the angle. The shape of the path along which the particle is constrained affects its distance from the reference point. By expressing the motion in terms of polar coordinates, we

can mathematically describe the particle's position, velocity, and acceleration at any given moment along the curvilinear path. The distance between the center of the wheel and the magnet positioned on the spoke is represented as ( $r$ ). The free body of magnetic shown in Figure 4.6, and Acting forces belong to the free-body-diagram.

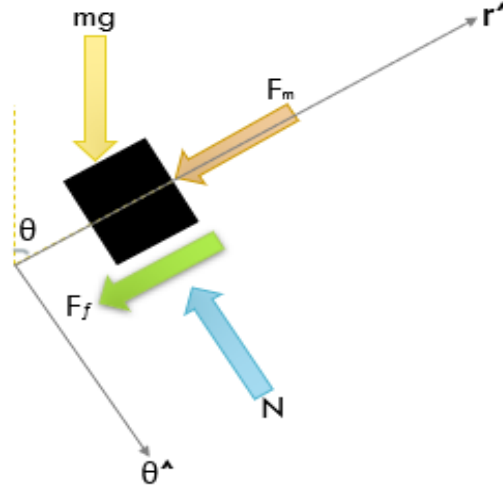


Figure 4. 6 The free body drawing of the magnetic for AD case in  $\hat{r}$  and  $\hat{\theta}$  coordinator system

let's analyze the equation that describes the radial motion (rotation) in the direction of  $\hat{r}$ . By applying Newton's second law of motion, we can examine the behavior of magnets. To do this, we must be studying the total force acting on the magnet in the radial direction ( $r$ -direction) is equal to the product of its mass and the radial acceleration. In other words, we can use Newton's second law, which states that the net force acting on an object is equal to its mass multiplied by its acceleration. In this case, we specifically consider the forces acting on a magnet in the radial direction (along the  $r$ -axis). The equation allows us to calculate the resulting acceleration of the magnet in response to these forces. This approach enables us to describe and analyze the motion of magnets in terms of Newton's laws of motion, considering the radial forces and their corresponding acceleration along the  $r$ -direction.

$$m \cdot \hat{a}^r = \sum_{i=1}^n \hat{F}^r \quad (4.13)$$

$$a^r = (r'' - r \theta'^2) \quad (4.14)$$

$$m \cdot (r'' - r \theta'^2) = -F_f - F_m - m \cdot g \cdot \cos \theta \quad (4.15)$$

$$m \cdot r'' - m \cdot r \theta'^2 + F_f + F_m = -m \cdot g \cdot \cos \theta \quad (4.16)$$

The total force acting on the magnet in the  $\theta$ -direction (angular direction) is equal to the product of its mass and the angular acceleration. Based on Newton's second law of motion the tangential component of the vector gives as:

$$m \cdot \hat{a}^\theta = \sum_{i=1}^n \hat{F}^\theta \quad (4.17)$$

$$a^\theta = (r \cdot \theta'' + 2 r' \theta') \quad (4.18)$$

$$m \cdot (r \cdot \theta'' + 2 r' \theta') = -N + m \cdot g \cdot \sin \theta \quad (4.19)$$

$$m \cdot r \cdot \theta'' + 2 m \cdot r' \cdot \theta' + N = m \cdot g \cdot \sin \theta \quad (4.20)$$

By referring to equations (4.16) and (4.20), we gain the ability to calculate and analyze forces based on specific conditions. These equations provide the necessary framework for determining forces under different scenarios, such as when the object is at rest or when it is in motion with defined starting ( $r_1$ ) and ending ( $r_2$ ) conditions.



Figure 4.7 The position of magnetic when entry and exit motion

Equation (4.16) likely represents a mathematical relationship that allows us to calculate forces or determine their behavior under certain conditions. Similarly, equation (4.20) likely provides another equation or expression that aids in the calculation or analysis of forces in specific situations. By utilizing these equations in conjunction with the given conditions, we can calculate and handle forces accordingly. This enables us to understand the forces acting on an object at rest or during specific motions, taking into account the initial and final positions ( $r_1$  and  $r_2$ ) as well. In summary, equations (4.16) and (4.20) provide the necessary tools for calculating and managing forces based on conditions at rest and for certain motions, allowing us to analyze and understand the behavior of forces in different scenarios.

### **Friction force:**

It is related to kinetic coefficient of friction ( $\mu$ ) and with the sign of radial velocity ( $r'$ ).

$$F_f = \mu \cdot N \cdot (r') \quad (4.21)$$

When :  $r' > 0$  , the magnetic toward to top of spoke

When :  $r' < 0$  , the magnetic toward to down of spoke

When :  $r' = 0$  , the magnetic at the rest

### Normal force:

It is related to radial and angular velocity as well as angular acceleration. Here are the calculations we can make based on equation (4.20).

$$N = -m.r.\theta'' - 2m.r'\theta' + m.g.\sin\theta \quad (4.22)$$

There is no difference between a magnet moving or a magnet stationary relative to the tube wall when it comes to this equation for normal force.

### Electromagnetic force:

In the research conducted by J. Cannarella et al. [25], it was found that the coupling factor is related by the electromagnetic force to the current flowing through the coil.

$$\gamma_r = \frac{F_m}{I}$$

So that the electromagnetic force can right as:

$$F_m = \gamma_r \cdot I \quad (4.23)$$

As Faraday Law of induction, the induced voltage in coil moving in magnetic field gives as.

$$\varepsilon = \oint (\mathbf{r} \times \mathbf{B}) \cdot d\mathbf{l} \quad (4.24)$$

In figure 4.8, it refers how does a coil, a magnet, and the magnetic field around the magnet look like

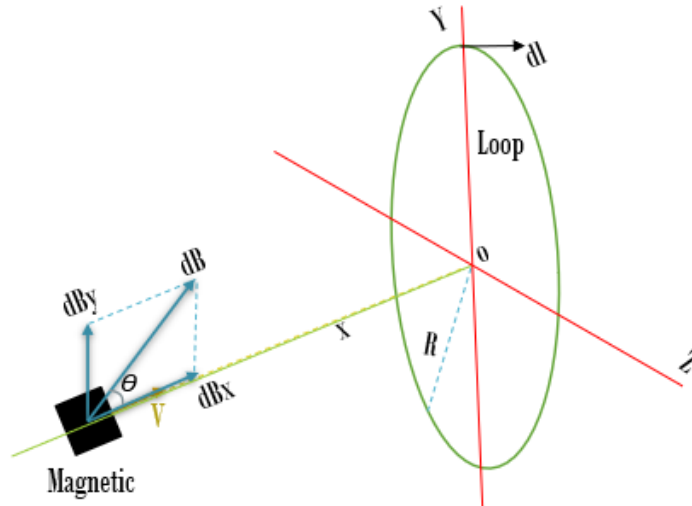


Figure 4.8 The magnetic field between the coil and magnetic

The radial velocity is denoted as ( $r'$ ), indicating the rate at which the distance from the center ( $r$ ) changes with time. The magnet experiences an electromagnetic drag force, which is a force opposing its motion, causing power to be transferred into the electrical circuit. According to the principle of conservation of energy, the power lost from the magnet due to this drag force is equal to the power transferred into the electrical circuit. In other words, as the magnet moves

radially, it experiences a drag force due to electromagnetic interactions. This drag force results in the dissipation of power, which is transmitted into the electrical circuit connected to the magnet. According to the conservation of energy, the power lost by the magnet due to this drag force is equal to the power gained by the electrical circuit. This principle highlights the transfer of energy from the magnet to the electrical circuit and ensures that energy is conserved in the system. It signifies that the power dissipated by the magnet due to the electromagnetic drag force is accounted for by the power absorbed by the electrical circuit.

$$\begin{aligned}\varepsilon \cdot I &= \mathbf{r}' \cdot \mathbf{F}_m \\ \varepsilon \cdot I &= \mathbf{r}' \cdot \gamma_r \cdot I \\ \gamma_r &= \frac{\varepsilon}{\mathbf{r}'}\end{aligned}\tag{4.25}$$

By replacing the equation (4.25) into (4.24) and dropping each of vectors in coordinator system (x, y, z) we found:

$$\gamma_r = \oint (B_\chi) dl \tag{4.26}$$

Depending on the researchers Zhang, Y et al. [58] which show the analysis of magnetic field in spiral pipe, we determine the magnetic flux density in two conditions:

1.  $B = \text{constant}$  for all loops:

$$\gamma_r = B_\chi \cdot L$$

(For one loop)

$$\begin{aligned}B_\chi &= \frac{\mu_0 I R^2}{2 \sqrt{(X^2 + R^2)^3}} \\ \gamma_r &= \frac{\mu_0 I R^2 \cdot L}{2 \sqrt{(X^2 + R^2)^3}}\end{aligned}\tag{4.27}$$

2.  $B \neq \text{constant}$  for loops of coil:

Many researchers have tried to determine the value of the coupling factor by experimental methods, but it is not possible to give information about how changing the harvester's geometry or influenced by coil dimensions [59, 60]. There are some sources that use elliptic integrations and numerical integrations as researcher Sneller and Mann [26] that point us following equation:

$$\gamma_r = \frac{1}{l} \oint (B_\chi dl) \cdot l \tag{4.28}$$

For the volume we can write the equation (4.28) as.

$$\gamma_r = \frac{1}{v} \oint (B_\chi dv) \cdot v \tag{4.29}$$

To calculate the volume of the coil in cylindrical coordinates and according to an illustration of the distance's relationship between the magnetic and coil we can write:

$$\begin{aligned}
 v &= R \cdot dR \cdot da \cdot d\theta \\
 \gamma_r &= \frac{1}{v} \oint (B_x dv) \cdot v \\
 &= \frac{1}{v} \oint \left( \frac{\mu_0 I R^2}{2 \sqrt{(X^2 + R^2)^3}} dv \right) v \\
 &= \frac{1}{v} \iiint \left( \frac{\mu_0 I R^2}{2 \sqrt{(X^2 + R^2)^3}} dv \right) R \cdot dR \cdot da \cdot d\theta \\
 \gamma_r &= \frac{1}{v} \iiint \left( \frac{\mu_0 I R^3}{2 \sqrt{(X^2 + R^2)^3}} dv \right) \cdot dR \cdot da \cdot d\theta \quad (4.30)
 \end{aligned}$$

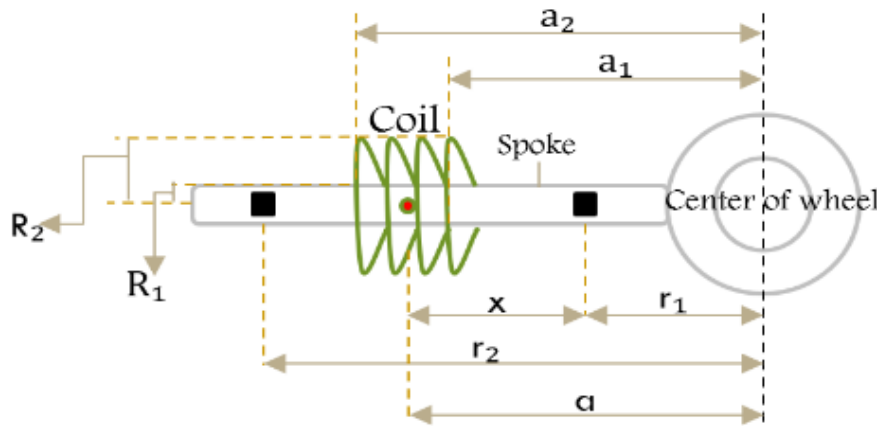


Figure 4.9 The dimensions between the magnet and the coil

#### 4.4 Experiment of axial design electromagnetic harvesting energy

To start the experiment for this model, we need to access two tests.

##### 4.4.1 Free falling test

We can test this energy-harvesting model by using a free-fall magnet on a coil, and let's study this hypothesis from equation (4.16).

$$\begin{aligned}
 m \cdot r'' + F_m &= -m \cdot g \\
 m \cdot r'' + \gamma_r \cdot I_r &= -m \cdot g \quad (4.31)
 \end{aligned}$$

The PP pipe, disk magnetic and copper coil that is used in this experiment shows in Figure 4.10, around the pipe, in the center, a coil bobbin is placed, and within the pipe, the magnetic is found. various load resistors connected to coil terminals were used to compare model predictions with measured voltages. Whenever the magnetic touch the pipe wall, we must

repeat the test from the beginning. Each resistor uses a certain amount of energy which can be calculated from a measured voltage as:

$$E = \int_0^t P \cdot dt = \int_0^t \frac{U}{R} \cdot dt \quad (4.32)$$

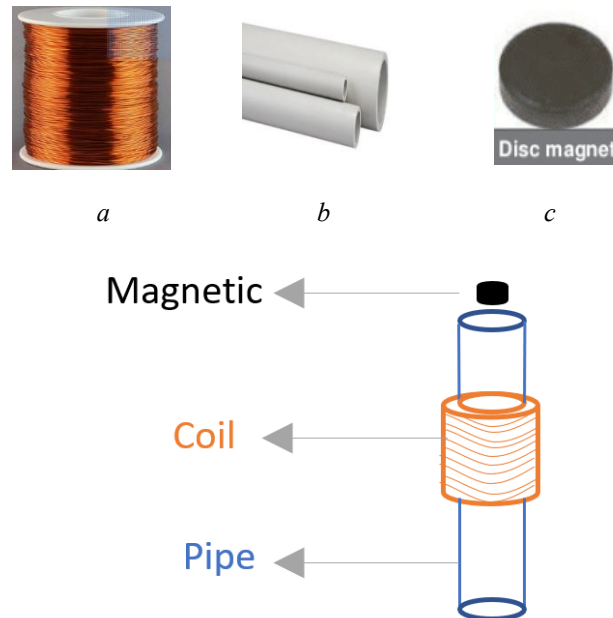


Figure 4.10 The components for free falling test (a. the coil, b. the PP pipe, c. the disc magnet)

The Characteristic of each component in this test can show in the schedules:

Table 1. 3 The specification about disc magnet in free falling test

H (High)	19 mm
D (Diameter)	12.5 mm
m (mass)	18.5 Kg
length of dropping the magnetic	160 mm

Table 1. 4 The specification of the coil in free falling test

H (High)	30.2 mm
R (resistance)	429 $\Omega$
L (inductance)	0.98 H
$R_1$ (the inner radius of the loop)	13.1 mm
$R_2$ (the outer radius of the loop)	27.6 mm
$a_1$ (the beginning radial position of the coil)	58.4 mm
$a_2$ (the last radial position of the coil)	88.6 mm

Table 1. 5 The specification of the PP pipe in free falling test

Type	Poly Propylene grey RAL 7032 DN 150
Length	153 mm



When the magnetic move through the pipe there is a dipole moment magnetic according to K&J Magnetics [27] which can calculate from the next equation:

$$M = \frac{V_m \cdot B_r}{\mu_0} \quad (4.33)$$

The value of this parameter exhibits significant variation across different companies, contingent upon the strength of the magnetic field. For our testing purposes, we can calculate the dipole moment value using the aforementioned equation and determine it to be 2.2 A m<sup>2</sup>. We selected a time interval ranging from 0 to 4.5sec, with a resistance of 500  $\Omega$ .

In this test there is an "overshoot" present in the curves when the magnet passes through the coil and the voltage returns to zero. Reversing the direction of the pipe leads to a reversal in the magnet's movement when it reaches the end of the tube. Consequently, the voltage does not increase significantly, resulting in minimal impact on the average energy according to figure 4.11

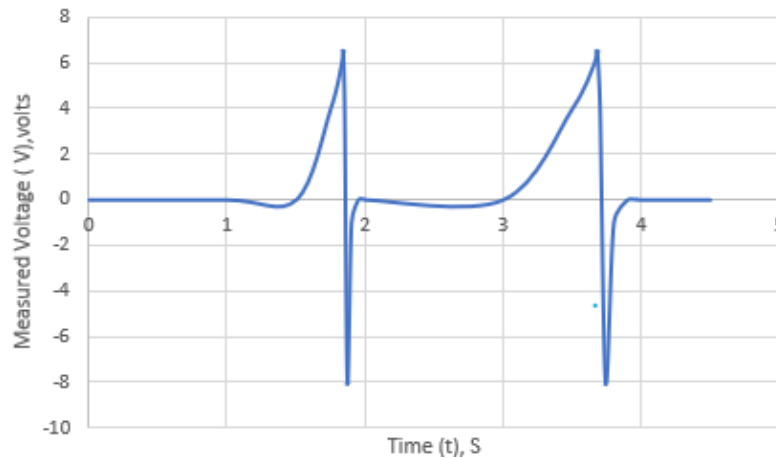


Figure 4.11 The response system according to time

#### 4.4.2 Rotation motion test

Depending on equations (4.16) & (4.20) and Similar to the component of the first test we use also the disk magnetic, pipe P.P., Load resistance ( $R_{load}$ ) 170  $\Omega$ . and coil. We add here the device for the counter of rotation (Tachometer), and a counter sensor for touch magnetic at the last position of the pipe as pointed in Figure 4.12. Also, there is a wireless DAQ device 9191 measures the voltage and transfers the values to a laptop.

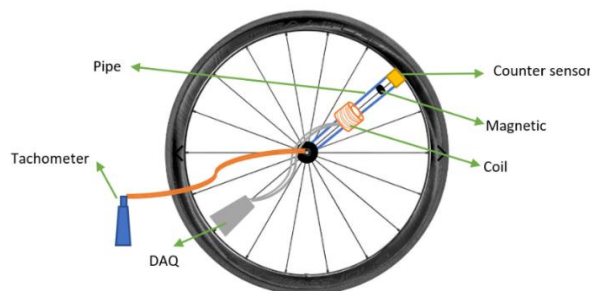


Figure 4.12 The components for rotation motion test

The Characteristic of each component in this test can show in the schedules:

Table 1. 6 The specification of disc magnet in rotation motion test

H (High)	19 mm
D (Diameter)	12.5 mm
m (mass)	18.5 Kg

Table 1. 7 The specification of the coil in rotation motion test

H (High)	30.2 mm
R (resistance)	429 $\Omega$
L (inductance)	0.98 H
$R_1$ (the inner radius of the loop)	13.1 mm
$R_2$ (the outer radius of the loop)	27.6 mm
$a_1$ (the beginning radial position of the coil)	77.8 mm
$a_2$ (the last radial position of the coil)	103.0 mm

Table 1. 8 The specification of the PP pipe in rotation motion test

Type	Poly Propylene grey RAL 7032 DN 150
Length	153 mm

These graphs in figure 4.13, depict the calculated effort over a duration of 60 seconds. As the number of wheel rotations increases, more voltage curves are observed. However, towards the end, irregularities in the peaks occur due to the presence of friction.

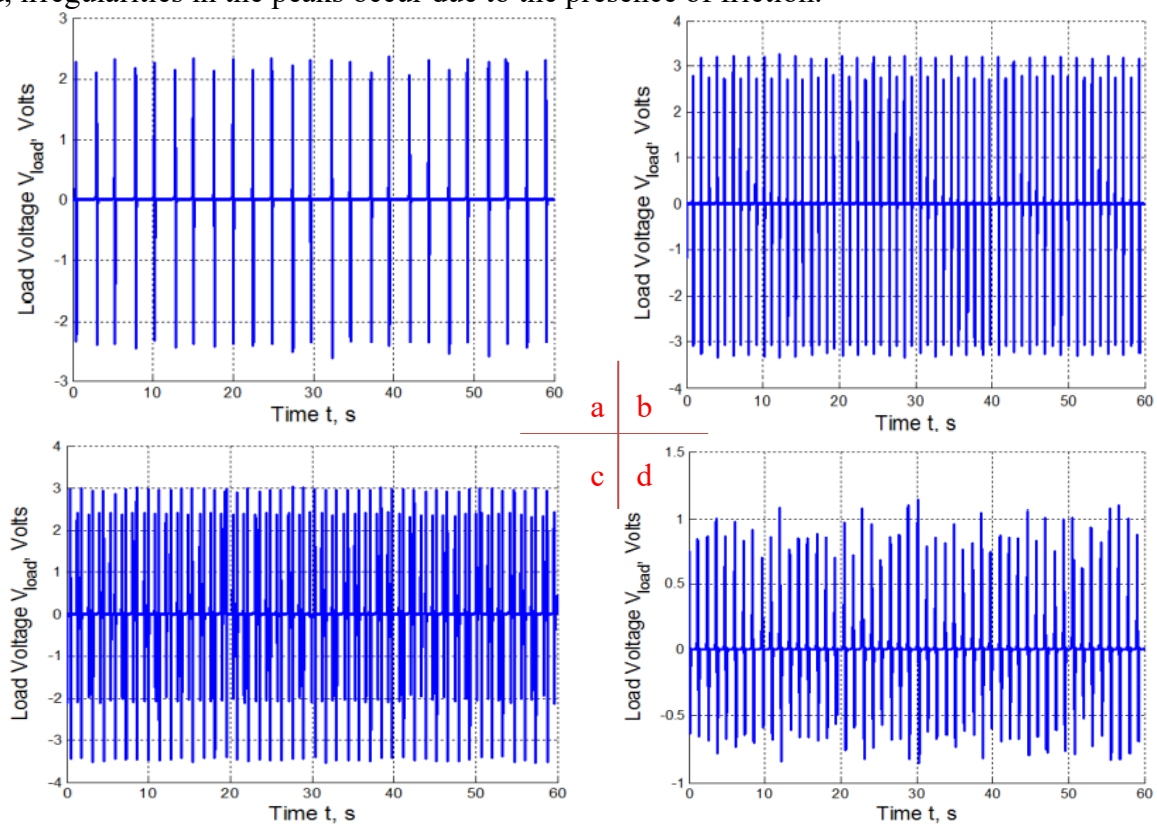


Figure 4.13 The response system according to time for rotation motion test for

(a.23 rpm, b.27 rpm, c.42 rpm, d.49 rpm)

#### 4.5 Results of electromagnetic harvesting energy

Illustrates the results of finding the energy using different resistances can be shown in the Figure 4.14

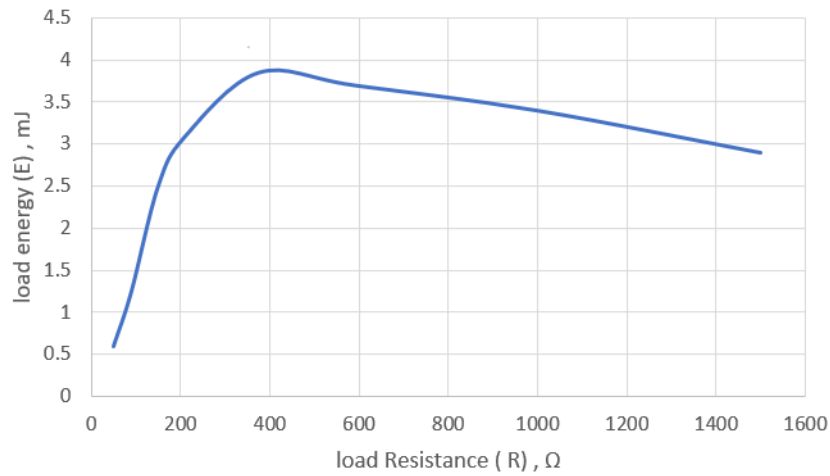


Figure 4.14 The relationship between the power and resistance

Any spoke and any rotation of a wheel can produce power according:

$$P = V^2/R \quad (4.34)$$

The maximum energy value as 3.77 mJ for free fall test and the coil's resistance 429  $\Omega$  as 3.74 mJ, the difference between maximum and coil values is 0.03. Thus, to estimate the maximum energy output, it is preferred to use a load resistance equal to the coil resistance. In a previous instance with the same coil resistance, a value of approximately 2.5 mW was obtained for the Radial Design. Also, it is better to check the energy by friction and without friction which the Figure 4.15, refer about the load energy (mW) and number of rotation (RPM).

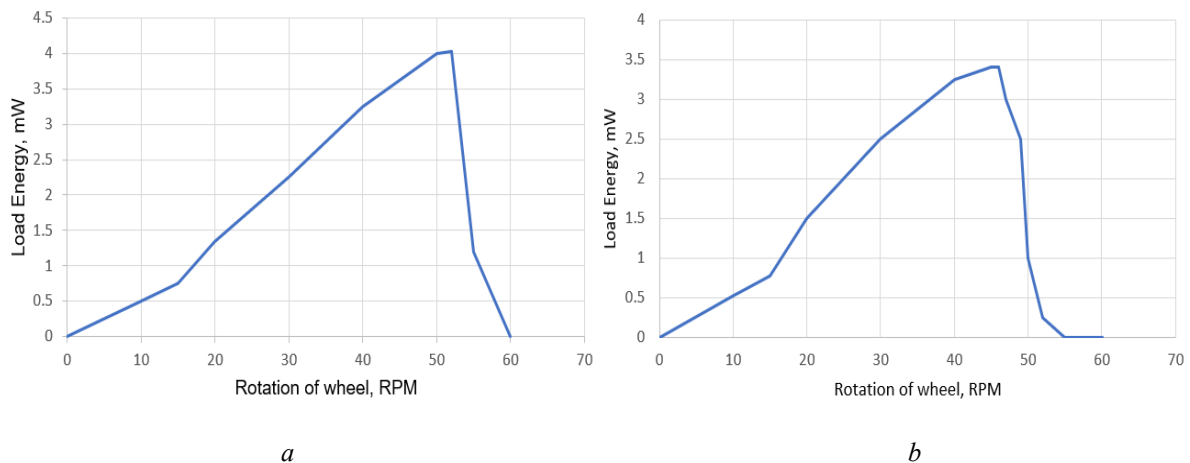


Figure 4.15 The relationship between the energy and rotation of the wheel for (a. without friction, b. with friction)

When the rotation of the wheel increases, the average amount of energy increases. In addition, we observe that the energy level declines sharply after the peak. During this decrease in energy, the magnet undergoes a centrifugal force to overcome gravitational pulling. Consequently, the

magnet will not fall completely to the bottom. As a result of the model without friction, the output of energy is about 4.02 mW at 53 RPM, but as a result of the model with friction, the output of energy is about 3.4 mW, and of course that is because we have the static friction coefficient when the magnetic starts sliding, and the kinetic friction coefficient on the magnet as it moves.

#### **4.6 Conclusion**

Through our investigation of the RD design, we observed that the motion of a magnet, induced by the rotation of a wheel, can generate approximately 2.5 mW of energy with 2% error based on the magnetic dipole value. This energy is produced within a stationary coil connected by a rod, and our findings indicate that the energy output varies with the resistance of the coil. The model for this design was developed using Simulink-MATLAB. This model also allows for simulations that incorporate the output voltage, which was calculated using Faraday's law and an equation for the magnetic field

In the case of an alternative AD design, we discovered that the direction of the wheel significantly influences the movement of the magnet within the fixed coil, leading to energy generation. During the rotation experiment, this energy harvester produced 4.02 mW of power, with a 3% error observed between the experimental data and the model at a speed of 53 rpm. Additionally, the free fall experiment yielded approximately 3.77 mJ of energy. Looking ahead, there is potential for further advancements in this design that could enhance its efficiency for energy generation.

# Chapter 5

## 5. Piezoelectric effects for other harvesting energy

### 5.1 Introduction

Innovative approaches have been developed to meet the need for powering devices. Piezoelectric materials and their derivatives play an important role in addressing these challenges. Harvesting energy from vibrations is one of the simplest and most effective methods. These vibrations can be caused by human motion, vehicle movement, machinery, and other vibrating objects. Piezoelectric materials can convert mechanical energy into electricity. Some natural piezoelectric materials currently in use include quartz. Other piezoelectric materials, such as BaTiO<sub>3</sub> and lead zirconium titanate (PZT), find applications in modern electronic circuits.

Piezoelectric materials are smart materials that have the ability to convert mechanical stress or strain into electricity and vice versa. This means that when mechanical stress or strain is applied to a material, electricity is generated; conversely, applying an electrical potential to the material causes mechanical displacement. These phenomena are known as the direct piezoelectric effect and the reverse piezoelectric effect, respectively. In a piezoelectric system, the material acts on a variety of surfaces. These properties are characterized by the piezoelectric stress in constitutive equations in following:

$$\begin{aligned}\varepsilon_i &= S_{ij}^E \sigma_j + d_{mi} E_m \\ D_m &= d_{mi} \sigma_i + \xi_{ik}^{\sigma} E_k,\end{aligned}$$

Denoted as  $d_{mi}$ , which represent the conversion of mechanical stress to electrical. The subscript "i" indicates the direction of electrical energy discharge, while "m" indicates the direction of applied mechanical stress or deformation. Notably,  $d_{33}$  and  $d_{31}$  are two main constants associated with the 3-axis direction due to the poling of the piezoelectric material as refer that in Figure 5.1

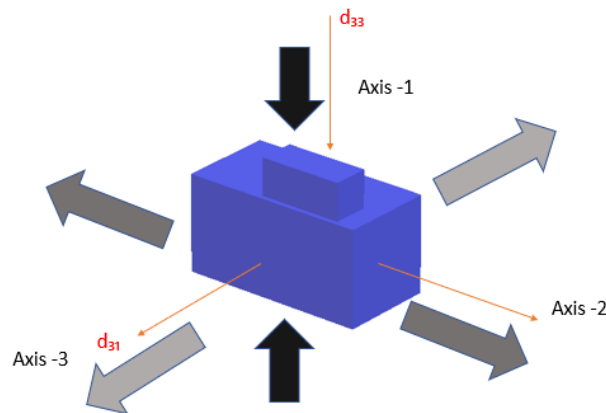


Figure 5. 1 The three-axis direction of the piezoelectric material by (Li, X., & Strezov, V., 2014) [57]

The authors proposed the idea of using piezoelectric energy harvesters to obtain electricity from vibrations. The energy collector contained a piezoelectric material that directly exhibited piezoelectric effects. A series of experiments was conducted to evaluate the efficiency of energy collection under different conditions. As Al-Yafeai, D., et al. [28] pointed out review explores the use of piezoelectric materials in car suspensions to capture and convert the mechanical vibrations and movements generated during vehicle operation into electrical energy. It discusses various design configurations and strategies employed in these systems to enhance energy harvesting efficiency. Darabseh, T., et al. [29] stated that simulation and experimental study of harvesting power from the car suspension system depending on piezoelectric method. They conducted tests on a time and frequency basis to evaluate the performance of the system. Using a half car model, they measured the maximum voltage and power generated at an excitation frequency of 1.46 Hz. The results showed that at this specific frequency, the system produced a maximum generated voltage of 33.56 V and a maximum power output of 56.35 mW.

Li, T., & Lee, P. S. [30] summarized to examine the key parameters that impact the performance of energy harvesting and provide guidance for future development. A universal theoretical model is developed, categorizing parameters into six groups. The review covers topics such as piezoelectric materials, including ceramics, polymers, single crystals, composites, nanomaterials, and lead-free materials, as well as their advantages, disadvantages, and material orientation. The discussion also encompasses structure designs (off-resonance, on-resonance, impact), sources of excitations and vibrations (direct contact force, low vibration force, hydraulic, pneumatic power, acoustic power), the effects of frequency and speed (high-frequency, high-speed conditions), the impact of electrical load on output power, and parameters related to energy accumulation.

## **5.2 Procedures types of design piezoelectric**

Piezoelectric materials [31] encompass a range of options such as quartz, BaTiO<sub>3</sub>, and Lead Zirconium Titanate. Among these materials, quartz generates the highest electrical output voltage in response to applied mechanical stress. However, its high cost makes it economically impractical for many applications. On the other hand, PZT materials are readily accessible at a low cost and deliver commendable results, making them a favorable choice for piezoelectric energy harvesting. PZT-5J material was chosen for its favorable availability and cost compared to other PZT materials. This selection ensures that the piezoelectric energy harvesting system remains economically feasible while still benefiting from the desirable properties of PZT materials.

We will examine two cases involving the incorporation of materials. The first case (single system) involves fixing the piezoelectric materials within the tire. In this approach, materials exhibiting the piezoelectric properties will be utilized only. The second case (dual system) use the piezoelectric and magneto strictive materials in vibration parts like engine or tiers. in this approach, the magneto strictive materials can convert the mechanical vibrations or strain experienced by the engine or tires into magnetic energy. The piezoelectric materials, in turn, can convert this magnetic energy into electrical energy. By combining these two effects, the

system maximizes the energy harvesting potential from the vibrating parts and enhances the overall energy efficiency of the vehicle.

### 5.2.1 Piezoelectric within the tire (first case)

In this particular case, PZT-5J modules with a thickness of 2mm are employed and strategically positioned along the inner circumference of the tire as figure 5.2. a. These modules experience mechanical stress as they are subjected to the significant load encountered by the tire, particularly in the contact patch area. The mechanical stress induces the generation of electrical voltage within the PZT-5J modules. This electrical voltage is then directed towards the battery for storage and future use. The operational sequence of the system is outlined in detail in Figure 5.2.b, illustrating the flowchart of its functioning.

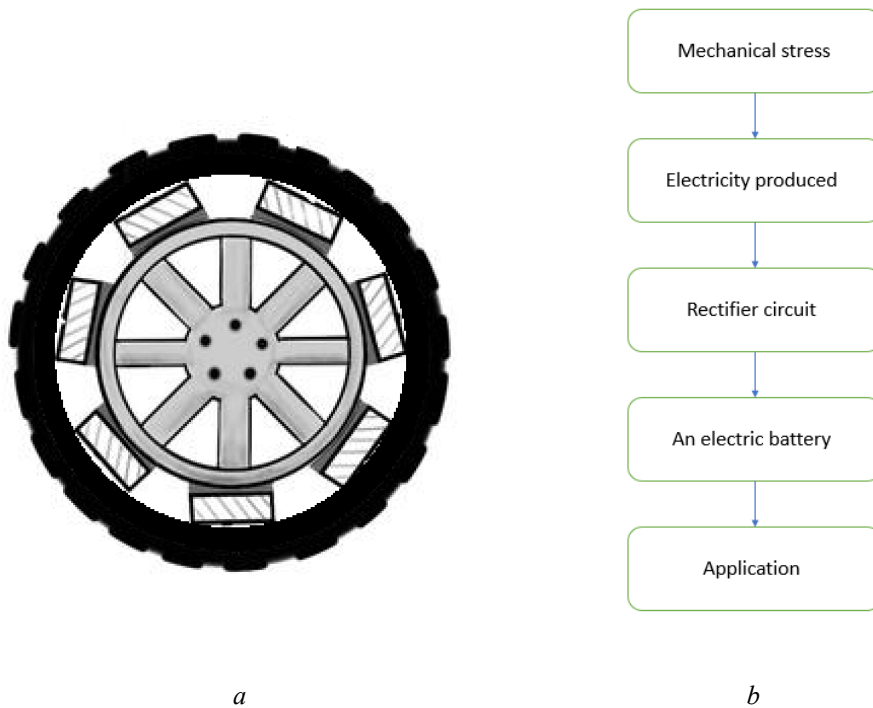


Figure 5. 2 The sketch and flowchart of operation sequence working for piezoelectric materials (first case)

### 5.2.2 Piezoelectric with magneto strictive materials (second case)

In this case, it includes piezoelectric and magnetoelectric materials. It is materials [32] that possess both magnetic and electric properties, and exhibit a coupling between them, are known to have a magnetoelectric effect. An important historical discovery in this field was made by Wilhelm Röntgen in 1888. Röntgen observed that dielectric materials could become magnetized when subjected to an electric field. These materials, which display intrinsic couplings between magnetic and electric phenomena, are commonly referred to as magnetoelectric materials.

## Magnetostriction:

The term "magnetostriction" [33] refers to the phenomenon where magnetic fields influence the dimensions of ferromagnetic materials. This effect was first observed by James Joule in 1842 while studying iron samples. Magnetostrictive materials possess the ability to convert electromagnetic energy into mechanical energy, and vice versa. This characteristic is utilized in the development of magnetic field sensors and force sensors. When a magnetic field or force is applied to a material, it induces strain within the material. This strain can be harnessed for various applications. For instance [34], Fe-Si-B-C-Sn alloys, known for their high saturation magnetic flux density and excellent thermal stability, are commonly used as magnetic cores in transformers.

Our device is constructed using a combination of magnetostrictive Fe-Si-B-C alloy ribbons and piezoelectric Pb (Zr, Ti) O<sub>3</sub> (PZT) fibers. The magnetostrictive component responds to magnetic fields, generating strain, while the piezoelectric fibers convert this mechanical strain into electrical signals. This integration allows our device to effectively sense and measure magnetic fields or forces, enabling a range of practical applications. By utilizing magnetostrictive and piezoelectric materials in combination, we can harness the advantages of both properties, resulting in a versatile and efficient device for various sensing and measurement purposes.

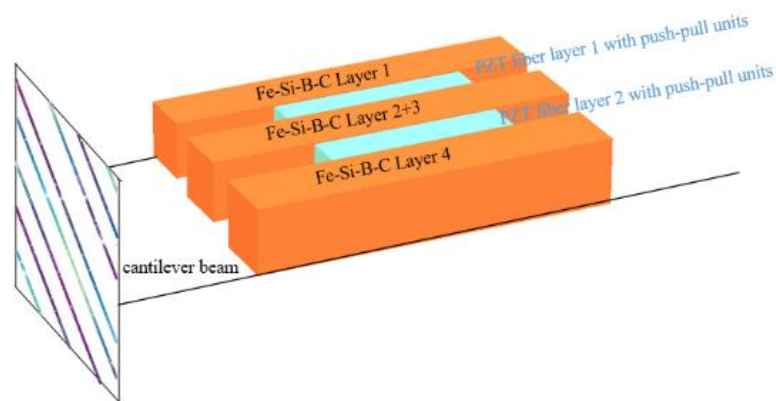


Figure 5. 3 The prototype working for piezoelectric materials (second case)

## **5.3 The calculation and experimental of piezoelectric harvesting energy**

### 5.3.1 First case

The Characteristic of PZT-5J from PIEZO company and depending on technical data sheet gives in table 2.1:

Table 2. 1 Characteristic of PZT-5J

Pizo electric charge constant	$d_{33} = 485 \times 10^{-12} \text{ C/m}^2$
Pizo voltage coefficient	$g_{33} = 21.3 \times 10^{-3} \text{ Vm/N}$
Resonant Thickness	$\tau = 2 \times 10^{-3} \text{ m}$
Curie Point	270 °C
Mechanical Quality Factor	60



Frequency Constants Radial	191 kHz · cm
Poisson's Ratio	0.31
Dielectric Constant (1kHz)	KT <sub>3</sub> =2100
Dielectric Loss Factor (1kHz)	0.2%
Clamped Dielectric Constant	800

The Characteristic of wheel which study in our experimental as in table 2.2:

Table 2. 2 Characteristic of wheel

Diameter	63,5 cm
Max Load	615 kg
Rev/Mile	831
Max PSI	3.5 bar

The behavior of piezoelectric materials can be described by a set of constitutive equations, which relate mechanical and electrical quantities. When the piezoelectric material is under mechanical stress, it generates a voltage. The relationship that leads to the open circuit voltage can be established from the electric field (E) generated in the material. The electric field (E) can be expressed in terms of the voltage ( $V_{oc}$ ) and the thickness ( $\tau$ ) of the material. Substituting E into the electrical displacement equation under open circuit conditions since no charge can flow, we arrive at the final equation for open circuit voltage for the PZT-5J as follow:

$$V_{oc} = g_{33} \times \tau \times \sigma \quad : \quad \sigma = \frac{F}{A'} \quad (5.1)$$

We need to understand that the tension in materials if it is subjected to pure tension as depending on equation (5.1) or can differ based on whether bending is involved as we found according to equation (5.2):

$$\sigma_b = \frac{M_{\sigma} \cdot d}{I_{\sigma}} \quad (5.2)$$

So that the total tension will be equal ( $\sigma_b + \sigma$ ) when there is bending. The value of open circuit voltage will be equal 0.81 volt without bending and 0.92 volt with the bending also the thickness of wheel about 0.05m

The relationship between mechanical stress ( $\sigma$ ) and the induced charge density per surface can be expressed through the piezoelectric constant (d) for the PZT-5J

$$\begin{aligned} C_d &= d_{33} \times \sigma_{total} \\ &= 0.01 \cdot 10^{-3} \text{ C/m}^2 \end{aligned} \quad (5.3)$$

In order to obtain uniform density in different tires, it is necessary to calculate the contact area of the tire with the ground.

$$A = \frac{F}{p} \quad (5.4)$$

$$= 0.01716 \text{ m}^2$$

So that the electric charge density it will be calculated according to (5.5) equation

$$C'_d = C_d \times A \quad (5.5)$$

$$= 0.01 \cdot 10^{-3} \times 0.01716$$

$$= 0.17 \mu\text{C}$$

The power due to piezoelectric cell compression can determine in equation (5.6), it is the amount of energy that can be obtained from straining or modulating a PZ cell.

$$P = \frac{V_{oc} \times C'_d}{t} \quad (5.6)$$

The value of power when there is bending for wheel it gives about  $0.16 \mu\text{W}$  for one sec and without bending it about  $0.13 \mu\text{W}$ .

The power generated by piezoelectric cells is influenced by stress and the contact area, as described by the equations and found in pervious study.

$$P = g_{33} \times \tau \times \sigma \times d_{33} \times \sigma \times A$$

$K = g_{33} \times \tau \times d_{33}$  : constant of piezoelectric material we can write as follow:

$$P = K \times \sigma^2 \times A \quad (5.7)$$

When different loads act on the cell, studying the stress and its calculation becomes crucial because increased stress leads to higher open-circuit voltage and charge density. This understanding is essential to gain insights into the behavior of piezoelectric cells under various loading conditions. To investigate the impact of stress on piezoelectric cells located on roads with electric voltage, we are conducting experiments to analyze their behavior under different loading conditions. Our research includes studying the effects of one-point loading, uniform distributed loading, and triangle-distributed loading on the piezoelectric cells. By simulating these different loading conditions, we aim to gain a comprehensive understanding of how the cells respond to the stress generated by passing vehicles on roads. Figure 5.4, provides an illustration of the different loading trucks used in our research and their corresponding loading conditions on the piezoelectric cells.

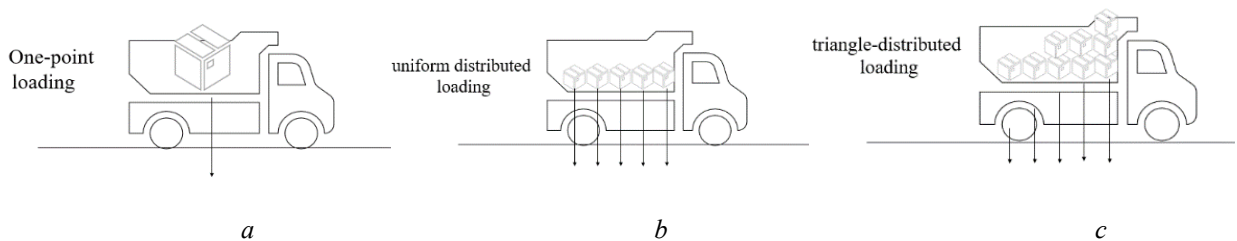


Figure 5. 4 The different loading truck on piezoelectric cells inside the roads. a). One point loading, b). uniform distributed loading, C). triangle distributed loading

Each stress vector ( $\hat{t}$ ) in indicial notation  $t_x, t_y$  in the coordinate system (X, Y) can be resolved into components along the coordinate lines and unit vector ( $i_x, i_y$ ):

$$\sigma_x i_x + \tau_{xy} i_y = t_x \quad (5.8)$$

$$\tau_{xy} i_x + \sigma_y i_y = t_y \quad (5.9)$$

Further research has been conducted on the implementation of finite and infinite elements [36] [37] [38] to enhance the analysis of piezoelectric cells. The objective of this analysis is to optimize the design and placement of these cells on roads, thereby maximizing their potential for energy generation. The finite and infinite element drawings presented in Figure 5.5, provide visual representations of the analysis conducted on the piezoelectric cells. These drawings serve as valuable tools in identifying areas of improvement, optimizing the design parameters, and ultimately maximizing the energy generation potential of the cells. The finite and infinite elements are represented as rectangular grid-like elements, not just simple line elements. The finite elements are depicted as rectangular grid cells, while the infinite elements are shown as extending beyond the finite grid, indicating they are used to model unbounded or open-ended domains. The transition between the finite and infinite element regions is also illustrated.

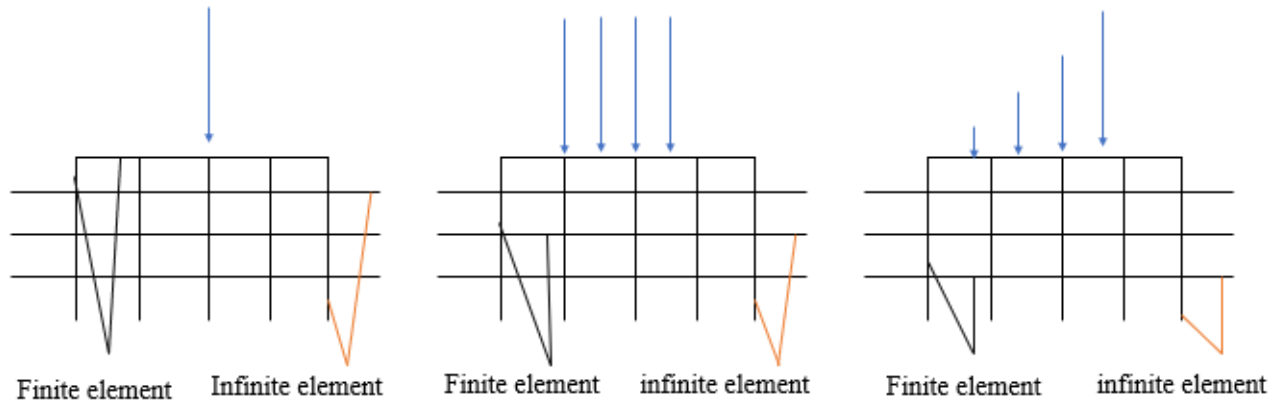


Figure 5. 5 Finite and infinite drawing under different loading

Resolving stress vectors into their normal and shear components can be a valuable approach. This involves breaking down the stress vector ( $\hat{t}$ ) into two separate components: one that is parallel to the normal of the surface element ( $n$ ), which is known as the normal stress ( $\sigma$ ), and another component that is perpendicular to the normal ( $n$ ), which is known as the shear stress ( $\tau^n$ ). We can gain a better understanding of how the stress is distributed across the surface and how it may impact the behavior of the piezoelectric cells [39] [40] [41].

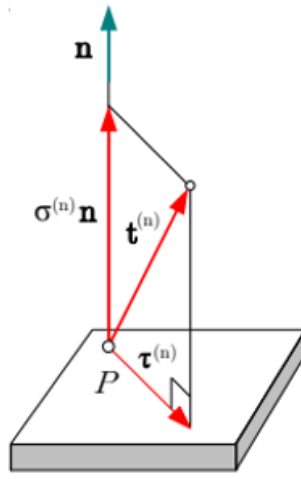


Figure 5. 6 Represents graphically the resolution of the stress vector  $t$  according to normal element

The equation of motion in coordinate system of  $x, y$  can give as:

$$\frac{\partial t_x}{\partial x} + \frac{\partial t_y}{\partial y} + \rho b = 0 \quad (5.10)$$

By substituting equations (5.8) and (5.9) into equation (5.10), we can obtain equilibrium equations in plane problems (5.11) and (5.12) that describe the stress vectors. This process involves expressing the stress vectors in terms of their normal and shear components. By doing so, we simplify the equations and make them more amenable to analysis. The resulting scalar equations offer a convenient method for calculating the magnitude of the stress vectors based on their normal and shear components. Instead of dealing with vector equations, we can now focus on scalar equations that directly relate to the normal and shear components of the stress.

$$\frac{\partial \sigma_x}{\partial x} + \frac{\partial \tau_{xy}}{\partial y} + f_x = 0 \quad (5.11)$$

$$\frac{\partial \tau_{xy}}{\partial x} + \frac{\partial \sigma_y}{\partial y} + f_y = 0 \quad (5.12)$$

When a vertical load ( $F$ ) is applied to the structure, it induces various stress components within the material. The horizontal normal stress ( $\sigma_x$ ) can arise due to the Poisson's effect, which is a consequence of the material's tendency to expand or contract in the perpendicular direction that compressed or stretched in one direction, while shear stresses account for critical factors such as sliding failure, material deformation, bending and torsion, failure criteria, and interaction effects. Understanding these aspects is essential for the design and analysis of safe and effective structures. The model illustrated in Figure 5.7, portrays undergoes various types of loading, including shear and stress forces.

The primary objective of this model is to investigate the behavior of piezoelectric cells under different stress conditions. The arrows depicted in the model represent diverse loadings, with varying magnitudes, applied to the medium to simulate distinct stress scenarios. By analyzing the response of the medium to these loadings, we can obtain valuable insights into the behavior of the piezoelectric cells under different stress conditions. This analysis allows us to understand how the cells deform and generate electrical energy in response to varying stress levels. Moreover, it aids in optimizing the design and placement of the cells.

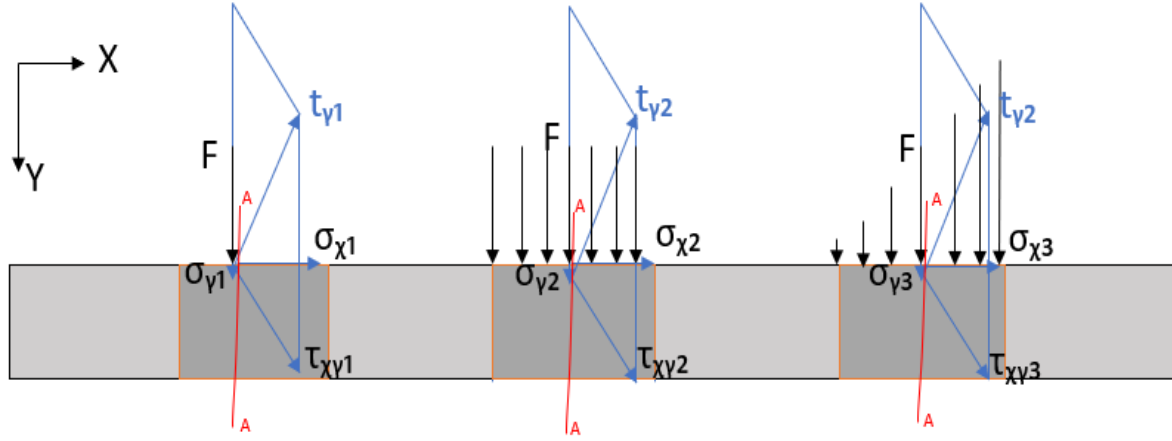


Figure 5. 7 infinite medium model that is subjected to various types of loading, shear and stress forces

By analyzing this stress distribution on the A-A section in the Figure5.7, we can obtain a deeper understanding of how the cell will react to different types and levels of pressure. This knowledge is crucial for optimizing the design and placement of the cells, ultimately maximizing their potential for energy generation.

For elastic material we can write:

$$\sigma = e. \epsilon \quad (5.13)$$

According to coordinator system (X, Y) we can write the equation (5.13) as follow:

$$\begin{bmatrix} \sigma_1 \\ \sigma_2 \\ \tau_{xy} \end{bmatrix} = \begin{bmatrix} c_{11} & c_{12} & 0 \\ c_{12} & c_{22} & 0 \\ 0 & 0 & c_{33} \end{bmatrix} \begin{bmatrix} \epsilon_1 \\ \epsilon_2 \\ \gamma_{12} \end{bmatrix} \quad (5.14)$$

As calculating the stiffness matrix, we must be knowing Young's Moduli ( $e'=22.4$  GPa), Poisson's Ratios ( $v=0.33$ ) and Shear Moduli ( $G= 22.4$  GPa) also the compliance matrix (S) equal to inverse of stiffness matrix(c) so that we can find the:

$$S_{11} = S_{22} = \frac{1}{e'}, \quad S_{12} = S_{21} = \frac{v}{e'}, \quad S_{33} = \frac{1}{G}, \quad \epsilon_1 = \frac{\partial x}{\partial X}, \quad \epsilon_2 = \frac{\partial y}{\partial Y}, \quad \gamma_{12} = \frac{\partial x}{\partial Y} + \frac{\partial y}{\partial X}$$

The figure 5.8 represents three types of loading on the piezoelectric cell, with the dimensions of the cell being 20 meters along the x-axis (length) and 20 meters along the y-axis (width). The loadings consist of shear forces, compressive forces, and tensile forces, each with a magnitude of 1000 kN/m. By incorporating these different loadings into the model, we can gain insights into how the cell will respond to various stress conditions. Analyzing the stress distribution helps us identify areas of the cell that experience high stress concentrations. This information is valuable for optimizing the design and placement of the cells, as it allows us to develop strategies to mitigate stress concentration and ensure the cell's optimal performance.

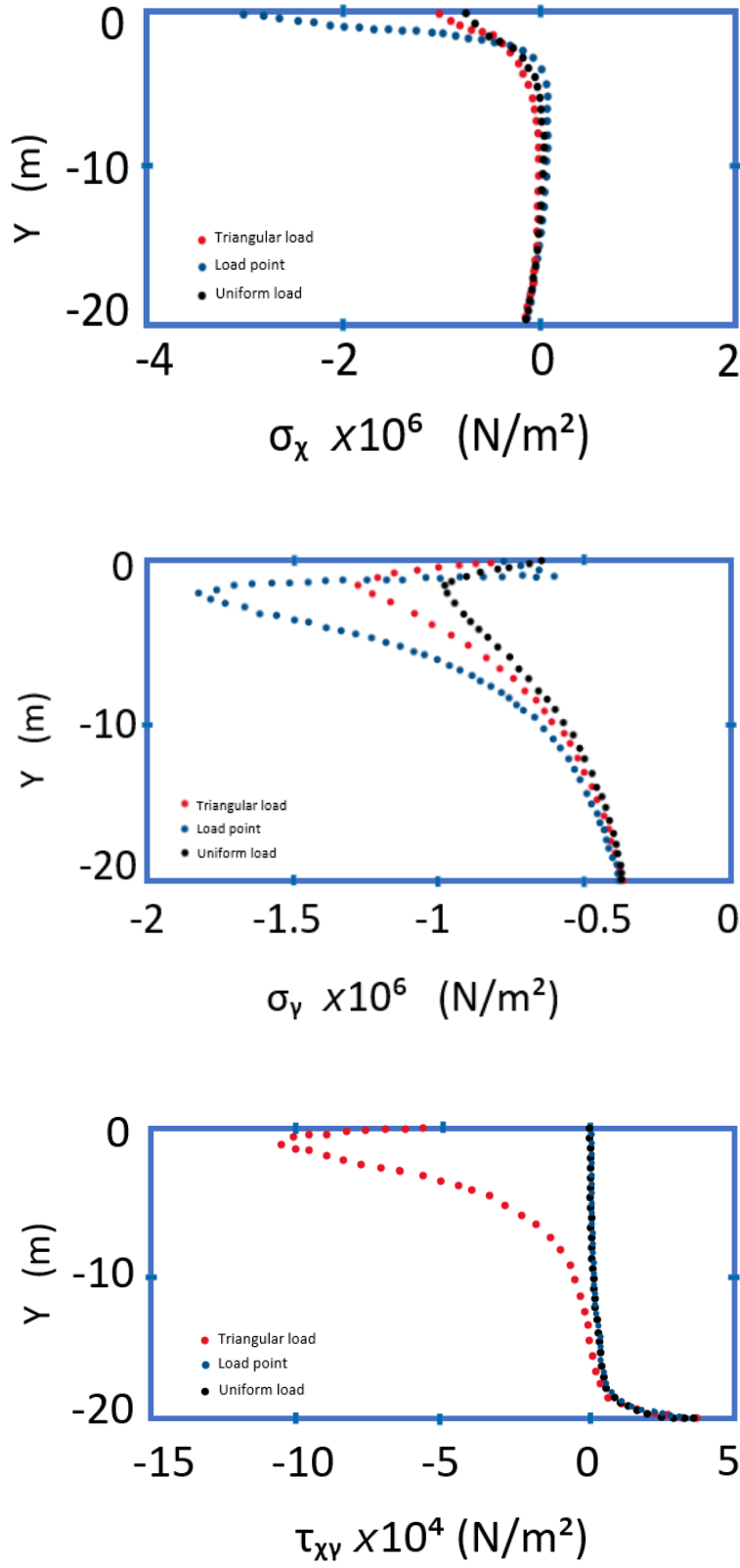


Figure 5. 8 visual representation of the stress distribution  $\sigma_x$ ,  $\sigma_y$ , and  $\tau_{xy}$ , in the piezoelectric cell along A-A section under three loads of point, triangular, and uniform

The results obtained from the stress analysis are significant in the design and analysis of piezoelectric (PZ) materials, as they play a crucial role in ensuring the safety, reliability, and overall performance of these systems. Based on the stress distribution plots presented in Fig.5.8, it can be observed that the maximum stress occurs near the piezoelectric material cell. This localized stress concentration is a result of the deformation and strain that takes place in this region when the material is subjected to mechanical loading.

Under point load conditions, the maximum normal stress ( $\sigma_y$ ) is approximately  $1.78 \times 10^6 \text{ N/m}^2$ , while the minimum normal stress ( $\sigma_y$ ) is around  $0.96 \times 10^6 \text{ N/m}^2$  under uniform distribution load conditions. For normal stress ( $\sigma_x$ ), the maximum stress under point load conditions is found to be  $0.12 \times 10^6 \text{ N/m}^2$ , with the stress distribution under uniform and triangular loads appearing relatively close together. Regarding shear stress ( $\tau_{xy}$ ), the maximum stress is observed under triangular load conditions, with a value of approximately  $10.3 \times 10^4 \text{ N/m}^2$ . The stress distribution under point and uniform load conditions for shear stress ( $\tau_{xy}$ ) appears to be relatively similar. Using the (5.1) open circuit voltage equation with a normal stress of  $1.8 \times 10^6 \text{ N/m}^2$ , the piezoelectric material was found to generate 76.7 Volts. Additionally, by employing the formula (5.3) for induced charge density per surface with the area of the piezoelectric cell ( $40 \text{ m}^2$ ), the charge density was calculated to be 0.34 A. With these current and voltage values, the power output was determined to be 26.078 Watts. The results provide valuable insights into the behavior of piezoelectric cells under different loading conditions and can be used to inform the development of new materials and technologies for road surfaces that can better withstand the stress and shear exerted by heavy vehicles. Also, as indicated by equation (5.5), which demonstrates a direct relationship between the contact area and the charge density (CD), the Figure 5.9, illustrated when increase the contact area the density of charge increase.

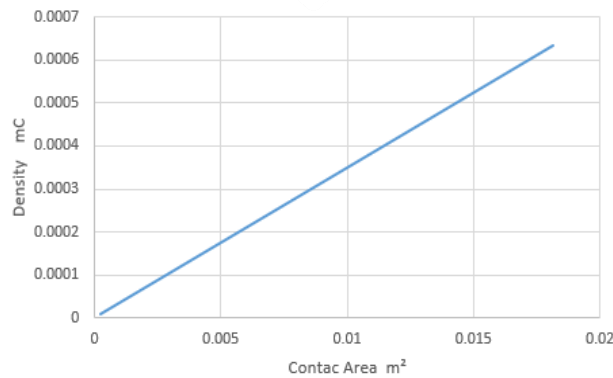


Figure 5.9 the relationship between the charge density and contact area

### 5.3.2 Second case

In this design it is possible to use two mechanisms simultaneously as:

- 1). By using the magnetostrictive effect of Fe-Si-B-C, stray magnetic fields (H) can stimulate longitudinal strain through the magnetoelectric effect then give electricity (magnetoelastoelectric) [35].
- 2). By piezoelectric effect causes strain through mechanical vibrations and generate electricity.

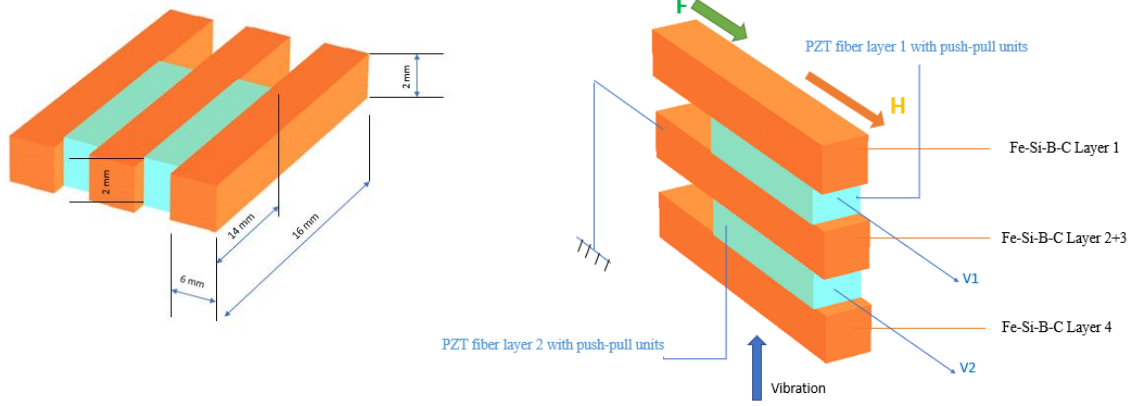


Figure 5.10 Schematic Illustration of energy harvesting for second case

When the magnetostrictive and piezoelectric responses are combined, they synergistically generate electricity through combined strains. This unique interaction allows for the possibility of an additive effect due to the elastic interactions that take place during the conversion process. By leveraging the complementary nature of these two phenomena, the composite strain-induced electrical generation becomes more efficient and effective.

In the case of applying a magnetic field ( $H_{ac}$ ) and a force ( $F$ ) of a specific frequency to the laminate in synchrony, it leads to the generation of vibrations in both longitudinal and bending modes. Consequently, these vibrations induce a voltage across the dielectric layer. The calculation of the induced voltage can be performed using the following formula [61] [62] [63].

$$U^{ind} = -\varphi_e \left( \frac{Z_c}{Z_m} \right) (F + \varphi_m H) \quad (5.15)$$

The equation (5.15) can write as follows:

$$U^{ind} = -\varphi_e \left( \frac{Z_c}{Z_m} \right) F - \left( \frac{Z_c}{Z_m} \right) \varphi_e \varphi_m H \quad (5.16)$$

A negative (-) sign indicates a reverse phase relationship between the applied force or magnetic field and the induced voltage. This signifies that the induced voltage is out of phase with the applied force or magnetic field.

The induced voltage can be attributed to two distinct contributions.

1. F-induced voltage: as a result of a mechanical-to-electric conversion ( $\varphi_e$ ).
2. H-induced voltage: as a result of a magnetoelastoelectric conversion ( $\varphi_e \cdot \varphi_m$ ).

The equation (5.16) refers that the ( $F$  or  $H$ ) induced voltage comparing the capacitance impedance ( $Z_c$ ) of a piezoelectric layer with the mechanical impedance ( $Z_m$ ) of the layer the entire magnetoelectric (ME) laminates. An appropriate mechanical impedance should be adjusted in a laminate in order to achieve effective stress transfer to the vibration source. Therefore, high coupling factors, a low damped capacitance, that is a high piezoelectric voltage coefficient, and a high coupling between the laminate and the vibration source are the variables that can result in large induced voltages.



To generate an alternative magnetic field ( $H_{ac}$ ) as depicted in Figures (5.11) and (5.12), Helmholtz coils powered by a function generator were employed in conjunction with Fe-Si-B-C ribbons. The Helmholtz coils, when energized by the function generator, produce a controlled and oscillating magnetic field. By carefully configuring the Helmholtz coils and supplying them with the appropriate electrical signals from the function generator, an alternating magnetic field is generated. The Fe-Si-B-C ribbons, which are part of the experimental setup, interact with this magnetic field, leading to the desired magnetic response.

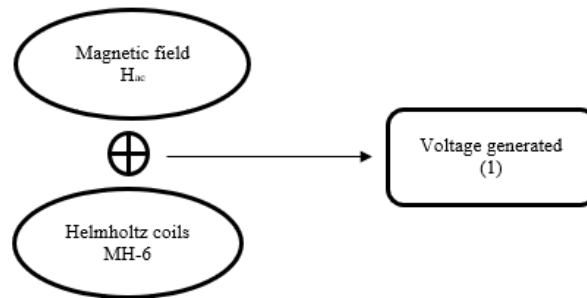


Figure 5.11 Schematic diagram of the first voltage generation

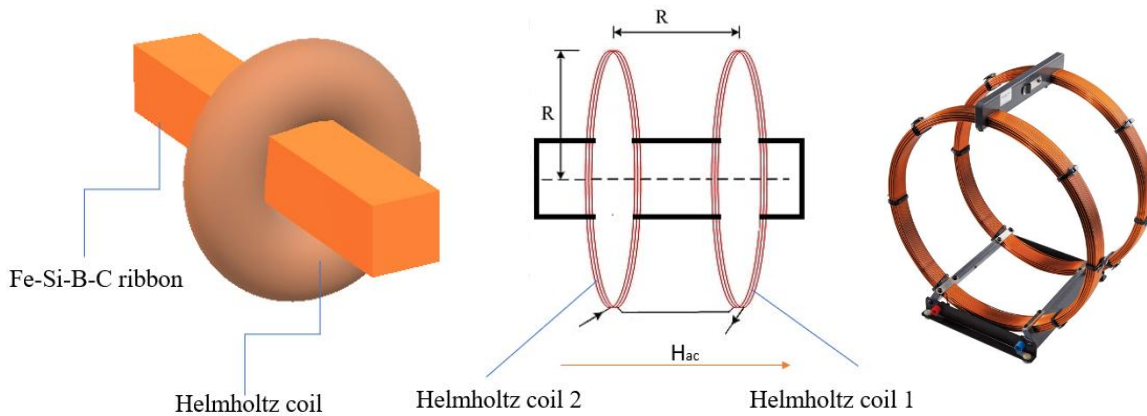


Figure 5.12 Illustration of first generation

The relationship between induced voltage ( $V$ ) and power ( $P$ ) resulting from an applied magnetic field ( $H$ ). The power output ( $P$ ) can be calculated by the formula:

$$P = V^2/R' \quad (5.17)$$

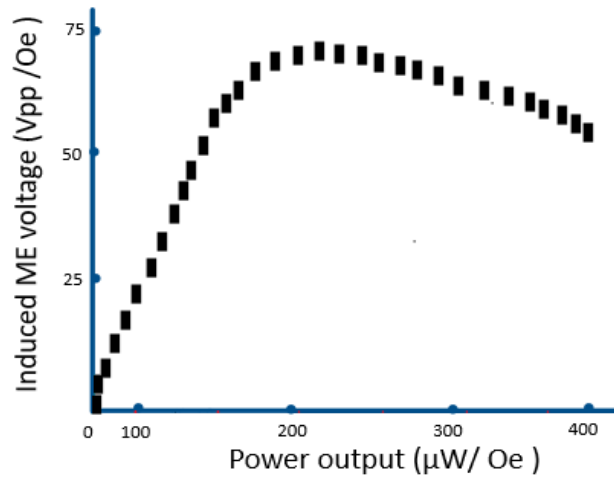


Figure 5.13 Relation between power and voltage for First generation

where  $R'$  represents the electrical resistance. The graph (5.13) shows how the induced voltage ( $V$ ) and power ( $P$ ) vary with the applied magnetic field ( $H$ ). As the magnetic field strength increases, it influences the induced voltage and subsequently impacts the power generated within the system.

During the vibration testing, shakers equipped with wheels were utilized to apply mechanical excitation to the magnetoelectric (ME) laminates. The response of the laminates to the mechanical vibrations was monitored using a PCB Piezotronics Accelerometer with the model number U352C22/meter 482A16. This accelerometer is specifically designed to measure and record vibrations accurately. The principle of piezoelectricity comes into play during the testing. Mechanical vibrations imposed on the ME laminates result in the generation of a voltage. This voltage is a direct consequence of the piezoelectric effect, where the mechanical deformation of the laminates induces an electric charge separation, leading to the production of an electrical potential. Figure 5.14, displays the voltage measurements captured during the testing, specifically for  $V_1$  (first layer) and  $V_2$  (second layer). To facilitate the testing setup, the free end of the cantilever was attached to a 1-gram mass positioned on top of the shaker equipped with wheels. This configuration ensures controlled and precise mechanical excitation of the ME laminates, allowing for accurate measurements of the induced voltages in the respective layers. The use of shakers with wheels, in combination with the PCB Piezotronics Accelerometer, enables controlled vibration testing of the ME laminates. The resulting voltage measurements captured in Figure 5.14 provide valuable insights into the piezoelectric response and behavior of the laminates under mechanical excitation.

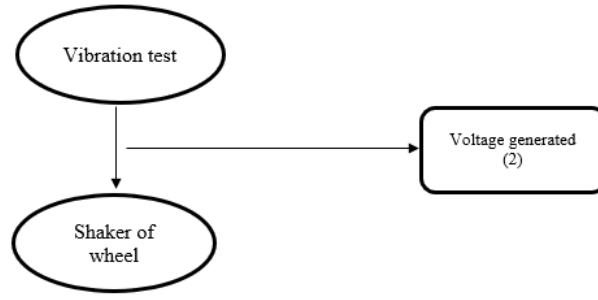


Figure 5.14 Schematic diagram of the second voltage generation

Graph (5.15) shows the relationship between Induced Voltage generate per first layer  $V_1$  and second layer  $V_2$  and power.

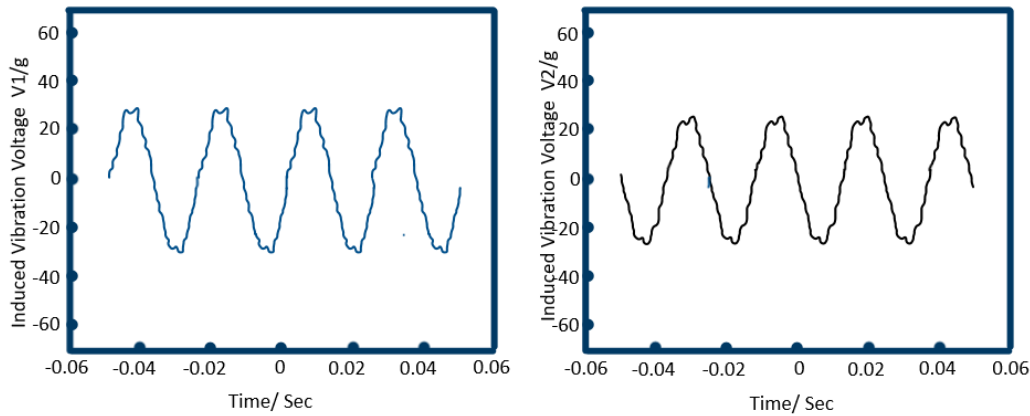


Figure 5.15 Induced voltage generate per first layer  $V_1$  and second layer  $V_2$

#### 5.4 The results of piezoelectric harvesting energy

In the first case design of the system, a notable amount of energy can be stored during a second of driving. This energy generation reaches a maximum of approximately  $10 \mu\text{W}$  when the system is subjected to a maximum load of  $615.07 \text{ kg}$  inside the automotive. Additionally, the system can generate around  $600 \mu\text{W}$  of power over the course of one minute and contact area  $0.01716 \text{ m}^2$ . These energy levels demonstrate the system's capability to adequately meet the power supply demands of various electronic circuits within the vehicle. It is worth emphasizing the significance of the contact area between components, particularly the touch between the cell and the contact surface. The power output of the system is directly influenced by the relationship between the contact area and the density of the cell. As the contact area increases, the density of the cell also increases, resulting in a corresponding increase in power output. Conversely, a decrease in the contact area leads to a reduction in cell density and subsequently, a decrease in power output. However, there is possibility for improvement through meticulous design iterations and experimentation, which can yield even better outcomes. Although the efficiency of such systems typically falls within the range of 30-40%, the utilization of higher-quality PZT-5J materials holds the potential for achieving superior results. By employing these improved materials, the amount of energy that can be generated and stored can be further enhanced. The energy produced by the system holds substantial value and can be utilized in several ways. For instance, it can be harnessed to charge mobile phones, offering a convenient and portable power source while on the move. Additionally, the energy can be stored and

utilized for powering LED headlights, which consume significantly less power compared to traditional headlights. This enables energy conservation and extends the operational lifespan of the vehicle's power supply.

For the second case the following table summarizes the results:

System	Voltage	Power
First system	$\sim 64 \text{ Vp.p./Oe}$	$422 \text{ } \mu\text{W/Oe}$ for $49 \text{ K}\Omega$ load
Second system (V1+V2)	$\sim 60 \text{ Vp.p./g}$	$404 \text{ } \mu\text{W/g}$ across $3.2 \text{ M}\Omega$

In our specific case, two external inputs were applied to the laminates at the same frequency. This simultaneous application of magnetic field and mechanical vibrations resulted in an amplification effect, doubling the generated electric charge within the composites. This phenomenon occurs as a response to the bending stress experienced by the laminates. At resonance frequencies of 20 kHz, 1/Oe (One Oersted is defined as the magnetic field strength), and 1/g, the voltages observed in the first and second systems were approximately 124 V. Additionally, the power generated by the systems was measured to be around  $826 \text{ } \mu\text{W}$ . These results indicate that both the magnetic field and mechanical vibrations have a significant impact on the behavior of the laminates. The observed voltages and power levels highlight the strong interplay between magnetic and mechanical stimuli in the laminates. By harnessing both of these inputs simultaneously, the generation of electric charge can be significantly enhanced, leading to increased voltage output and power generation.

## 5.5 Conclusion

In summary, the findings of the first and second case designs highlight the potential of these systems in energy generation and storage. With further optimization and exploration, they can lead to enhanced power supply solutions in automotive applications. The first case design demonstrates the capability to generate approximately  $600 \text{ } \mu\text{W}$  of power per minute if the stress determines  $0.71 \times 10^6 \text{ N/m}^2$  and  $0.01716 \text{ m}^2$  while with the area of the piezoelectric cell  $40 \text{ m}^2$  and the charge density was calculated to be  $0.34 \text{ A}$ , the power output was determined to be  $26.078 \text{ W}$ . The second case design achieves around  $826 \text{ } \mu\text{W}$ . These power levels are significant and can meet the power supply demands of various electronic circuits within a vehicle. Both case designs emphasize the importance of considering the contact area and the interplay between magnetic fields and mechanical vibrations in maximizing energy generation efficiency. Optimizing the contact area between components, particularly the cell and the contact surface, is crucial for maximizing power output. Additionally, the simultaneous application of magnetic fields and mechanical vibrations in the second case design amplifies the generated electric charge, leading to increased voltage output and power generation. Overall, these findings describe multimodal systems that can simultaneously harvest energy by leveraging piezoelectric devices. Further optimization, material improvements, and exploring the interplay between different stimuli can unlock even greater potential for these systems in automotive applications and beyond.

# Chapter 6

## 6. Roads (infrastructure) effects for other harvesting energy

### 6.1 Introduction:

Increased technological innovation is driving us towards a more sustainable and environmentally friendly Earth. As our dependence on fossil fuels increases, it becomes necessary great if we discover new energy sources that can restore our planet's geochemical balance and compensate for the depletion of fossil fuels. Electric vehicles (EVs) seem to be a promising option for the future, which can overcome the above-mentioned challenges and risks. However, it is important to consider whether EVs alone can adequately meet these challenges. Figure 6.1, provides a comprehensive statistical analysis of the electric vehicle markets sales in different regions or countries as of International Energy Agency (IEA) classification by the first quarter of 2024[42].

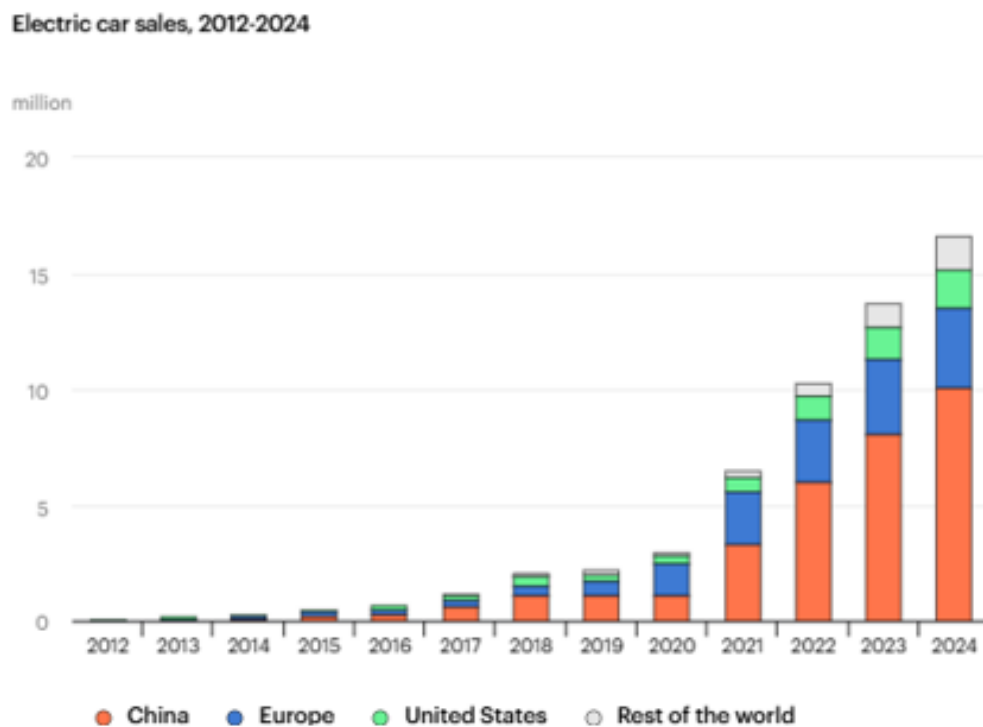


Figure 6. 1 A comprehensive statistical analysis of the electric vehicle markets as of IEA classification

The successful development and widespread adoption of electric vehicles in any country necessitate the establishment of a robust charging infrastructure. This infrastructure plays a pivotal role in supporting the growth and accessibility of EVs. To assess the progress of light-duty plug-in electric vehicle markets worldwide, it is essential to analyze relevant statistics as example the limited availability of electric charging stations in India has had an indirect impact on the number of electric vehicles (EVs) in the country.

In this context, it will be important for original equipment manufacturers (OEMs) to build charging stations before releasing their EV models. The availability of charging stations is a key factor that affects consumer confidence and encourages them to invest in electric vehicles. If charging points are weak and inconvenient, potential EV buyers are more likely to consider switching. By prioritizing charging infrastructure development, it creates a virtuous cycle that supports the growth of the EV market. As more charging stations become available, OEMs gain confidence in bringing their electric devices to market, increasing the choice of EVs for consumers. This helps increase the demand for electric vehicles and forces money encouraging further charge management.

In order to address issues related to charging time and the availability of charging stations, it is essential to devise a strategic approach. One effective strategy is to establish harvesting charging stations (HCS) in various convenient locations such as supermarkets, malls, parking lots, cinemas, and any other areas with existing electric poles. By leveraging existing infrastructure, the deployment of charging stations can be expedited. It is recommended that fast DC chargers be installed within the city limits by using pre-installed electrical poles for faster charging. This makes it more efficient for electric vehicles, reducing transmission time over the entire charge. For easy charging, the voltage from the power pole should be around 230-240 volts.

Charging systems can be easily expanded using existing electric pole systems by properly locating charging stations in easily accessible areas. Not only does this approach provide convenient and convenient charging points for electric vehicles owners but encourages greater use of EV across the region.

## 6.2 Algorithm of harvesting charging station:

Harvesting charging station is represented as shown in the following

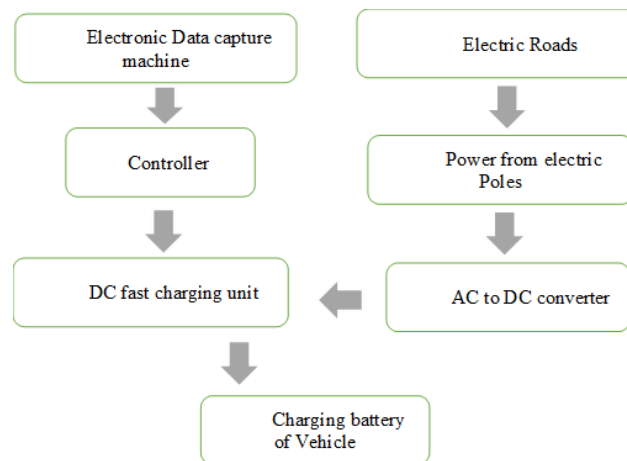


Figure 6. 2 The flowchart of Harvesting Charging Station (HCS)

The central element highlighted in the algorithm is electric roads, which plays a pivotal role in our Harvesting Charging Station. Electric roads enable the generation of electricity through various methods of energy harvesting from rotating vehicle tires. This energy harvesting can be achieved using nanogenerators based on the piezoelectric and triboelectric effects, or

through electromechanical wideband energy harvesters. By harnessing the energy generated by vehicle tires, a previously untapped energy source is discovered. The potential energy that can be harvested from the power generated by the rotation of vehicle wheels on the earth is estimated to be approximately  $3 \times 10^{11}$  kW. This remarkable potential has been explored in a study conducted by Feng-Chen Li in 2019 [43], which examines renewable energy sources and quantifies the power generated under the wheels of a vehicle traveling at a speed  $V$ . In addition, Jin, X. et al. in 2021 [44] demonstrate the cost-effective and unconventional technique of harnessing magnetic energy using a Triboelectric Nanogenerator (TENG). By utilizing magnetic balls rotating around a core, magnetic energy is harvested from transmission lines. The resulting output power of a single TENG unit is measured at 1.5 KV, 6.67 mW. Furthermore, Wang, Z. et al. in their work [45] propose the installation of an energy-monitoring system on bogie frames to measure electromagnetic energy from the rotor. By leveraging the relative motion between the coils and magnetic field, the device can be easily mounted to the wheelset. The output power under trains traveling at speeds ranging from 420 to 820 rpm is estimated at approximately 1982 W per cubic.

These studies highlight the potential of different energy harvesting techniques, such as piezoelectric, triboelectric, and magnetic, to contribute to the generation of electricity in innovative ways. By incorporating these technologies into our HCS, we can harness these untapped energy sources and make strides towards a more sustainable and efficient transportation infrastructure.

### **6.3 Design and construction of roads harvesting energy**

The design and construction of roads that can harvest energy is an emerging field that aims to integrate energy generation capabilities into the infrastructure itself [46]. This new approach has the potential to contribute to sustainable energy, and a range of benefits such as reducing reliance on traditional energy sources and supporting smart cities. It depending about piezoelectric materials quartz, BaTiO<sub>3</sub>, Lead Zirconium Titanate (PZT) etc. Out of these quartz gives highest electrical output voltage w.r.t the mechanical stress applied but it is economically not feasible due to its high cost. The next is PZT which are readily available at low cost and gives impressive results [47].

Piezoelectric materials will be enclosed in protective packages made from insulating materials to protect them from the impact brought by vehicles and the ambient environment. A long-lasting, insulating engineering plastic is selected to build the package, which can resist the external impacts of vehicles. Additionally, the package must block any fluid or chemical from contaminating the hosting material. Fluids should not come in contact with them as they may cause a short circuit between the positive and negative poles of the material. Also, to transferring the stress applied by vehicles to the piezoelectric material uniformly, the protective package also helps ensure a long life for the material.

In the prototype model design, the purchased piezoelectric disks are evaluated using simple tests. Specifically, the device is made up of a plastic cover, a protective Teflon tube, and an edge clearance for location the piezoelectric as follows in Figure 6.3

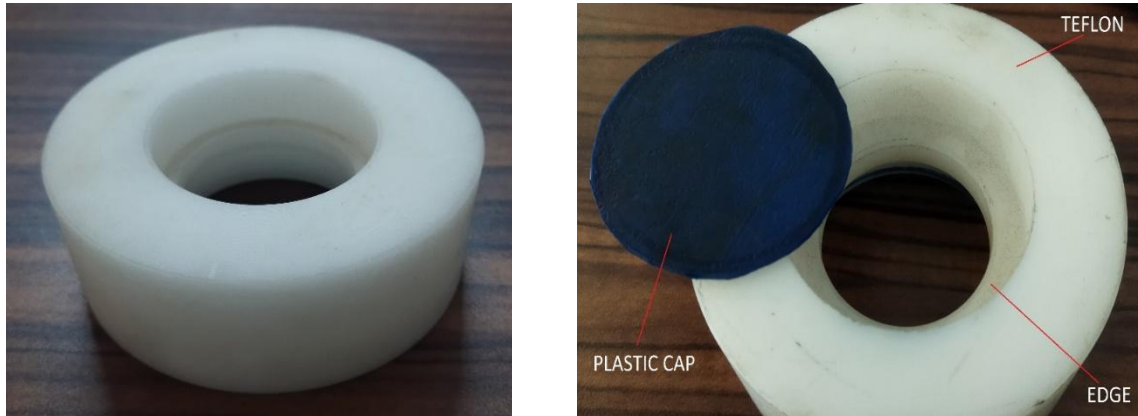


Figure 6. 3 Protective for our study cell of piezoelectric

Here are some key points about the layout Assembly design and construction as following:

### 6.3.1 First design (LAD1)

To accommodate the six piezoceramic disks made of PZT, circular notches will be milled into the aluminum base plate. Here are the specifications:

#### Piezoceramic disks:

Material: PZT (Lead Zirconate Titanate)

Number of Disks: 6

Dimensions: Diameter = 31.5 mm, Thickness = 14.4 mm

#### Base Plate :

Materials : Aluminum

Dimensions : 225 mm x 163 mm x 10 mm

The aluminum base plate has six circular notches milled into it to accommodate the piezoceramic disks. The circular notches will match the dimensions of the disks to ensure a secure fit as shown in Figure 6.4

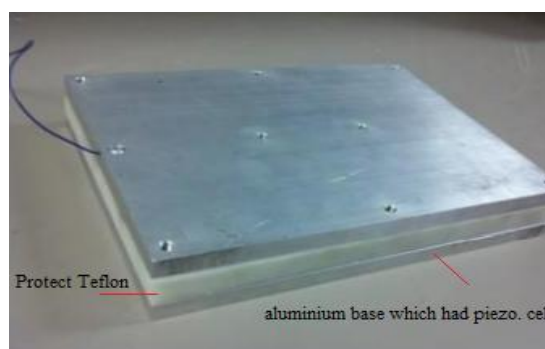






Figure 6. 4 The first layout Assembly design

### 6.3.2 Second design (LAD2)

To accommodate 20 piezoceramic disks made of PZT, the structure will be constructed using cement concrete instead of aluminum alloy covers and bases. Here are the specifications:

#### Piezoceramic disks:

Material: PZT (Lead Zirconate Titanate)

Number of disks: 20

Dimensions: Diameter = 25.2 mm, Thickness = 10.4 mm

#### Concrete structure:

Material: Cement concrete

Dimensions : 225 mm x 163 mm x 10 mm

Design: The structure will be specifically designed to hold the 20 piezoceramic disks securely and provide adequate support. By utilizing cement concrete for the covers and bases, cost savings can be achieved compared to using aluminum alloy. The specific design of the cement concrete structure will ensure proper placement and stability of the 20 piezoceramic disks as in Figure 6.5

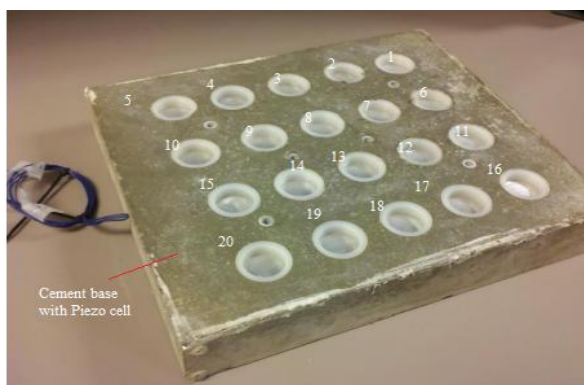


Figure 6. 5 The second layout Assembly design

### 6.3.3 Third design (LAD3)

LAD3 is designed with the same specifications as LAD1 and LAD2, featuring a screw-free packaging to maximize its energy output. The use of screws may result in a loss of strength, so cement-concrete holders are used instead. This method ensures that the force produced by LAD3 has no potential loss of force due to screw tension. The cement concrete holder provides a stable and secure environment for LAD3, preventing any movement or displacement that could affect its performance. By eliminating the need for screws, the risk of loss of strength due to stiffness is eliminated, allowing LAD3 to operate at its optimal capacity. Cement concrete is selected as a material it will carry because of its low cost, durability and ease of installation. Overall, the screw-free packaging with a cement concrete holder enhances the energy output of LAD3, providing a reliable and efficient solution for maximizing power production.



*Figure 6. 6 The third layout Assembly design*

### 6.3.4 Fourth design (LAD4)

LAD4's design includes various adjustments to improve its performance. These improvements include using copper-alloy electrodes, replacing the negative electrodes with copper alloy, and replacing the aluminum material with molybdenum disulphide Nylon (MDS). Here are the details:

#### 1- Copper-alloy electrodes:

Copper-alloy electrodes are connected under the cover of LAD4. Copper alloys are used because of their higher electrical conductivity than other materials. Using copper-alloy electrodes can improve LAD4's electrical efficiency, leading in increased energy production, allows for more efficient charge transfer and lower power losses

#### 2- The cover material is Molybdenum Disulphide Nylon:

The aluminum material in the prior design has been replaced with molybdenum disulphide Nylon. MDS is recognized for its abrasion resistance, high tensile strength, impact resistance, machinability, and elasticity. Furthermore, MDS has the capacity to absorb moisture, which

may improve its effectiveness. This change increases the endurance and lifetime of LAD4, ensuring that it operates efficiently under a variety of situations.

By implementing these changes, LAD4 improves electrical conductivity, energy output, and robustness. These design improvements help to maximize the overall performance and efficiency of LAD4 as an energy-harvesting device.

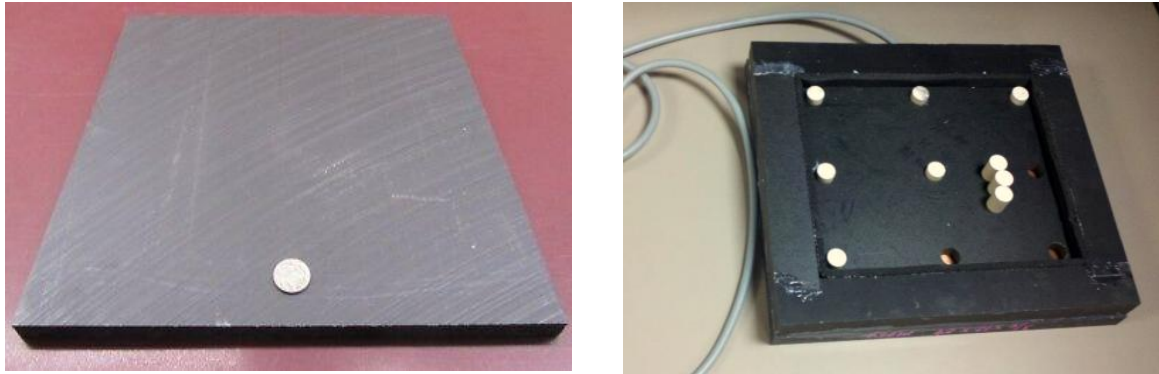


*Figure 6. 7 The fourth layout Assembly design*

### **6.3.5 Fifth design (LAD5)**

LAD5 is a type of energy-harvesting device that combines two types of piezoelectric elements: disks and bars. Similar to LAD4, the components used in LAD5 include copper-alloy electrodes, copper alloy for the negative electrodes, and a molybdenum disulphide Nylon cover material. Here is an overview of LAD5's design.

Here is an overview of LAD5's design:

Piezoelectric disks: LAD5 incorporates piezoelectric disks, similar to LAD4. These disks are made of a piezoelectric material, such as PZT, which can generate electrical energy in response to mechanical stress and pressure.

Piezoelectric bars: In addition to the disks, LAD5 also includes piezoelectric bars. These bars are another type of piezoelectric element that can convert mechanical energy into electrical energy. The bars are typically made of a piezoelectric material and are designed to be responsive to applied forces.

Copper-alloy electrodes: LAD5 features copper-alloy electrodes attached under the cover. The use of copper alloy ensures good electrical conductivity, facilitating efficient charge transfer and maximizing energy output.

Copper alloy for negative electrodes: Similar to LAD4, LAD5 employs copper alloy for the negative electrodes. Copper's superior electrical conductivity allows for improved charge transfer efficiency, reducing power losses and enhancing overall performance.

Molybdenum Disulphide Nylon cover material: LAD5 replaces the aluminum material with molybdenum disulphide Nylon for the cover. This material offers resistance to abrasion, high tensile strength, impact resistance, machinability, and elasticity. Additionally, its moisture absorption capacity can potentially enhance its performance and durability.

#### 6.3.6 Sixth design (LAD6)



*Figure 6. 8 The fifth layout Assembly design*

LAD6 is another design variation of the energy-harvesting device, which follows the same design principles as LAD5 but features a different shape. While LAD5 combines piezoelectric disks and bars, LAD6 incorporates these components in a unique configuration.

LAD6 influence the overall performance and efficiency of the device in harvesting energy from mechanical sources because the contact surface will be increase.

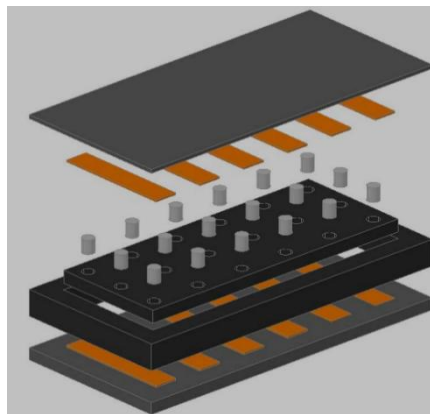


*Figure 6. 9 The sixth layout Assembly design*

### 6.4 Test piezoelectric designs of roads harvesting energy

#### 6.4.1 first design (LAD1) test

Prior to commencing the testing procedure, it is necessary to evaluate the performance of the Teflon-protected disk piezoelectric. For this purpose, we have obtained three specimens from Zibo Yuhai Electronic Ceramic Co., Ltd. These specimens are categorized as single-layer stacks, double-layer stacks, and four-layer stacks. Figure 6.10, illustrates the visual representation of the three types of piezoelectric PZT-51 discs



Figure 6.10 The types of disks piezoelectric which categorized as single, double, and four layers

Below is an illustration depicting the setup of the testing frame. The purpose of this setup is to determine the force applied to the specimen. The specimen is positioned above a force meter and connected to a load resistance. In order to ensure stability and accuracy, a steel stabilizer is placed between the specimen and the force meter, and it is positioned around the electric shaker. To facilitate data collection, the Lab Master software is utilized. This software connects a computer to the various meters in the setup and enables the collection of testing data. During the testing process, different loading resistances are applied to each specimen. The aim is to obtain voltage output data, which reflects the electrical response of the specimens. It is important to note that every 1.2 volts of voltage signal can be converted into 90.4 Newtons of force.

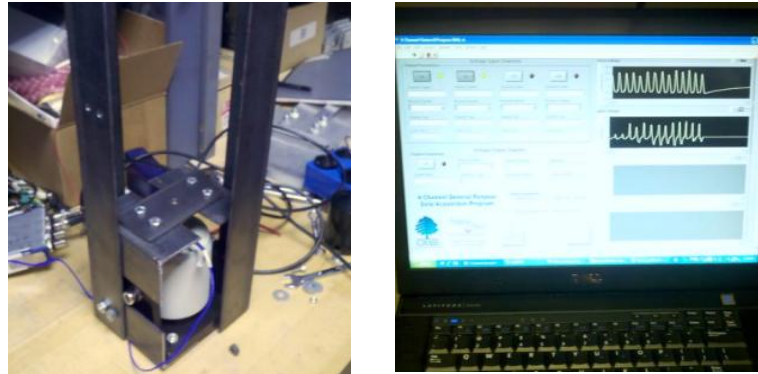


Figure 6.11 The tools testing for LAD1

To calculate the power/force ratio from the output voltage, there is relationship between electrical energy and mechanical work or force and that relationship combines both electrical and mechanical aspects. The equation can be interpreted as:

$$\frac{P}{F} = \frac{\int V^2 dt}{R \cdot \int F dt} \quad (6.1)$$

A piezoceramic disk with a parallel connection generates a different loading resistance when at maximum power output. The single-piece generator should have the highest R of the double generators, while the four-piece generator will have the lowest R. One-piece generators should have the smallest power/force ratio, while four-piece generators will have the best. Graphs of

Power / Force versus Loading Resistance are shown below in Figure 6.12, we found here that when  $R$  equals about  $2250\text{ k}\Omega$  the  $p/f$  will be more than about  $1.14 \times 10^{-9}$  watts/N.

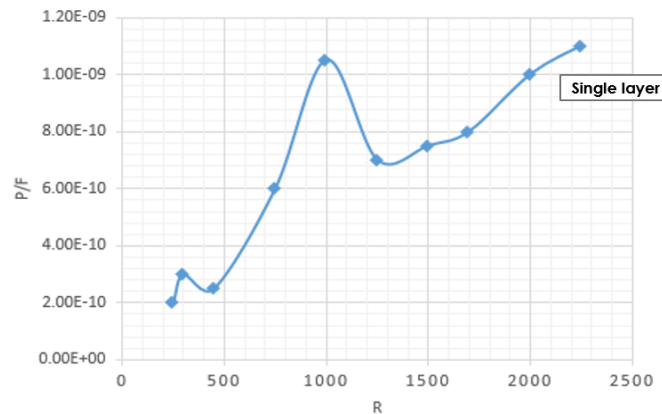


Figure 6. 12 The graph between  $P/f$  &  $R$  for the single-layer generator

With a double layer as Figure 6.13, our results here show that for  $R$  around  $1360\text{ k}\Omega$  the  $p/f$  will be more and equal to about  $2.51 \times 10^{-8}$  watts/N.

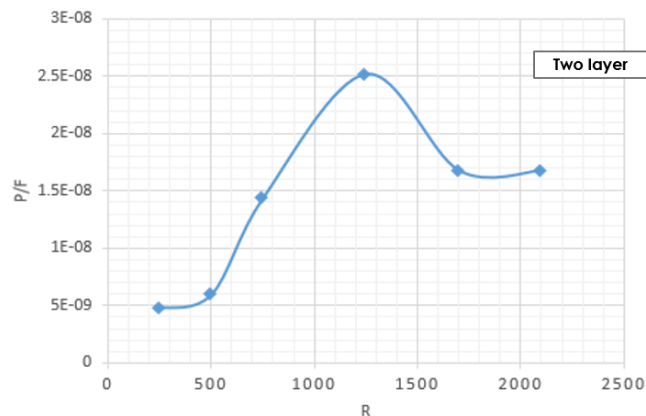


Figure 6. 13 The graph between  $P/f$  &  $R$  for the double-layer generator

According to Figure 6.14, referring to  $R$  as  $1120\text{ k}\Omega$  the power/force is equal to about  $1.01 \times 10^{-7}$  watts/N.

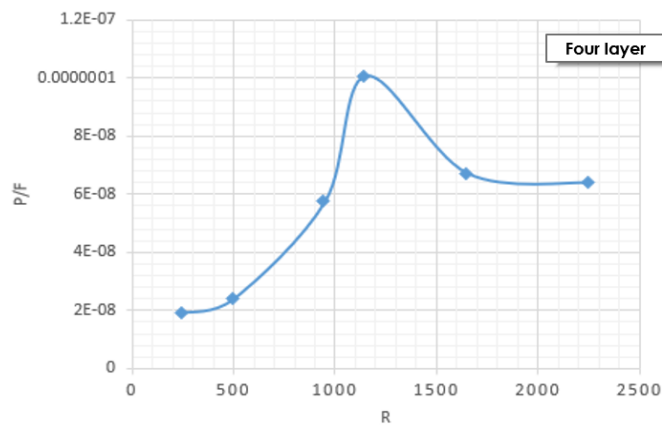


Figure 6. 14 The graph between  $P/f$  &  $R$  for the four-layer generator



Among all the configurations, including single-layer, double-layer, and four-layer schemes, it is evident that the four-piece generators offer the highest level of performance.

In order to evaluate the performance of LAD1, LAD2 and LAD3, it is crucial to consider LAD1 as it provides insights into the energy production or harvesting capabilities. The testing of LAD1 is conducted using a model mobile loading simulator (MMLS) provided by PAVETESTING company with the device Pave®MMLS11 which it rented. This simulator comprises a small wheel that rotates on top of the piezoelectric layer, as depicted in Figure 6.15. The wheel's speed can be varied within the range of 0 to 15 km/hr (0 to 48 Hz). This allows for the simulation of loading conditions similar to those experienced by real pavement under actual traffic.



Figure 6. 15 Model Mobile Loading Simulator

The testing of the LAD1 harvester was performed with varying wheel speeds and resistors, specifically using resistors of 335 k $\Omega$  and 565 k $\Omega$ . As the electrical resistance increases and the speed of testing is raised, the power output of the harvester also increases. It is anticipated that the power output will reach its maximum when the equivalent resistance of the harvester matches the loading electrical resistance.

In the case of the 335 k $\Omega$  resistor, the refer the relationship between the power and frequency reach up to 0.00003W of power at 45Hz.

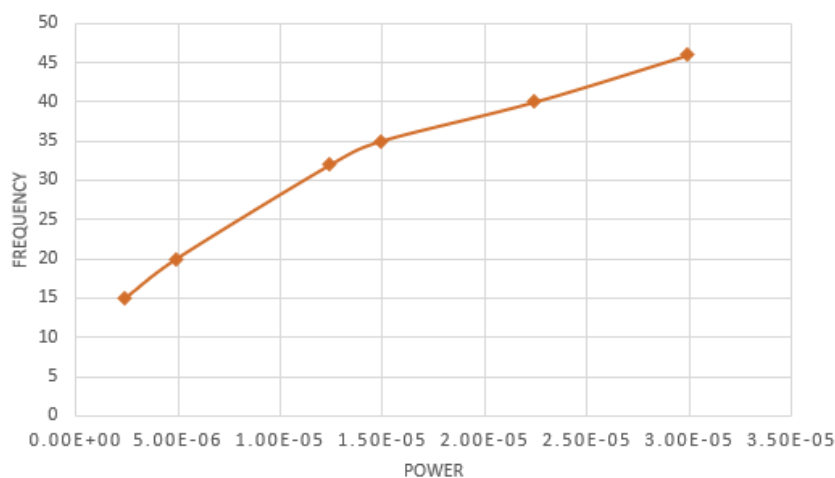


Figure 6. 16 The generating power with frequency when the resistor 335 K $\Omega$

For the case with a 565 k $\Omega$  resistor, the graph depicts the relationship between frequency and power levels up to a maximum of 0.00035W of power at 45Hz.

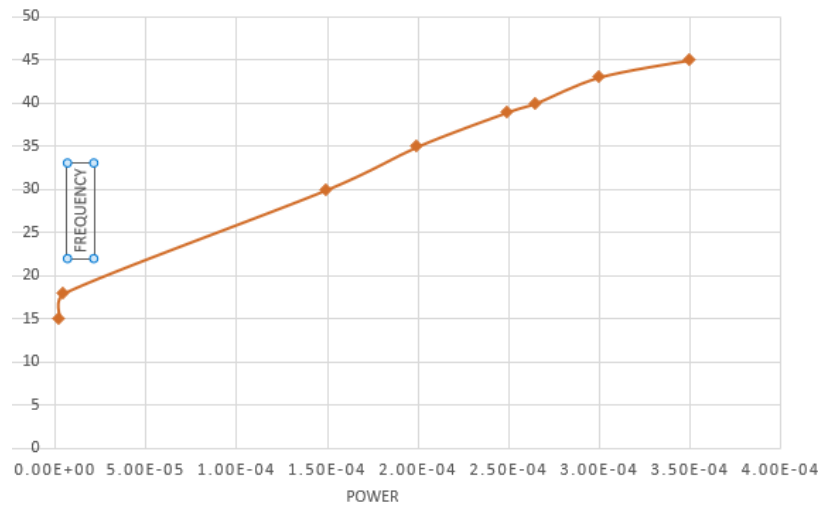


Figure 6. 17 The generating power with frequency when the resistor 565 K $\Omega$

#### 6.4.2 Fourth design (LAD4) test

The LAD4 design is a dedicated layout assembly design for nanogenerators that harness power from the flow of traffic on roadways. It incorporates a protective covering that houses piezoelectric ceramic disks. These disks are responsible for converting the mechanical power generated by the weight of vehicles into electrical power [48]. The performance and efficiency of the LAD4 design were evaluated through testing, and the results were found to be satisfactory in terms of converting mechanical power into electrical power.

The design of The LAD4 can be observed and the base of the design is present in figure 6.18. Copper-alloy electrodes will be attached to a cement structure. For this purpose, the chosen material lies underneath the cover. This material has been chosen for the negative electrodes in place of aluminum alloy due to its superior electrical conductivity.

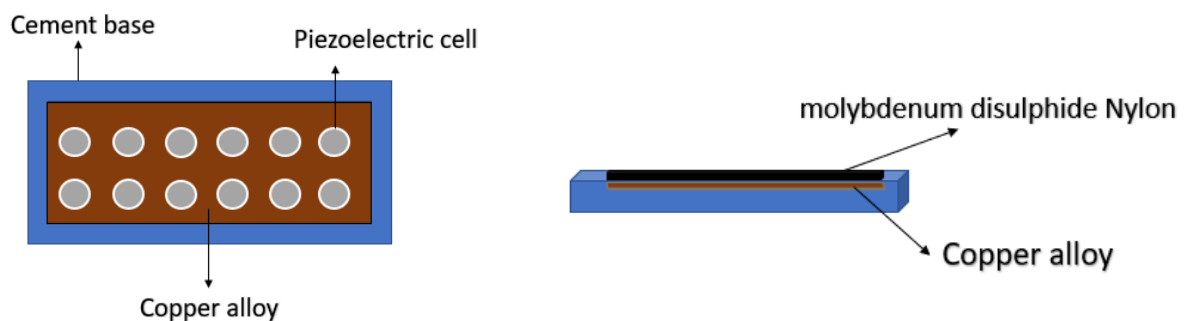


Figure 6. 18 The Illustration of the fourth design

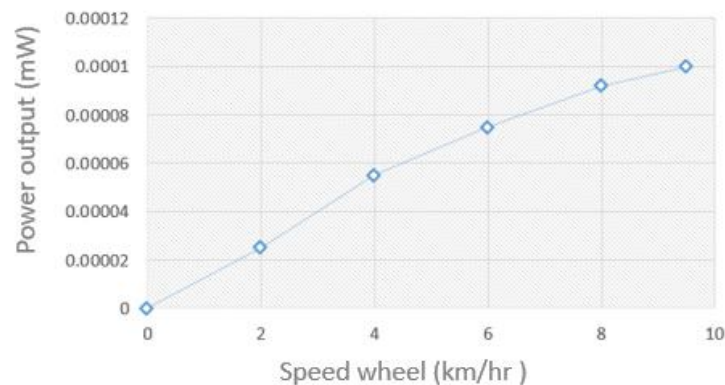
The testing LAD4 procedure for the piezoelectric cells in the LAD1 design follows a similar approach MMLS, utilizing the same type of PZT-51 discs. With reference to equation 6.1, we can summarize the observations for LAD4 and LAD5 as follows:



### For power:

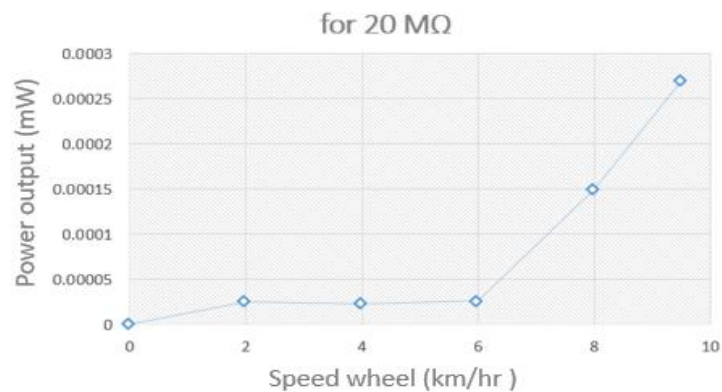
The tests assess speed and loading resistance are an important aspect of evaluating piezoelectric materials for energy harvesting. It is critical to determine the best speed range for energy collecting and evaluate the material's effectiveness at various speeds. When evaluating the piezoelectric material, we conducted trials at speeds ranging from 0 to 10 km/hr to determine the best results. Several loading resistances were evaluated, including 10 M $\Omega$ , 20 M $\Omega$ , 40 M $\Omega$ , and 60 M $\Omega$ . The data demonstrating the link between wheel speed and power production are shown in the diagrams below.

For 10 M $\Omega$ :



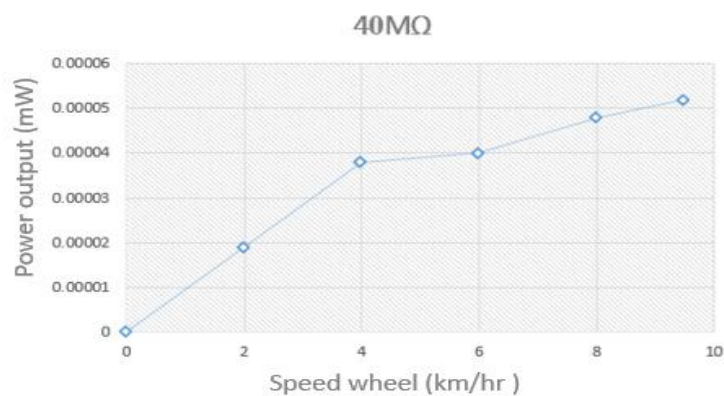
*a*

For 20 M $\Omega$ :



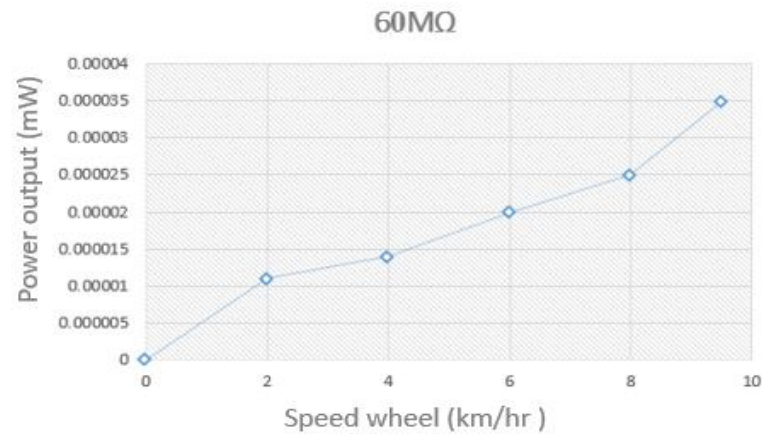
*b*

For 40 M $\Omega$ :



*c*

For 60 M $\Omega$ :



*d*

Figure 6. 19 The relation between power and speed wheel with different loading resistance

(a.10, b.20, c.40, d.60) M $\Omega$

Multiple observations can be extracted from the previous illustrations:

1. Power amplifies along with wheel velocity. This is demonstrated by the fact that at a speed of 9.5 km/hr, a resistance of 20 M $\Omega$  produced nearly identical power to 0.275 mW.
2. It's quite evident that power diminishes when faced with resistance; hence, at 60 M $\Omega$  resistance, power drops to 0.035 m watts.
3. The analysis of the power output trends across the different resistance cases highlights the importance of identifying optimal operational conditions for effective energy harvesting. The diminishing returns at higher speeds suggest a need for careful consideration in system design and energy management as the larger drop in power output between cases (b) and (c) indicates that there is an optimal speed range where energy harvesting is most effective, and the smaller increase in power output from (c) to (d) suggests diminishing returns at higher speeds so that these findings can inform energy management strategies

For voltage:

Its generation from a harvester relies upon several factors such as wheel celerity and load resistance. In the case of Electric Road Energy Harvesting (EREHV) as EREHV1, EREHV2, and EREHV3, voltages generated at a wheel speed of 9.5 km/hr were examined under a 20 M $\Omega$  resistor [49]. It is important to note that altering either the wheel speed or the resistance will impact the voltage production of the harvesting device. For instance, if wheel speed is increased, then voltage output will increase, provided that the resistance remains steady. Similarly, if resistance is raised, harvesting device's voltage production decreases provided wheel speed is kept constant. Additionally, design layout of harvesters may also influence voltage outputs. Distinct harvester's models could have different layouts thus influencing overall voltage generation capacity [50]. Divergences in the output of voltage can occur within similar resistance and wheel speed conditions, across different harvester models. The

noteworthy spikes in voltage every four seconds, as well as numerous crests found in each waveform, imply a sense of recurring pattern or rhythm inherent to this system. Such periodicity could be linked to specific aspects such as wheel rotations or possibly other design elements pertaining to the harvester. Noteworthy correlation between negative values of voltage with wheel disengagement from EREHV1; whereas positive voltages relate to loaded wheel configurations. It indicates that changes in load weight borne by wheels can influence voltage output levels. This comes as no surprise since weight loading on wheels significantly affects energy harvesting potential within the system [51]. Take reference from Figure 6.20 for EREHV1 related voltage data.

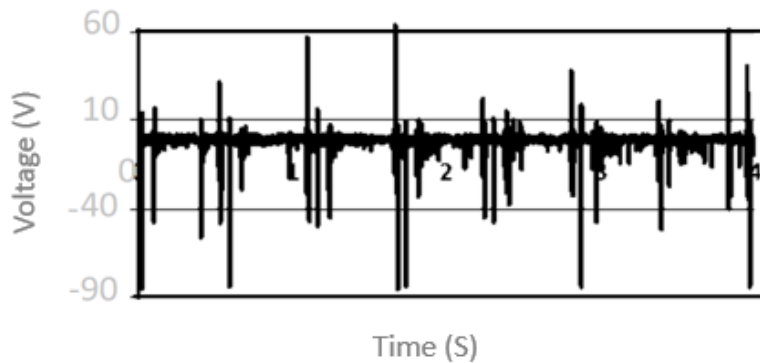


Figure 6. 20 The graph of voltage for EREHV1 at 3.2Km/h

For EREHV2:

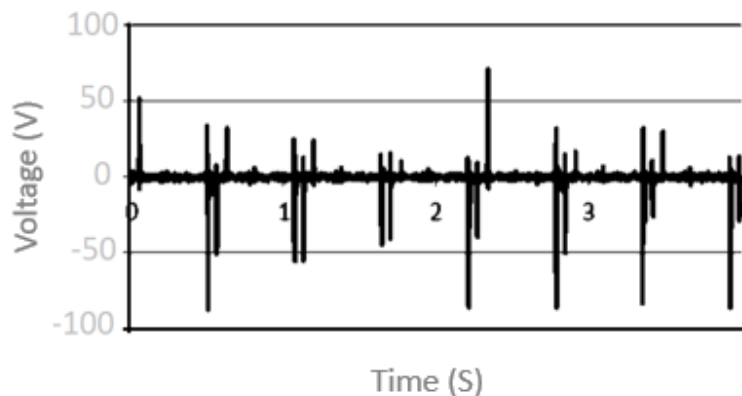


Figure 6. 21 The graph of voltage for EREHV2 at 3.2Km/h

For EREHV3:

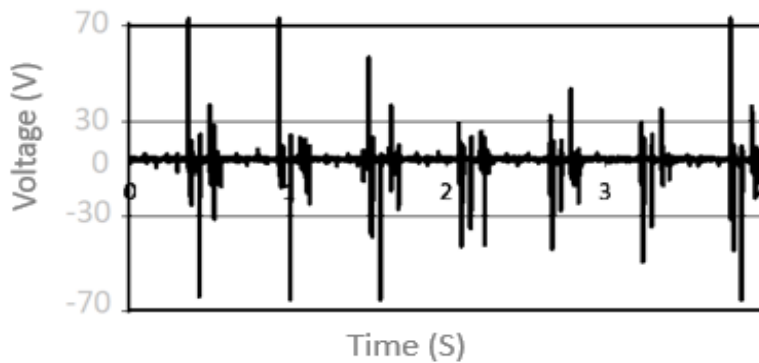


Figure 6. 22 The graph of voltage for EREHV3 at 3.2Km/h

It can be assumed that the increase in voltage parallels the power output of the energy harvester, as shown by preceding graphs. To verify this hypothesis, we constructed and tested various piezoelectric energy harvesters within controlled lab conditions. Piezoelectric substances elicit a voltage response to mechanical strain or change in form. The resultant voltage produced is directly linked to the magnitude of mechanical energy inputted into these materials. Consequently, with every enhancement of energy harvesting efficiency, we should anticipate an accompanying surge in voltage delivery.

## **6.5 Conclusion**

Gaining a comprehensive understanding of the relationship between potential and electrical potential difference is of utmost importance when designing energy harvesting systems that are efficient and effective. By carefully scrutinizing and optimizing this correlation, experts can develop utility designs that excel at converting kinetic potential into electrical potential. In the case of LAD1, we observed that a resistance of  $335\text{ K}\Omega$  yielded a power output of approximately  $3 \times 10^{-5}\text{ W}$ . Similarly, with a resistance of  $565\text{ K}\Omega$ , the power output was approximately  $3.5 \times 10^{-4}\text{ W}$ . In the case of LAD4, as the wheel velocity increased to  $9.5\text{ km/hr}$ , a resistance of  $20\text{ M}\Omega$  resulted in nearly identical power output of  $0.275\text{ mW}$ . Enhancing the efficiency of energy conversion is essential for the practical implementation of energy harvesting systems, especially in scenarios where power resources are scarce or access to traditional power sources is challenging. Therefore, continuous research and development efforts are vital in driving advancements in this field, aiming to improve the efficiency, scalability, and reliability of energy harvesting technologies. By pushing the boundaries of energy conversion and exploring novel materials, techniques, and applications, researchers and engineers strive to unlock the full potential of energy harvesting and its ability to provide sustainable power solutions across various domains. The concept of harvesting energy from roads is a promising area in energy harvesting, and ongoing research and development endeavors are crucial for further advancement in this field.

# Chapter 7

## 7. Electromechanical effects by MMR for other harvesting energy

### 7.1 Introduction

The pursuit of environmentally friendly and cost-effective energy solutions has spurred remarkable advancements in the field of energy harvesting. Among various sources of electric energy, electromechanical energy harvesting [52, 53, 54] emerges as the most promising, offering significant electricity generation potential for diverse applications. This research complements and supports the automotive industry by addressing the challenges associated with power generation and utilization. Mechanical motion-based energy harvesting has gained popularity as a viable approach to generate electrical power across various domains. In the context of automobiles, the mechanical motion induced during driving presents an opportunity to tap into this energy source. One such instance is the oscillation of the third pedal, caused by the connection rod between the brake pedal and the throttle pedal. Efficiently harnessing this motion can provide an additional or alternative power source for automotive systems. In this section, we propose an innovative design for a mechanical motion rectifier (MMR) that captures and converts the mechanical motion of the third pedal in vehicles into electrical power. Through simulation and design tools, we assess the feasibility of implementing this system and explore its potential benefits and challenges in automotive applications. Furthermore, we demonstrate that the design and operational parameters of the MMR system significantly impact its efficiency and performance.

The stages of concept development are depicted about Pedal harvesting energy (HPE) in Figure 7.1, which involves harnessing the minor potential (such as in a car with a raised pedal) and primary kinetic energy generated by the driver's foot while pressing the pedal and depending to MMR.

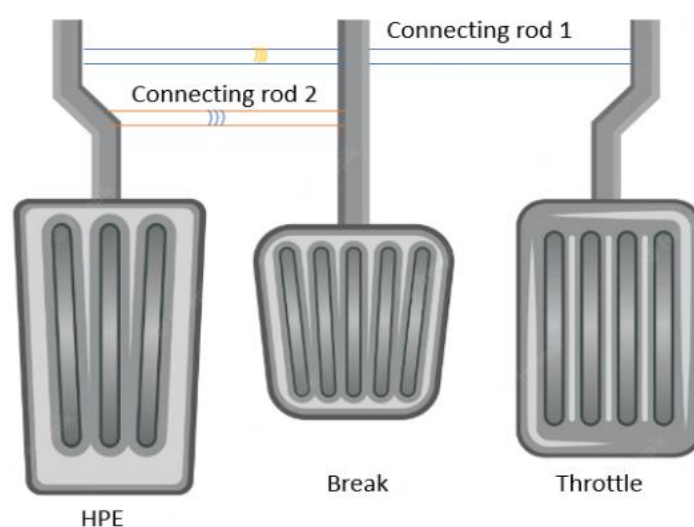


Figure 7. 1 concept development about pedal energy harvesting

So, as notice the pedal energy harvesters are designed to capture the kinetic and potential energy released during the contact between the driver's feet and the pedal. The key components of the pedal energy harvester are illustrated in Figure 7.2

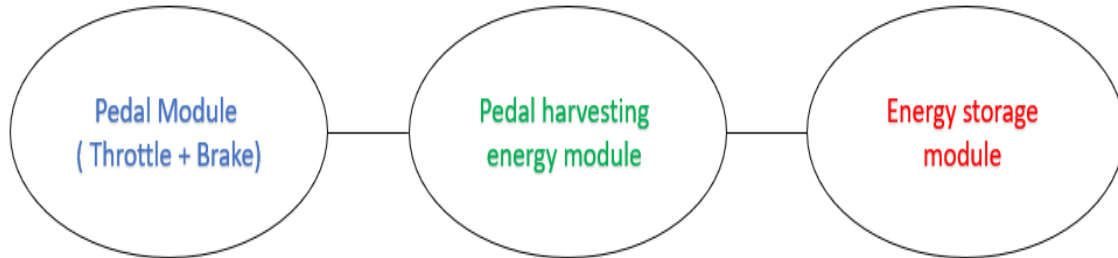


Figure 7. 2 The main components for the harvester pedal energy

## 7.2 Characteristics and features of electromechanically energy

### 7.2.1 Pedal (throttle + break) module

As stated earlier, the throttle and brake pedals are connected to the HPE (harvesting pedal energy) module through a connecting rod.

1. The connecting plate, made of stainless-steel type 440, is chosen for its ability to withstand shocks and effectively carry the load. Its purpose is to transmit the load from the driver to the harvesting module.
2. Springs and bearings: The pedal is equipped with springs attached from the bottom, and linear bearings are connected to shafts, as depicted in Figure 7.3

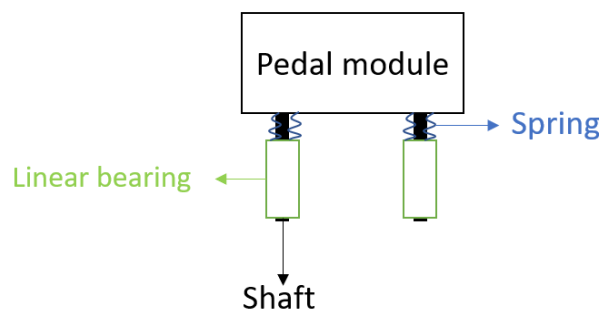


Figure 7. 3 A schematic of the (throttle & brake) module

The selection of the spring is crucial as it directly impacts the performance and load capacity of the energy harvester. To ensure the correct choice of spring, it is important to consider the rebound time, which should be approximately one-quarter of the total oscillation cycle time, corresponding to the natural frequency of the system. This ensures optimal performance and efficiency. Another important factor to consider in spring selection is the time interval between consecutive pedal presses, known as the pedal cadence. This parameter affects the energy storage and release characteristics of the system. The chosen spring must be capable of quickly storing and releasing energy to keep up with the pedal cadence. Additionally, it should provide

sufficient energy storage capacity to meet the overall requirements of the system. By carefully considering these factors, the appropriate spring can be selected to maximize the energy harvesting efficiency and ensure the system meets the desired performance criteria.

### 7.2.2 Pedal harvesting energy module

It contains the following:

1. The pinion gear (1&2) and rack system are responsible for converting linear motion into rotational motion, as depicted in Figure 7.4, The specifications for the system include a length of 340 m, a force of 2F, and specific attributes such as LAM and DDF ranging from 9 to 14. The specification for the toothed wheel is  $Z = 25$  M2 LR=20 IF DF=25 CLLR=8.

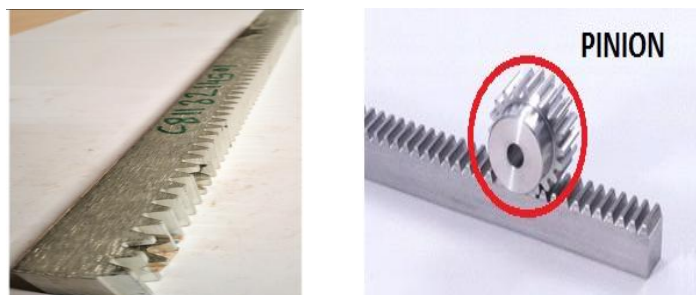


*Figure 7. 4 The Rack & pinion in pedal harvesting energy module*

2. The gearbox of a harvesting unit holds significant importance as it enables the attainment of the rated speed for the motor. This is necessary because the regular speed of the pinion gear is insufficient to drive the motor at its desired speed. In this case, a planetary gearbox provided by Nanotec Company is utilized [55]



*Figure 7. 5 The gearbox in pedal harvesting energy module*

3. The guide and bearing components are integral to the connection between the connecting rod and rack system, facilitated by a bearing pin as depicted in Figure 7.6, two distinct types of bearings are utilized in this system: the linear bearing guide FRN 32EI and the FRNR 32EI, as illustrated in Figure 7.7.

FRNR 32EI allowing for smoother and more consistent movement compared to fixed linear bearings. Also, can provide improved load capacity, lower friction, and enhanced durability.





Figure 7. 6 The guide, FS32TT, L=460mm, 9F, DF9



a



b

Figure 7. 7 The bearing (a. FRN, b. FRNR)

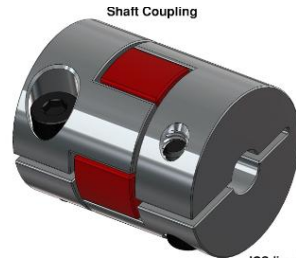
4. The role of shaft supports is to secure and position components employed in linear motion applications. In cases where the weight is relatively light, there is a propensity for the support blocks to exhibit deflection between the supports. Support blocks are commonly employed in applications with low loads to minimize deflection. Specifically, the UCPA206 type of support block was used, as depicted in Figure 7.8



Figure 7. 8 The support UCPA 206 of shaft

5. The coupling [56] is a mechanical device designed to connect two rotating components, such as shafts or gears, while allowing for flexibility to accommodate slight misalignments or movements. This flexibility ensures that the two components remain connected and able to transmit power, even in scenarios where perfect alignment is not achievable or when there is movement or vibration within the system.





*Figure 7. 9 The coupling of the shaft*

### 7.2.3 Energy storage module

The system comprises a generator motor [55], specifically a brushless DC motor. Brushless DC motors do not have brushes, eliminating the occurrence of friction. Consequently, brushless motors exhibit higher efficiency. Moreover, BLDC motors can also function as generators. Therefore, the prototype incorporates a three-phase, single-shaft BLDC motor. Additionally, this model includes an electrical load.



*Figure 7. 10 The brushless DC motor NEMA 17*

By combining these components, the system can effectively capture, convert, and utilize the energy generated by the driver's pedal motion, providing an alternative power source for various applications. The whole system of MMR collects as following:

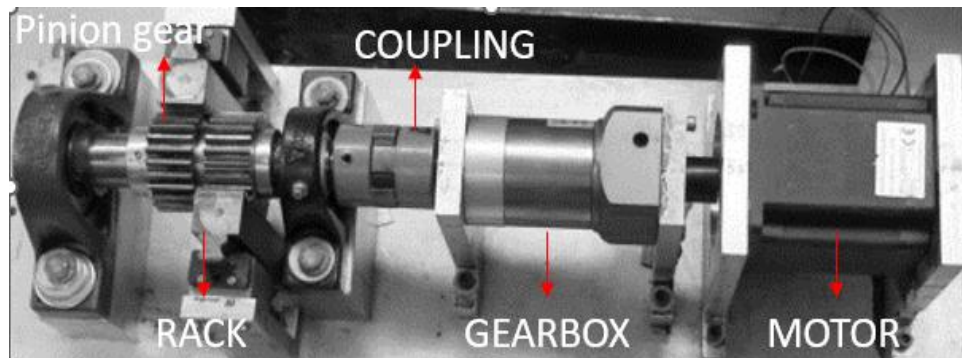


*Figure 7. 11 The mechanical motion transformation of the pedal harvesting energy*

The MMR achieves the conversion of linear motion from racks into rotational motion by interlocking pinion gears 1 and 2. When the driver vertically presses the pedal module, the rack moves, causing the pinion gear to rotate and the shaft to spin. This rotation of the shaft drives the gearbox, which in turn rotates the DC motor, generating electric power. To enhance power generation efficiency, a gearbox is utilized to increase rotational speed, as the linear motion of the rack alone cannot achieve high speeds. The generated energy is stored in a battery and can be used later. The Figure 7.12, shows a schematic of the mechanical motion transformation MMR for the third pedal.

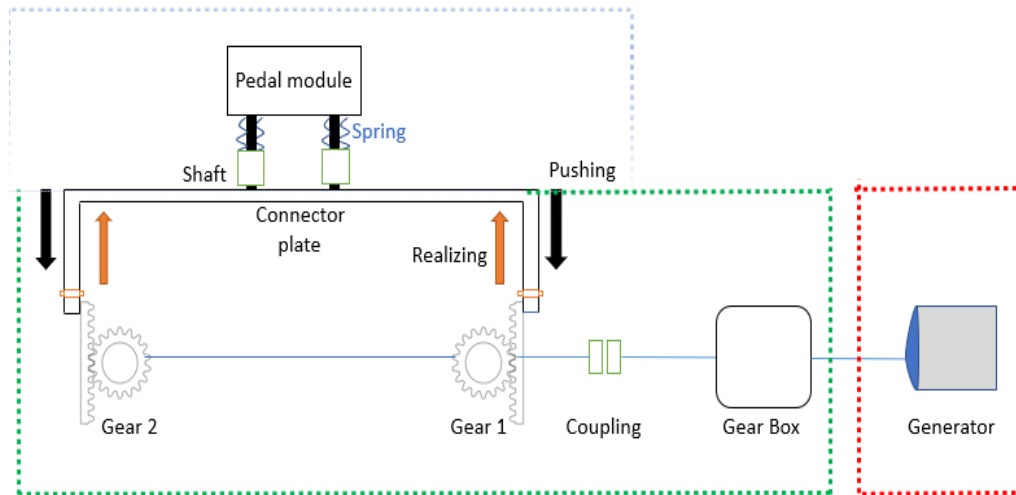


Figure 7. 12 A schematic of the mechanical motion transformation MMR for the third pedal

### 7.3 Statistical analysis of electromechanically energy by MMR

To start statistical modeling, it is better to have an understanding of the various dynamics of the mechanical motion transformer MMR. This is crucial in investigating the feasibility of energy harvesting from the third pedal and demonstrating how we can control and extract power from this strategy.

#### 7.3.1 Pedal harvesting energy dynamics

Pedal energy harvesting is a concept that involves harnessing the mechanical motion of a pedal, such as those found in vehicles or bicycles, to generate and collect energy. In this concept, the pedal acts as a mechanism for converting mechanical force into usable energy. In Figure 7.13 provides a visual representation of the pedal energy harvesting system, emphasizing the applied force on the pedal (referred to as PHE). This force is typically exerted by the user, whether through their foot or another method of interaction. Understanding the transmission and transformation of this force within the system is vital for analyzing the dynamics of pedal energy harvesting.

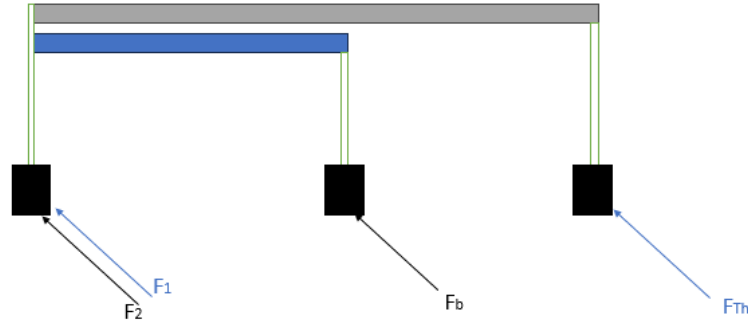


Figure 7. 13 The pressed force acting on the pedal (PHE)

The connection between the PHE (Pedal Harvesting Energy) system and the MMR (Mechanical Motion Transformer) system can be established through the consideration of spring stiffness and equivalent electrical damping as shown in Figure 7.14, spring stiffness  $K_b$  refers to the stiffness or resistance offered by a spring when it is compressed or stretched. In the context of the PHE and MMR system, the spring stiffness can be used to control the interaction between the pedal and the mechanical motion transformer. It determines the amount of force required to compress or stretch the spring, thereby affecting the torque and power transmission within the system. Equivalent electrical damping  $C_b$  refers to the damping effect that can be represented by an electrical circuit equivalent to the mechanical system. It is used to model the dissipation of energy within the system due to factors such as mechanical friction between moving parts such as bearing or joints, air resistance when the air molecules collide with the surface, or viscous damping like moving in air around moving elements which resists motion. By incorporating equivalent electrical damping, the behavior and response of the system can be analyzed and optimized. The spring stiffness and equivalent electrical damping are parameters that can be adjusted and optimized to achieve desired performance characteristics in the PHE and MMR system. They play a role in determining factors such as the system's response time, stability, energy efficiency, and overall performance.

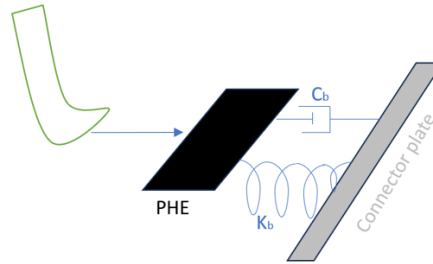


Figure 7. 14 The connection between the PHE and the MMR by  $C_b$ ,  $K_b$

According to Newton's second law of motion, we can express the equation of motion for the Pedal Harvesting Energy (PHE) system as follows:

$$\sum F = M_b \cdot a$$

$$F_{spring} + F_{damping} + F_1 + F_2 = M_b \cdot a$$

$$F_1 + F_2 = M_b \cdot x'' + C_b \cdot x' + k_b \cdot x$$

$$F_t = M_b \cdot \ddot{x} + C_b \cdot \dot{x} + k_b \cdot x \quad (7.1)$$

### 7.3.2 Dynamics equations for rack in MMR

The dynamics equation for the rack can be described based on Newton's second law and Figure 7.15 as follows:

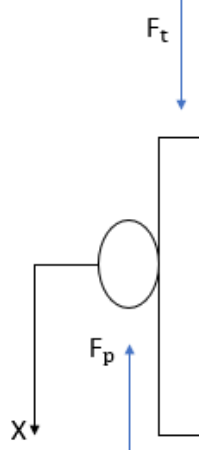


Figure 7. 15 The forces acting on rack of MMR

$$M_r \cdot a = F$$

$$M_r \cdot \ddot{x} = -F_p + F_t \quad (7.2)$$

Also, the force of pinion gear can give as:

$$F_p = \frac{2 \pi T_p}{p' \eta R} = K \frac{T_p}{R} \quad (7.3)$$

$$M_r \cdot \ddot{x} + K \frac{T_p}{R} = F_t \quad (7.4)$$

### 7.3.3 Dynamics equations for pinion and outer ring of one-way clutch in MMR

To find the equation for the above circumstance involving the MMR, it is necessary to sketch the torques and inertia associated with the system. To begin, a sketch of the MMR should be created, clearly identifying the places of the angular displacement and axis of rotation, as shown in Figure 7.16

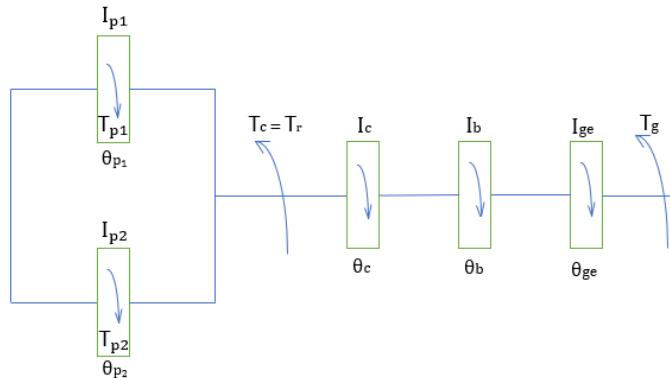


Figure 7. 16 The moment of inertia and torques of MMR

Next, the moment of inertia for the MMR must be considered. The moment of inertia represents the rotational inertia of the system and is influenced by the distribution of masses and their distances from the axis of rotation. The total moment of inertia for the MMR can be obtained by summing the individual moments of inertia for each mass.

$$I = \int r^2 . dm \quad (7.5)$$

The equation for the given situation can be derived by applying Newton's second law for rotational motion. This equation ties the net torque exerted on the system to the moment of inertia and the angular acceleration of the MMR, allowing us to study the rotational dynamics of the pinion as follows.

$$I_{p, n} . \theta''_{p, n} = T_p - T_r \quad (7.6)$$

$n=1,2$  because we have here in this case only two pinion gear.

$T_r = T_c$ : indicates a state of equilibrium where the reaction torque equals the counteracting torque. This balance prevents the ring from rotating despite the presence of external loads or disturbances.

$$I_{p, n} . \theta''_{p, n} = T_p - T_c \quad (7.7)$$

For the ring:

$$I_0 . \theta''_0 = - T_p \quad (7.8)$$

### 7.3.4 Dynamics equations for coupling, gearbox and generator in MMR

According to the moment of inertia and figure 7.16 we can determine each of dynamic equations for.

1- Coupling:

$$I_c . \theta''_c = T_c \quad (7.9)$$

2- Gearbox and generator:

$$I_{ge} . \theta''_{ge} + I_c . \theta''_c = T_c - T_g \quad (7.10)$$

$\theta_c = \theta_b = \theta$  these two components (coupling and gearbox) are linked in such a way that they rotate together.

$$\theta_{ge} = n' \cdot \theta_b$$

So that we can write:

$$\begin{aligned} I_{ge} \cdot n' \cdot \theta''_b + I_c \cdot \theta''_b &= T_c - T_g \\ (I_{ge} \cdot n' + I_c) \theta''_b &= T_c - T_g \end{aligned} \quad (7.11)$$

Electromagnetic induced torque ( $T_g$ ):

This torque produced by the interplay of electric currents and magnetic fields in a spinning electrical machine, such as generator and it gives as:

$$T_g = K_t \cdot B \cdot I \cdot \sin \alpha \quad (7.12)$$

In a simplified design scenario where there is a linear relationship between the torque and current, we can set  $\alpha$  to  $90^\circ$  (indicating that the magnetic field and current are perpendicular) and assuming a linear relationship between torque and current, one can predict that the torque rate (T/B)=1

$$T_g = K_t \cdot I \quad (7.13)$$

From each of equations 7.4,7.7,7.11, we can analysis the equation for harvesting energy as following:

$$\begin{aligned} M_r \cdot x'' + K \frac{T_p}{R} &= F_t \\ M_r \cdot R \cdot \theta'' + K \frac{T_p}{R} &= F_t \\ I_{p,n} \cdot \theta''_{p,n} &= T_p - T_c \\ T_p &= I_{p,n} \cdot \theta''_{p,n} + T_c \\ (I_{ge} \cdot n' + I_c) \theta''_b + T_g &= T_c \\ T_p &= I_{p,n} \cdot \theta'' + (I_{ge} \cdot n' + I_c) \theta'' + T_g \\ T_p &= (I_{p,n} + I_{ge} \cdot n' + I_c) \theta'' + T_g \\ M_r \cdot R \cdot \theta'' + \frac{K}{R} (I_{p,n} + I_{ge} \cdot n' + I_c) \theta'' + \frac{K}{R} \cdot T_g &= F_t \end{aligned}$$

From equation 7.13 we can write:

$$M_r \cdot R \cdot \theta'' + \frac{K}{R} (I_{p,n} + I_{ge} \cdot n' + I_c) \theta'' + \frac{K}{R} \cdot K_t \cdot I = F_t$$

The voltage (V) and current (I) for generator:

The electromotive voltage (EMV) in generator which connected by gearbox express by:

$$EMV = V = K_g \cdot n' \cdot B \cdot A \cdot \omega \quad (7.14)$$

The voltage expresses in another formula: ( $\omega = \theta'$ )

$$V = K_g \cdot n' \cdot \theta' \quad (7.15)$$

Also, the current can write as:

$$I = V/R_t$$

$$I = \frac{K_g \cdot n' \cdot \theta'}{R_t} \quad (7.16)$$

$$M_r \cdot R \cdot \theta'' + \frac{K}{R} (I_{p,n} + I_{ge} \cdot n' + I_c) \theta'' + \frac{K}{R} \cdot K_t \cdot \frac{K_g \cdot n' \cdot \theta'}{R_t} = F_t$$

$$[M_r \cdot R + \frac{K}{R} (I_{p,n} + I_{ge} \cdot n' + I_c)] \theta'' + [\frac{K \cdot K_t \cdot K_g \cdot n'}{R \cdot R_t}] \theta' = F_t$$

$$M_e \cdot \theta'' + C_e \cdot \theta' = F_t$$

$$\theta'' = \frac{1}{M_e} F_t - \frac{C_e}{M_e} \cdot \theta' \quad (7.17)$$

### 7.3.5 State of disengagement equation in MMR

When a system is disengaged, the mechanical linkage between the driving force and the generator shaft is interrupted. As a result, the generator shaft continues to rotate due to its inertia, but this rotational motion gradually diminishes over time. Therefore, the angular displacement of the generator can be instead ( $\theta'_{ge}$ ) as follows:

$$\theta'_{ge} = \theta'_{ge} \cdot e^{-\alpha t} \quad (7.18)$$

$\alpha = C_e/M_e$  it is the decay factor, also known as the angular damping coefficient, controls the rate at which the generator shaft's rotational motion decreases.

t: this is the amount of time that has passed since the system was disconnected. The decay effect causes the angular displacement to decrease with time.

Based on equations (7.1), (7.17) and (7.18), it has been determined that the harvesting of energy can be achieved. The power can be calculated either from the angular velocity ( $\theta'$ ) or from the linear velocity ( $x'$ ) as follows:

$$\begin{aligned}
 P &= T_g \cdot \theta' \\
 &= K_t \cdot I \cdot \theta' \\
 &= K_t \cdot I \cdot x' / R \\
 &= C_e \cdot \theta'^2
 \end{aligned} \tag{7.19}$$

#### 7.4 Modeling and Experiment of MMR:

To evaluate the effectiveness of MMR, an initial study was conducted to harvest energy from this technology. Additionally, to identify the factors that influence this energy harvest, it is necessary to determine the variable factors. From the equation (7.1) we can found the pedal position as:

$$x'' = \frac{1}{M_b} F_t - \frac{C_b}{M_b} x' - \frac{k_b}{M_b} x \tag{7.20}$$

The Simulink for equation (7.20) gives as figure 7.17

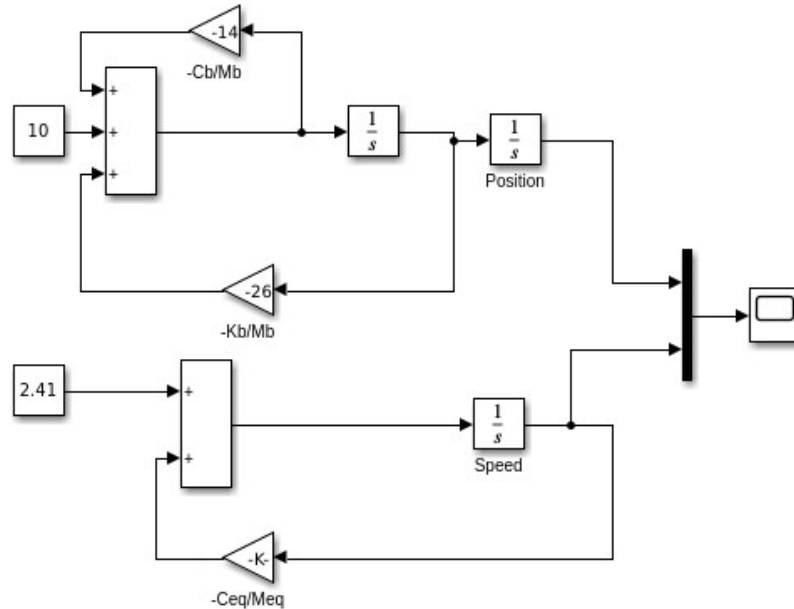


Figure 7. 17 The drawing of Simulink for whole the system



The gain block comes from the tested indicators which we take in following schedule.

Table 3. 1 Information about the tested indicators for simulation MMR

Name	Notation	Value and unit
Equivalent mass	$M_{eq}$	207.25 kg
Pressing mass	$M_b$	50 kg
Equivalent coefficient when $R_t = 202\Omega$	$C_{eq}$	28.65 (N-s/m)
Pinion stiffness	$K$	0.5024 (N/m)
Generator stiffness	$K_t$	0.18 (N/m)
PHE stiffness	$K_b$	1300 (N/m)
PHE coefficient	$C_b$	700 (N-s/m)

Since ( $F_t$ ) is related through ( $M_b$ ) between the brake pedal and the throttle pedal according to equation (7.21).

$$F_t = M_b \cdot g \quad (7.21)$$

Table 3. 2 Information about pressing mass for small and big car

Type	Small or family car	Big car
Brake pedal	(23- 45) kg	(45-68) kg
Throttle pedal	(9-23) kg	(23-45) Kg

In order to evaluate the efficacy of MMR (Mechanical Motion Rectifier), an initial study was undertaken to explore its energy harvesting capabilities. To further comprehend the factors influencing energy harvest, specific values needed to be identified. Figure 7.18 illustrates the examination of signals depicting pedal position and angular speed over a duration of approximately 60 seconds (one minute). The analysis uncovered a linear correlation between the pedal position and time, steadily increasing throughout. Conversely, the angular speed exhibited a gradual rise until reaching a peak of 17.5 rad/s.

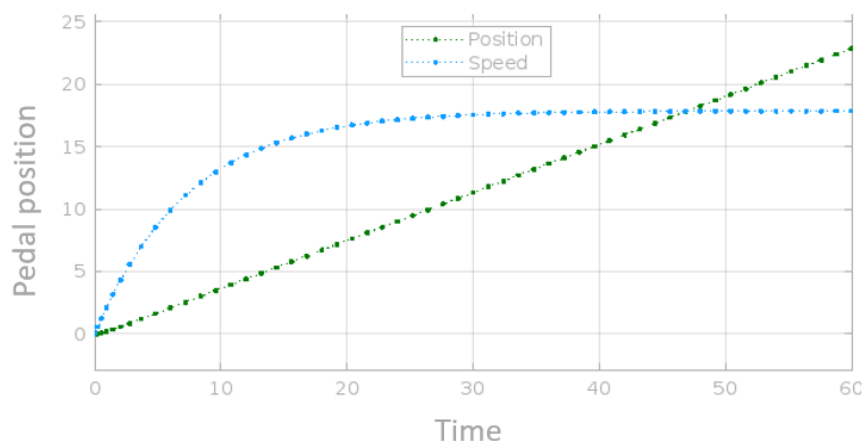


Figure 7. 18 The response system according to time for PHE

Then perform a simulation according to equation (7.18) between the generator shaft in the left figures and the pinion gear in the right figures of (7.19,7.20) using six seconds of angular velocity (in radians) for two speed 3.21& 8.04 KMH of car speed.

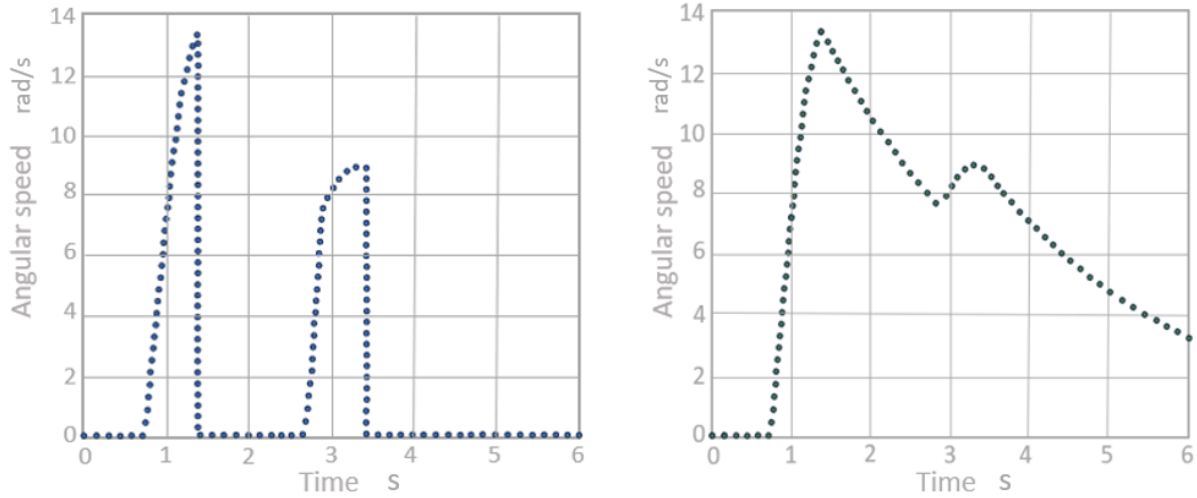


Figure 7. 19 The angular speed of generator & pinion plots to time for 3.21KMH of car speed

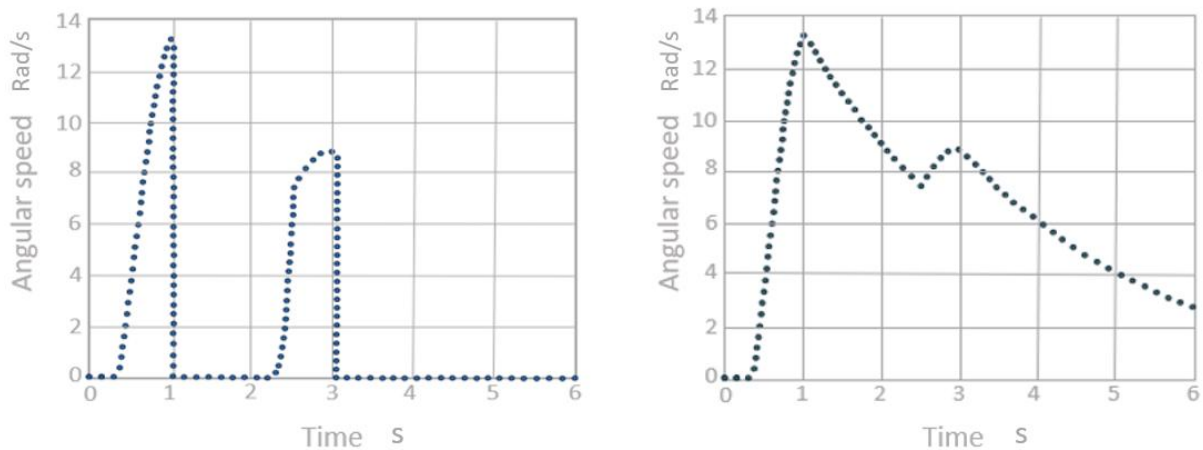


Figure 7. 20 The angular speed of generator & pinion plots to time for 8.04 KMH of car speed

The process of association and MMR dissociation is clearly visible in pervious graphs. As the vehicle begins to accelerate on the throttle pedal, the PHE descends and touches the rack and pinion assembly. Therefore, the system uses a pinion gear that drives the generator shaft at the same angular velocity. Once the lower limit of the rack is reached, the pinion releases and its angular velocity suddenly decreases to zero. After that, the system cuts off and the generator shaft continues to rotate with the decay factor ( $\alpha$ ) according to Equation (7.18).

Since the generated power is directly proportional to the square of the angular velocity of the generator shaft, the same trend is followed the second peak observed in the figure indicated that the system engaged in retrieval process. Another thing we notice here is that as the speed of the car increases, the peaks will get closer. This makes sense because, at high speeds, the person's foot stays on the throttle pedal and moves lower and lower. So, the closure coming to the summit is a validation of that. Also pressing the brake pedal will be done when there is an

emergency that needs to be pressed and using the same procedure as described before. on  $202\Omega$  we can find the power in Figure 7.21

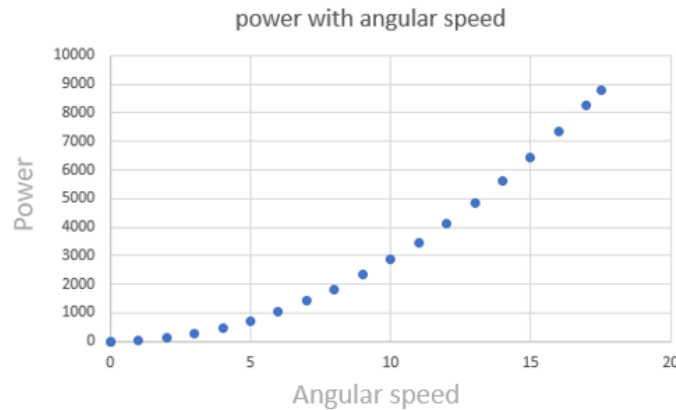


Figure 7. 21 The power with angular speed at  $202\Omega$

In order to study the impact of external loads on energy production, it is crucial to incorporate simulations. Testing different resistances connected to the generator provides valuable insights into current behavior and aids in determining the energy harvested through this method. The simulation was conducted within a speed range of 11.26 - 16.09 km/h. Figure 7.22 illustrates the results, showcasing two pressure peaks at PHE (Pressure High Efficiency) that generate power. For a resistance value of  $110\Omega$ , the first peak yielded approximately 1145 watts, while the second peak produced around 735 watts. These studies provide valuable information regarding the output harvesting energy under varying load conditions.

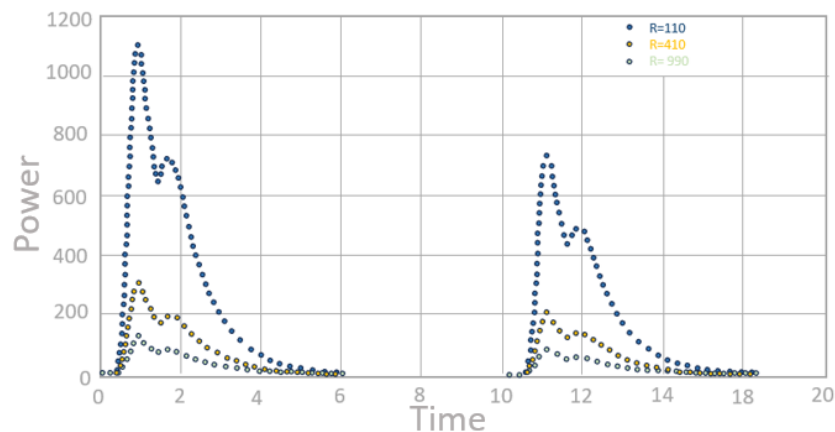


Figure 7. 22 The generating power with time and different resistance

## 7.5 Conclusion:

This study focuses on the investigation and development of alternative energy harvesting methods using scientific techniques and methodologies. Specifically, the pedal harvester and its geometry were extensively examined, leading to discover electrical harvesting method. The ability of the pedal energy harvester to generate electricity was evaluated through simulations and field tests. A MATLAB model was developed to analyze the simulation results. The prototype of PHE demonstrated the capability to generate approximately 1100 watts of peak power. It is important to note that the energy gained by the pedal harvester increases with the

frequency of pressing the throttle and brake pedals. This suggests that the proposed pedal power collector has the potential to provide sufficient power for signal transmission, monitoring sensors, and even recharging the battery of an electric car. The current prototype represents a pioneering design for future iterations of the pedal harvester. Overall, this research introduces another area of study and encourages researchers and engineers to further explore and advance this field of alternative energy harvesting.

## NEW SCIENTIFIC RESULTS OF THE THESES

### T1. The harvesting energy by electromagnetic effects as Radial & Axial Design (RD & AD):

In this study, I propose a novel method for energy production and harvesting from wheel movement, distinct from traditional approaches that focus on vibrations or suspensions. This strategy aims to assist hybrid or electric vehicles in charging their batteries while in motion, without the need to stop. The process involves converting the rotational motion of the wheels into electrical energy through electromagnetic principles, a concept that has been explored by various researchers. This research demonstrates that energy can be harvested from the rotation of the wheels on first case as RD design, approximately 2.5 mW of energy is generated by capturing the motion of magnets through the wheel's movement within a coil, in accordance with Faraday's law. This process was simulated using MATLAB, yielding a 2% error based on the magnetic dipole value. For another AD design, this energy harvester produced about 4.02 mW of power, also with a 3% error between the experimental data and the model at 53 rpm. (1)(5)

### T2. The harvesting energy by Piezoelectric materials inside the wheel:

In my study, I focused on the piezoelectric material PZT-5J because of its excellent mechanical strength and durability. I conducted a detailed analysis of the stress distribution within this material, aiming to optimize the performance of a piezoelectric energy harvester integrated into a vehicle damper system. To evaluate its effectiveness, I examined two different energy harvesting scenarios under varying mechanical conditions. In the first scenario, utilizing the specified materials, approximately 600  $\mu\text{W}$  was generated at a pressure of  $0.71 \times 10^6 \text{ N/m}^2$  over an area of  $0.01716 \text{ m}^2$ . Conversely, with a piezoelectric cell area of  $40 \text{ m}^2$  and a charge density of about 0.34 A, the output surged to 26 W. In the second scenario, the combination of piezoelectric and magnetostrictive effects resulted in an energy harvest of approximately 826  $\mu\text{W}$ . Within the field of piezoelectric applications, there is a pressing need to improve power output by investigating various designs. The efficiency of piezoelectric materials tends to decline over time, specifically between 1 to 5 minutes, with efficiencies ranging from 13.4% to 14.5%. To counteract this issue, it could be advantageous to implement multiple layers of these materials—potentially doubling or tripling them—within the wheel and conducting a comprehensive performance study. (4)(6)(9)

### T3. The harvesting energy by the piezoelectric roads:

My research supports the concept of a smart city by utilizing PZT materials with several assembly designs integrated into road layouts (LAD1, LAD2, LAD3, LAD4, LAD5, and LAD6). These designs generate energy that is transmitted to electric poles installed along the roads. A converter then transforms the output from AC to DC, enabling this energy to power vehicles and charge car batteries without requiring stops (smart roads) or in any place there is

HCS with stop of car. For instance, in the case of LAD1 with a resistance of  $335\text{ K}\Omega$ , the power output was approximately  $3 \times 10^{-5}\text{ W}$ . Likewise, with a resistance of  $565\text{ K}\Omega$ , the output increased to around  $3.5 \times 10^{-4}\text{ W}$ . In the case of LAD4 at a speed of  $9.5\text{ km/hr}$ , a resistance of  $20\text{ M}\Omega$  yielded a similar power output of  $0.275\text{ mW}$ . (3)(7)(8)(11)

#### T4. The harvesting energy by MMR:

This research introduces an innovative approach to energy harvesting from car pedals, distinguishing it from prior studies that predominantly focused on bike pedals. While previous investigations have explored energy harvesting from pedals in the context of Formula racing cars using manual methods, our research pioneers a new domain by emphasizing the potential of car pedals for energy generation. This study demonstrates that the energy produced coming from MMR achieves the conversion of linear motion from racks into rotational motion by interlocking pinion gears 1 and 2. When the driver vertically presses the pedal module, the rack moves, causing the pinion gear to rotate and the shaft to spin. This rotation of the shaft drives the gearbox, which in turn rotates the DC motor, generating electric power. It is equal approximately by simulated with MATLAB about  $1100\text{ to }1145\text{ W}$  and when increase the pressing of both pedals will be increase the output of energy also the number of pressings on pedals. In the context of MMR, conducting a stress analysis on critical components such as the connecting rod, foot cover, and rack and pinion gear assembly would be valuable. Investigating their failure modes can provide insights that future researchers can use to enhance the overall efficiency of the device. Additionally, comprehensive and rigorous in-field testing is essential to analyze the actual impact of the driver's leg on the pedals, particularly by leveraging the brake pedal during periods of heavy vehicle congestion, as well as to examine vehicle dynamics more thoroughly. (2)(10)

## Acknowledgements

I would like to express my heartfelt gratitude to all those who have supported me throughout my PhD journey.

First and foremost, I would like to thank my supervisor *Béla Kovács* for their invaluable guidance, encouragement, and support. Their expertise and insights have been instrumental in shaping my research and helping me overcome challenges.

I am also grateful to my committee members, *Dr. Szeidl Gyorgy*, for their constructive feedback and suggestions that enriched my work.

To my parents *Mom Zelal and Dad Mwafaq*, thank you for instilling in me the value of education and perseverance. Your constant encouragement has been my bedrock.

To my beloved wife *Nagham*, your unwavering support, patience, and encouragement have been my greatest source of strength throughout this challenging journey. Thank you for always believing in me, even when I doubted myself. Your sacrifices and understanding during the long nights and weekends of research have not gone unnoticed. You have been my confidante, my cheerleader, and my anchor, providing love and motivation when I needed it most.

To my wonderful children *Leen& Kenan*. Your laughter, curiosity, and love have been my greatest motivation throughout this journey. Thank you for your patience during the long hours I spent working on my research. You have shown remarkable understanding and support, even when it meant sacrificing family time. Your belief in me has inspired me to keep pushing forward, no matter the challenges I faced.

Finally, I would like to appreciate anyone else who played a role in my journey, whether big or small. Your support has meant the world to me.

{ *Thank you all for being part of this significant chapter of my life* }

## References

- [1] Pan, H., Qi, L., Zhang, Z., & Yan, J. (2021). Kinetic energy harvesting technologies for applications in land transportation: A comprehensive review. *Applied Energy*, 286, 116518.
- [2] Saidur, R., Rezaei, M., Muzammil, W. K., Hassan, M. H., Paria, S., & Hasanuzzaman, M. (2012). Technologies to recover exhaust heat from internal combustion engines. *Renewable and sustainable energy reviews*, 16(8), 5649-5659.
- [3] Tie, S. F., & Tan, C. W. (2013). A review of energy sources and energy management system in electric vehicles. *Renewable and sustainable energy reviews*, 20, 82-102.
- [4] Goswami, D. Y., & Kreith, F. (Eds.). (2007). *Energy conversion*. CRC press.
- [5] Lukic, S. M., Cao, J., Bansal, R. C., Rodriguez, F., & Emadi, A. (2008). Energy storage systems for automotive applications. *IEEE Transactions on industrial electronics*, 55(6), 2258-2267.
- [6] Larcher, D., & Tarascon, J. M. (2015). Towards greener and more sustainable batteries for electrical energy storage. *Nature chemistry*, 7(1), 19-29.
- [7] Svasta, P., Negroiu, R., & Vasile, A. (2017, October). Supercapacitors—An alternative electrical energy storage device. In *2017 5th International Symposium on Electrical and Electronics Engineering (ISEEE)* (pp. 1-5). IEEE.
- [8] Hedlund, M., Lundin, J., De Santiago, J., Abrahamsson, J., & Bernhoff, H. (2015). Flywheel energy storage for automotive applications. *Energies*, 8(10), 10636-10663.
- [9] Saidur, R., Rahim, N. A., & Hasanuzzaman, M. (2010). A review on compressed-air energy use and energy savings. *Renewable and sustainable energy reviews*, 14(4), 1135-1153.
- [10] Cusenza, M. A., Guarino, F., Longo, S., Ferraro, M., & Cellura, M. (2019). Energy and environmental benefits of circular economy strategies: The case study of reusing used batteries from electric vehicles. *Journal of Energy Storage*, 25, 100845.
- [11] Jafari Kaleybar, H., Golnargesi, M., Brenna, M., & Zaninelli, D. (2023). Hybrid Energy Storage System Taking Advantage of Electric Vehicle Batteries for Recovering Regenerative Braking Energy in Railway Station. *Energies*, 16(13), 5117.
- [12] Hedlund, M., Lundin, J., De Santiago, J., Abrahamsson, J., & Bernhoff, H. (2015). Flywheel energy storage for automotive applications. *Energies*, 8(10), 10636-10663.
- [13] POPA, D., FLORESCU, B., & TUDOR, I. KERS DYNAMICS (KINETIC ENERGY RECOVERY SYSTEMS).
- [14] Chain Bear. (2018, June20). *How does the MGU-K work?* [video]. YouTube. <https://www.youtube.com/watch?v=yhGDYDkrb8M>
- [15] Mercedes-AMG Petronas Formula One Team. (2022, October06). *Power Unit 101 with PETRONAS: MGU-H, EXPLAINED!* [video]. YouTube. <https://www.youtube.com/watch?v=Ha0ckcYVez0&t=5s>



- [16] Yadav, D. S., & Manisha, M. (2022, April). Electric Propulsion Motors: A Comparative Review for Electric and Hybrid Electric Vehicles. In 2022 IEEE International Conference on Distributed Computing and Electrical Circuits and Electronics (ICDCECE) (pp. 1-6). IEEE.
- [17] Donut. (2018, March21). *Turbos: How They Work | Science Garage* [video]. YouTube. <https://www.youtube.com/watch?v=lrCwmpjR77U&t=7s>
- [18] Maamer, B., Boughamoura, A., El-Bab, A. M. F., Francis, L. A., & Tounsi, F. (2019). A review on design improvements and techniques for mechanical energy harvesting using piezoelectric and electromagnetic schemes. *Energy Conversion and Management*, 199, 111973.
- [19] Halim, M. A., Rantz, R., Zhang, Q., Gu, L., Yang, K., & Roundy, S. J. A. E. (2018). An electromagnetic rotational energy harvester using sprung eccentric rotor, driven by pseudo-walking motion. *Applied Energy*, 217, 66-74.
- [20] Zhang, L. B., Dai, H. L., Yang, Y. W., & Wang, L. (2019). Design of high-efficiency electromagnetic energy harvester based on a rolling magnet. *Energy conversion and management*, 185, 202-210.
- [21] Jin, X., Yuan, Z., Shi, Y., Sun, Y., Li, R., Chen, J., ... & Wang, Z. L. (2021). Triboelectric Nanogenerator Based on a Rotational Magnetic Ball for Harvesting Transmission Line Magnetic Energy. *Advanced Functional Materials*, 2108827.
- [22] Wang, Z., Wang, W., Gu, F., Wang, C., Zhang, Q., Feng, G., & Ball, A. D. (2021). On-rotor electromagnetic energy harvester for powering a wireless condition monitoring system on bogie frames. *Energy Conversion and Management*, 243, 114413.
- [23] Calvo, J. A., Diaz, V., & San Roman, J. L. (2005). Establishing inspection criteria to verify the dynamic behavior of the vehicle suspension system by a platform vibrating test bench. *International journal of vehicle design*, 38(4), 290-306.
- [24] Donoso, G., Ladera, C.L. and Martin, P., 2009. Magnet fall inside a conductive pipe: motion and the role of the pipe wall thickness. *European Journal of Physics*, 30(4), p.855.
- [25] J. Cannarella, J. Selvaggi, S. Salon, J. Tichy and D.-A. Borca-Tasciuc, "Coupling factor between the magnetic and mechanical energy domains in electromagnetic power harvesting applications," *IEEE Transactions of Magnetics*, vol. 47, no. 8, pp. 2076-2080, 2011.
- [26] A. J. Sneller and B. P. Mann, "On the nonlinear electromagnetic coupling between a coil and an oscillating magnet," *Journal of Physics D: Applied Physics*, vol. 43, 2010.
- [27] K&J Magnetics. (2018, October 20). *Magnetic Dipole Moment* [video]. YouTube. <https://www.youtube.com/watch?v=7uicK71IPB4>
- [28] Al-Yafeai, D., Darabseh, T., & I. Mourad, A. H. (2020). A state-of-the-art review of car suspension-based piezoelectric energy harvesting systems. *Energies*, 13(9), 2336.
- [29] Darabseh, T., Al-Yafeai, D., Mourad, A. H. I., & Almaskari, F. (2021). Piezoelectric method-based harvested energy evaluation from car suspension system: simulation and experimental study. *Energy Science & Engineering*, 9(3), 417-433.
- [30] Li, T., & Lee, P. S. (2022). Piezoelectric energy harvesting technology: from materials, structures, to applications. *Small Structures*, 3(3), 2100128.

- [31] Erturk, A., & Inman, D. J. (2011). Piezoelectric energy harvesting. John Wiley & Sons.
- [32] Fiebig, M. (2005). Revival of the magnetoelectric effect. *Journal of physics D: applied physics*, 38(8), R123
- [33] Lee, E. W. (1955). Magnetostriction and magneto mechanical effects. *Reports on progress in physics*, 18(1), 184.
- [34] Kambale, R. C., Kang, J. E., Yoon, W. H., Park, D. S., Choi, J. J., Ahn, C. W., ... & Ryu, J. (2014). Magneto-mechano-electric (MME) energy harvesting properties of piezoelectric macro-fiber composite/Ni magnetoelectric generator. *Energy Harvesting and Systems*, 1(1-2), 3-11.
- [35] Kambale, R. C., Yoon, W. H., Park, D. S., Choi, J. J., Ahn, C. W., Kim, J. W., ... & Ryu, J. (2013). Magnetoelectric properties and magneto mechanical energy harvesting from stray vibration and electromagnetic wave by Pb (Mg $_{1/3}$ Nb $_{2/3}$ ) O $_3$ -Pb (Zr, Ti) O $_3$  single crystal/Ni cantilever. *Journal of Applied Physics*, 113(20), 204108.
- [36] El-Esnawy N. A., Akl A. Y. and Bazaraa A. S., "A new parametric infinite domain element," *Finite Elements in Analysis and Design*, 19(1-2), pp. 103-114 (1995). ISSN 0168-874X.
- [37] Zienkiewicz O. C., Emson C. and Bettess P., "A novel boundary infinite element," *International Journal for Numerical Methods in Engineering*, 19(3), pp. 393- 404 (1983). ISSN 0029-5981.
- [38] Erkal A., Laefer D. F. and Tezcan S. S., "Advantages of infinite elements over prespecified boundary conditions in unbounded problems," *Journal of Computing in Civil Engineering*, 29(6), p. 1-28 (2015). ISSN 8873801.
- [39] Means W.D. - 1976. Stress and strain. Basic concepts of continuum mechanics for geologists. Springer Verlag, New York. 339 p.
- [40] Oertel G.F.M. - 1996. Stress and deformation: a handbook on tensors in geology. Oxford University Press, New York. 292 p.
- [41] Pollard D.D. & Fletcher R.C. - 2005. Fundamentals of structural geology. Cambridge University Press, Cambridge. 500 p.
- [42] IEA (2023, March20). Electric Vehicles. Retrieved from <https://www.iea.org/energy-system/transport/electric-vehicles>
- [43] Li, F. C. (2019). An Abundant and Renewable Potential Energy Source: Harvestable Energy under Vehicle Wheels. *Global Challenges*, 3(7), 1800096.
- [44] Jin, X., Yuan, Z., Shi, Y., Sun, Y., Li, R., Chen, J., ... & Wang, Z. L. (2021). Triboelectric Nanogenerator Based on a Rotational Magnetic Ball for Harvesting Transmission Line Magnetic Energy. *Advanced Functional Materials*, 2108827.
- [45] Wang, Z., Wang, W., Gu, F., Wang, C., Zhang, Q., Feng, G., & Ball, A. D. (2021). On-rotor electromagnetic energy harvester for powering a wireless condition monitoring system on bogie frames. *Energy Conversion and Management*, 243, 114413.
- [46] Haocheng, X. (2014). Piezoelectric Energy Harvesting for Public Roadways (Doctoral dissertation, Virginia Polytechnic Institute and State University).

- [47] Wang, J., Xiao, F., & Zhao, H. (2021). Thermoelectric, piezoelectric and photovoltaic harvesting technologies for pavement engineering. *Renewable and Sustainable Energy Reviews*, 151, 111522.
- [48] Kim, C. I., Kim, K. B., Jeon, J. H., Jeong, Y. H., Cho, J. H., Paik, J. H., ... & Lee, Y. J. (2012). Development and evaluation of the road energy harvester using piezoelectric cantilevers. *Journal of the Korean Institute of Electrical and Electronic Material Engineers*, 25(7), 511-515.
- [49] Ashebo, D. B., Tan, C. A., Wang, J., & Li, G. (2008, April). Feasibility of energy harvesting for powering wireless sensors in transportation infrastructure applications. In *Nondestructive Characterization for Composite Materials, Aerospace Engineering, Civil Infrastructure, and Homeland Security 2008* (Vol. 6934, pp. 265-272). SPIE
- [50] Priya, S., & Inman, D. J. (Eds.). (2009). *Energy harvesting technologies* (Vol. 21, p. 2). New York: Springer.
- [51] Shashank, R., Harisha, S. K., & Abhishek, M. C. (2018, February). Modelling and analysis of piezoelectric cantilever energy harvester for different proof mass and material proportion. In *IOP Conference Series: Materials Science and Engineering* (Vol. 310, No. 1, p. 012147). IOP Publishing.
- [52] Li, Zhongjie, et al. "Energy-harvesting shock absorber with a mechanical motion rectifier." *Smart materials and structures* 22.2 (2012): 025008.
- [53] Suhalka, Rajneesh, et al. "Generation of electrical power using bicycle pedal." *International Journal of Recent Research and Review* 7.2 (2014): 63-67.
- [54] Arellano-Sánchez, Maria C., et al. "Static technologies associated with pedaling energy harvesting through rotary transducers, a review." *Applied Energy* 263 (2020): 114607.
- [55] Brushless DC motors with gearbox, Accessed (2023, March 01). Nanotec Electronic [Online]. Retrieved from <https://en.nanotec.com/brushless-dc-motors-with-gearbox>
- [56] Industrial quick search, Accessed (2023, February 01). Shaft coupling [Online]. Retrieved from <https://www.iqsdirectory.com/articles/shaft-couplings.html>.
- [57] Li, X., & Strezov, V. (2014). Modelling piezoelectric energy harvesting potential in an educational building. *Energy Conversion and Management*, 85, 435-442.
- [58] Zhang, Y., Huang, X., Chen, S., Guo, S. and Jin, S., 2015. Analyses of magnetic field in spiral steel pipe. *Journal of Magnetism and Magnetic Materials*, 375, pp.210-216.
- [59] J. Liu and S. Garrett, "Characterization of a small moving-magnet electrodynamic linear motor," *Journal of the Acoustical Society of America*, vol. 118, no. 4, p. 2289–2294, 2005.
- [60] S. D. Conrad, *Development of an inertial generator for embedded applications in rotating environments*, 2007.
- [61] S. X. Dong, J. F. Li, and D. Viehland, "Longitudinal and transverse magnetoelectric voltage coefficients of magnetostrictive/piezoelectric laminate composite: Theory," *Ieee Transactions on Ultrasonics Ferroelectrics and Frequency Control* 50 (10), 1253 (2003).
- [62] S. X. Dong and J. Y. Zhai, "Equivalent circuit method for static and dynamic analysis of magnetoelectric laminated composites," *Chinese Science Bulletin* 53 (14), 2113 (2008).

[63] S. X. Dong, J. F. Li, and D. Viehland, "Magnetolectric coupling, efficiency, and voltage gain effect in piezoelectric-piezomagnetic laminate composites," *Journal of Materials Science* 41 (1), 97 (2006).

## List of figures

Figure 1. 1	The flow chart of energy recovery system.....	10
Figure 2. 1	The mechanical flywheel system of KERS by Hedlund et al. [12] .....	12
Figure 2. 2	The mechanical flywheel with gear and generator system of KERS.....	12
Figure 2. 3	The generator with battery system of KERS .....	13
Figure 2. 4	The Illustration work of MGUK.....	13
Figure 2. 5	The Illustration work of MGU-H .....	14
Figure 2. 6	The torque of MGU-H in one loop .....	15
Figure 2. 7	Turbocharger cycle .....	16
Figure 2. 8	the MGU-H connecting with turbocharger.....	17
Figure 3. 1	The energy storage (ERS battery) .....	18
Figure 3. 2	The control electronic by (Bold valuable tec,2019) .....	18
Figure 3. 3	The scheme of other harvesting energy .....	19
Figure 4. 1	The simple drawing about placement of magnetic and coil for RD case .....	22
Figure 4. 2	The free body drawing of the magnetic inside coil in $\hat{n}$ and $\hat{\tau}$ coordinator system .....	23
Figure 4. 3	The response of system according to time.....	25
Figure 4. 4	The simple drawing about placement of magnetic and coil for AD case .....	26
Figure 4. 5	The motion of the magnetic inside the spoke without a coil .....	26
Figure 4. 6	The free body drawing of the magnetic for AD case .....	27
Figure 4. 7	The position of magnetic when entry and exit motion .....	28
Figure 4. 8	The magnetic field between the coil and magnetic.....	29
Figure 4. 9	The dimensions between the magnet and the coil .....	31
Figure 4. 10	The components for free falling test (a. the coil, b. the PP pipe, c. the disc magnet) .....	32
Figure 4. 11	The response system according to time .....	33
Figure 4. 12	The components for rotation motion test.....	33
Figure 4. 13	The response system according to time for rotation motion test for.....	34
Figure 4. 14	The relationship between the power and resistance.....	35
Figure 4. 15	The relationship between the energy and rotation of the wheel for (a. without friction, b. with friction) .....	35
Figure 5. 1	The three-axis direction of the piezoelectric material by (Li, X., & Strezov, V. ,2014) [57] .....	37
Figure 5. 2	The sketch and flowchart of operation sequence working for piezoelectric materials (first case) .....	39
Figure 5. 3	The prototype working for piezoelectric materials (second case) .....	40
Figure 5. 4	The different loading truck on piezoelectric cells inside the roads. a). One point loading, b). uniform distributed loading, C). triangle distributed loading .....	42
Figure 5. 5	Finite and infinite drawing under different loading.....	43
Figure 5. 6	Represents graphically the resolution of the stress vector $t$ according to normal element .....	44
Figure 5. 7	infinite medium model that is subjected to various types of loading, shear and stress forces.....	45
Figure 5. 8	visual representation of the stress distribution $\sigma_x$ , $\sigma_y$ , and $\tau_{xy}$ , in the piezoelectric cell along A-A section under three loads of point, triangular, and uniform .....	46
Figure 5. 9	the relationship between the charge density and contact area .....	47
Figure 5. 10	Schematic Illustration of energy harvesting for second case.....	47
Figure 5. 11	Schematic diagram of the first voltage generation .....	49
Figure 5. 12	Illustration of first generation .....	49

Figure 5. 13 Relation between power and voltage for First generation .....	50
Figure 5. 14 Schematic diagram of the second voltage generation.....	51
Figure 5. 15 Induced voltage generate per first layer V1 and second layer V2 .....	51
Figure 6. 1 A comprehensive statistical analysis of the electric vehicle markets as of IEA classification .....	53
Figure 6. 2 The flowchart of Harvesting Charging Station (HCS) .....	54
Figure 6. 3 Protective for our study cell of piezoelectric.....	56
Figure 6. 4 The first layout Assembly design .....	57
Figure 6. 5 The second layout Assembly design.....	57
Figure 6. 6 The third layout Assembly design .....	58
Figure 6. 7 The fourth layout Assembly design .....	59
Figure 6. 8 The fifth layout Assembly design.....	60
Figure 6. 9 The sixth layout Assembly design .....	60
Figure 6. 10 The types of disks piezoelectric which categorized as single, double, and four layers ...	61
Figure 6. 11 The tools testing for LAD1 .....	61
Figure 6. 12 The graph between P/f & R for the single-layer generator.....	62
Figure 6. 13 The graph between P/f & R for the double-layer generator.....	62
Figure 6. 14 The graph between P/f & R for the four-layer generator.....	62
Figure 6. 15 Model Mobile Loading Simulator .....	63
Figure 6. 16 The generating power with frequency when the resistor 335 K $\Omega$ .....	63
Figure 6. 17 The generating power with frequency when the resistor 565 K $\Omega$ .....	64
Figure 6. 18 The Illustration of the fourth design .....	64
Figure 6. 19 The relation between power and speed wheel with different loading resistance.....	66
Figure 6. 20 The graph of voltage for EREHV1 at 3.2Km/h.....	67
Figure 6. 21 The graph of voltage for EREHV2 at 3.2Km/h.....	67
Figure 6. 22 The graph of voltage for EREHV3 at 3.2Km/h.....	67
Figure 7. 1 concept development about pedal energy harvesting .....	69
Figure 7. 2 The main components for the harvester pedal energy .....	70
Figure 7. 3 A schematic of the (throttle & brake) module .....	70
Figure 7. 4 The Rack & pinion in pedal harvesting energy module .....	71
Figure 7. 5 The gearbox in pedal harvesting energy module .....	71
Figure 7. 6 The guide, FS32TT, L=460mm,9F, DF9 .....	72
Figure 7. 7 The bearing (a. FRN, b. FRNR) .....	72
Figure 7. 8 The support UCPA 206 of shaft.....	72
Figure 7. 9 The coupling of the shaft .....	73
Figure 7. 10 The brushless DC motor NEMA 17.....	73
Figure 7. 11 The mechanical motion transformation of the pedal harvesting energy .....	73
Figure 7. 12 A schematic of the mechanical motion transformation MMR for the third pedal .....	74
Figure 7. 13 The pressed force acting on the pedal (PHE) .....	75
Figure 7. 14 The connection between the PHE and the MMR by Cb, Kb.....	75
Figure 7. 15 The forces acting on rack of MMR.....	76
Figure 7. 16 The moment of inertia and torques of MMR.....	76
Figure 7. 17 The drawing of Simulink for whole the system.....	80
Figure 7. 18 The response system according to time for PHE.....	81
Figure 7. 19 The angular speed of generator & pinion plots to time for 3.21KMH of car speed .....	82
Figure 7. 20 The angular speed of generator & pinion plots to time for 8.04 KMH of car speed .....	82
Figure 7. 21 The power with angular speed at 202 $\Omega$ .....	83
Figure 7. 22 The generating power with time and different resistance.....	83

## List of tables

Table 1. 1 Measured parameters for simulation radial design.....	24
Table 1. 2 The last values for equation 4.11 .....	24
Table 1. 3 The specification about disc magnet in free falling test.....	32
Table 1. 4 The specification of the coil in free falling test.....	32
Table 1. 5 The specification of the PP pipe in free falling test.....	32
Table 1. 6 The specification of disc magnet in rotation motion test .....	34
Table 1. 7 The specification of the coil in rotation motion test.....	34
Table 1. 8 The specification of the PP pipe in rotation motion test.....	34
Table 2. 1 Characteristic of PZT-5J.....	40
Table 2. 2 Characteristic of wheel.....	41
Table 3. 1 Information about the tested indicators for simulation MMR.....	81
Table 3. 2 Information about pressing mass for small and big car.....	81

## List of publications

- (1) Mohammed Alaa Alwafaie, Bela Kovacs: empowering sustainability: The promise of energy harvesting from wheel motion (experiment and simulation). International Journal of Membrane Science and Technology, VoL.10 No. (4), pp 1517-1524, 2023 <https://doi.org/10.15379/ijmst.v10i4.2271>, MTMT No. 34550348, Rank: Q4
- (2) Mohammed Alaa Alwafaie, Bela Kovacs: the mechanism parts of mechanical motion rectifier to produce energy from third pedal in automotive, Acta Tecnológica - International Scientific Journal about Technologies, Volume: 9,2023 Issue: 2 Pages: 73-77, ISSN 2453-675X, Article DOI: <https://doi.org/10.22306/atec.v9i2.174>, MTMT NO. 34133445.
- (3) Mohammed Alaa Alwafaie, Bela Kovacs: testing LAD1of harvesting electric roads, Acta Mechatronica -International Scientific Journal about Mechatronics, Volume: 7 2022 Issue: 4 Pages: 25-29 ISSN 2453-7306, MTMT NO.33662173, Article: doi:10.22306/am. v7i4.87.
- (4) Mohammed Alaa Alwafaie, Bela Kovacs: dual - harvester energy (type3), Open Access Research Journal of Science and Technology,2022,04(02),067-071, MTMT NO.32769437, Article DOI: <https://doi.org/10.53022/oarjst.2022.4.2.0037>.
- (5) Mohammed Alaa Alwafaie, Béla Kovács: harvester wheel energy (type1), Quest Journals: Journal of Research in Mechanical Engineering, Volume 8 ~ Issue 1 (2022) pp:06-11ISSN(Online)2321-8185,2022, MTMT NO. 32653475, <http://www.questjournals.org/jrme/papers/vol8-issue1/B08010611.pdf>
- (6) Mohammed Alaa Alwafaie, Béla Kovács: harvester wheel energy (type 4), World Journal of Advanced Research and Reviews, 2022, 13(02), 304–308, MTMT 32695809, Article DOI: <https://doi.org/10.30574/wjarr.2022.13.2.0147>
- (7) Mohammed Alaa Alwafaie, Béla Kovács: electric charging platforms, International AEGEAN conferences on Innovation Technologies and Engineering V AEGEAN, February 25-26, 2022 / Izmir, Turkey, pp 33-37 (2022), MTMT no: 32769342.
- (8) Mohammed Alaa Alwafaie, Bela Kovacs: the review of infrastructure requirements for electric automotive, in 6. International Ankara multidisciplinary studies congress, October 13-14, 2023, Ankara, Turkey. 74-77. MTMT No. 34550378.
- (9) Mohammed Alaa Alwafaie, Bela Kovacs: studying the distribution of stress in two-dimensional compression piezoelectric cells under load-truck conditions, in 61st International Scientific Conference on experimental stress analysis 2023, June 6th – 8 th, 2023, Košice, Slovakia. 117- 124, MTMT NO. 34788590 (Scopus index).
- (10) Mohammed Alaa Alwafaie, Bela Kovacs: Investigating the feasibility of energy harvesting from the third pedal in automotive systems using a mechanical motion rectifier: simulation-based study, Acta Tecnológica - International Scientific Journal about Technologies, Volume: 10 2024 Issue: 2 Pages: 57-64 ISSN 2453-675X, Article DOI: <https://doi.org/10.22306/atec.v10i2.200>
- (11) Mohammed Alaa Alwafaie, Bela Kovacs: Design and evaluation of test assembly (LAD5) for electric road energy harvesting (EREH), AIP Conf. Proc. 3227, 030001 (2025), Volume 3227, Issue 1, 12 March 2025, <https://doi.org/10.1063/5.0241749>,